Copyright

by

Jackson White Massey

2015

The Thesis Committee for Jackson White Massey
Certifies that this is the approved version of the following thesis:

A Comprehensive Comparison of FFT-Accelerated Integral Equation Methods vs. FDTD for Bioelectromagnetics

APPROVED BY
SUPERVISING COMMITTEE:

Supervisor:

Ali E. Yılmaz, Supervisor

George Biros

A Comprehensive Comparison of FFT-Accelerated Integral Equation Methods vs. FDTD for Bioelectromagnetics

by

Jackson White Massey, B. S. E. E.

Thesis

Presented to the Faculty of the Graduate School of

The University of Texas at Austin

in Partial Fulfillment

of the Requirements

for the Degree of

Master of Science in Engineering

The University of Texas at Austin

May 2015

Dedication

To my family and partner

Acknowledgements

I would like to express my deepest gratitude to my family and partner for their continued love, support, and encouragement throughout my academic adventure.

I would also like to thank my supervisor, Dr. Ali Yılmaz, for his guidance, assistance, patience, and availability to help me reach this milestone.

I also want to thank my reader, Dr. George Biros, for his cooperation, patience and understanding as I worked on this thesis.

Additionally, I would like to thank my fellow research group members for their help. Max, Cemil, and Guneet deserve special recognition.

I acknowledge and thank the National Science Foundation and the T.L.L. Temple Foundation through the Cockrell School of Engineering for their generous financial support. Finally, I acknowledge the Texas Advanced Computing Center (TACC) at The University of Texas at Austin for providing HPC and visualization resources that have contributed to the research results reported within this thesis.

Abstract

A Comprehensive Comparison of FFT-Accelerated Integral Equation Methods vs. FDTD for Bioelectromagnetics

Jackson White Massey, MSE

The University of Texas at Austin, 2015

Supervisor: Ali E. Yılmaz

The performance of two FFT-accelerated integral equation methods—the adaptive integral method (AIM) and GMRES-FFT—and the finite-difference time-domain (FDTD) method are systematically compared for their use in bioelectromagnetic (BioEM) analysis. The comparison involves four steps: (i) A BioEM benchmark is developed. The power absorbed by a human model illuminated by an impressed time-harmonic source is selected as the problem of interest. The benchmark consists of three inhomogeneous models (a multilayered spherical head phantom, an anatomical male, and an anatomical female model), two types of models (pixel or surface based), two types of sources (far or near), and three frequencies in the UHF band (402 MHz, 900 MHz, and 2.45 GHz). (ii) Error and cost measures are identified: The total power absorbed, the power absorbed in different tissues, and the absorbed power density are compared to either analytical results or results from other methods. The peak memory requirement and computation time of the simulations are recorded. (iii) The benchmark problems are solved using each method with optimized parameters. (iv) Plots of results, errors, and computational costs are presented

and the tradeoff between increased accuracy and cost is quantified for each method. The data show that when surface-based models can be used AIM generally outperforms GMRES-FFT and FDTD: AIM achieves lower errors at the same computational cost or costs less to achieve the same error. When restricted to pixel-based models, however, FDTD generally outperforms GMRES-FFT and AIM: All three methods yield comparable errors, in most cases FDTD is less costly than GMRES-FFT (especially for anatomical models, far sources, and higher frequencies), and GMRES-FFT is slightly less expensive than AIM. These results suggest that for the type of BioEM analysis represented by the benchmark, AIM should be used whenever surface-based models are available and FDTD should be used if only pixel-based models are available.

Table of Contents

List of Tables

List of Figures

Chapter 1: Introduction

Bioelectromagnetic (BioEM) simulations in the UHF band (0.3-3 GHz) are becoming increasingly more important in the design of body-centric wireless communication systems [1], wireless implants [2]–[4], and medical imaging tools [5]–[7]. They are also needed to develop body area networking standards and to ensure that exposure to non-ionizing radiation remains lower than values specified in safety standards [8]–[10]. BioEM simulations can be categorized according to the complexity of the models used to represent the problem of interest and the type of numerical method used to solve the governing equations.

The complexity of the models used in BioEM simulations range from *simplified models*, e.g., infinite slabs [1], [2], [4], spheres [3], or phantoms [11], [12], to *anatomical models*, e.g., human or animal models [13]–[16]. Simplified models—which are generally piecewise homogeneous—are easy to build, modify, verify, and simulate accurately by a large variety of numerical methods, but have limited predictive capacity. In contrast, anatomical models—which are generally inhomogeneous—can yield detailed and highly predictive information, but are difficult to create, alter, validate, and simulate accurately.

The numerical methods used in BioEM simulations can be categorized as *differential-equation based methods,* e.g., the finite-difference time-domain (FDTD) method [17] or the finite-element method [18], or *integral-equation based methods*, e.g., the conjugate-gradient fast-Fourier-transform (CG-FFT) method [19], [20], fast multipole method [21], [22], or the adaptive integral method (AIM) [23]. Differential-equation based methods, which require the solution of sparse (or diagonal) matrix equations, are currently the most popular methods for BioEM simulation, especially when anatomical models are used; this can be attributed to their generality and flexibility in modeling position-

dependent material parameters, ease of implementation, robustness, and low computational overhead. These methods, however, have major accuracy and efficiency drawbacks that can limit their effectiveness. For example, classical explicit FDTD solvers must meet the (necessary but not sufficient) Courant-Friedrichs-Lewy (CFL) condition to yield stable results, implement approximate absorbing boundary conditions on an extended convex volume enclosing the biological object of interest to emulate open regions, ensure that unacceptable levels of numerical dispersion and phase error buildup are avoided for electrically large regions, and overcome staircasing errors at curved boundaries. In comparison, integral-equation based methods are not bound by the CFL condition, impose the radiation condition analytically, mesh only the surfaces of homogeneous regions and volumes of inhomogeneous regions (not an extended region around them), are more immune to phase error buildup, and can avoid staircasing errors robustly by using unstructured meshes. Yet, they require the use of carefully designed cubature rules to evaluate up to six-dimensional integrals with singular kernels, as well as complicated fast algorithms to efficiently solve dense matrix equations.

The above comparison of different numerical methods is inconclusive and should be enhanced with computational experiments to quantify the performance of these methods for BioEM simulations. This thesis develops benchmark BioEM problems, systematically compares two FFT-accelerated integral-equation methods to the FDTD method, and presents quantitative, comprehensive, and replicable computational results.

The performance of FDTD and integral-equation methods have been compared for BioEM simulations before [24]–[28]. Nevertheless, a comprehensive study of the different methods' performances is needed because of four reasons: (i) *Existing comparisons are rather rudimentary*; e.g., only 2-D BioEM problems were considered in [24]; the accuracy of the results were quantified only by plotting the electric field components along a line

through the object of interest in [24], [26]–[28] (no accuracy comparison was performed in [25] and analytical references were not used in [26], [28]); the integral-equation solution was not accelerated by a fast algorithm in [26], [28]; and computation times were not reported in [25], [26]. (ii) *Complexity and realism of BioEM models have increased drastically*. The latest anatomical human models feature mm-scale details and are comprised of more than 100 million elements (orders of magnitude larger than in [24]–[28]). Additionally, even though most anatomical models continue to be pixel-based models, several surface-based human models have been developed [14], [29], [30]. Because such models can potentially minimize the staircasing error inherent in pixel-based models, it is important to compare numerical methods for both pixel- and surface-based models. (iii) *FDTD and FFT-accelerated integral-equation methods have been actively researched*. For instance, for FDTD, more effective perfectly matched layers (PML) terminations have been developed [31] while for FFT-accelerated integral-equation methods, more accurate basis functions [32], [33], more advanced algorithms that are effective for unstructured meshes [34], and novel parallelization techniques [35] have been developed. (iv) *Computer hardware has improved significantly*. Increases in raw computing power (faster processors, more memory, more cores, and higher-speed interconnections) have enabled the solution of larger and more complex problems [36]. These improvements also enable better visualization of the large data sets—and therefore better means for interpreting results and measuring errors—generated by BioEM simulations.

Motivated by the shortcomings of previous comparative studies and by the ongoing advances in BioEM simulations, a systematic approach was recently introduced to empirically evaluate the advantages and tradeoffs of different methods for modern BioEM simulations [37]–[40]. The methodology is based on using error-vs.-cost plots with well-

defined and useful error measures. This thesis extends the methodology in [37]–[40] by modifying the error measures (from pointwise to cellwise), adding new error measures (visualizations, L∞-norm, and tissue absorbed power analysis), and providing a method for comparing numerical methods without a reliable reference result. It also introduces a BioEM benchmark that is appropriate for judging the performance of methods that compute the power absorbed by a human model illuminated with an impressed time-harmonic source. The benchmark consists of a multilayered sphere and two anatomical human models, two different excitations (plane wave and a nearby Hertzian dipole), and three representative frequencies in the UHF band.

Using the proposed comparison methodology and BioEM benchmark, this thesis compares the performance of FDTD and two FFT-based algorithms—AIM and GMRES-FFT (a variant of the CG-FFT method that uses the generalized minimal residual (GMRES) algorithm as the iterative solver). It is shown that all three numerical methods yield similar error levels for pixel-based models and that FDTD simulations are significantly less costly than GMRES-FFT and AIM simulations (which have similar costs), especially for anatomical models, plane-wave excitations, and higher frequencies in the UHF band. It is also shown that AIM simulations can yield significantly lower errors by using surface-based models (meshed with unstructured tetrahedral elements) and this approach requires less computation time and memory for a desired accuracy when compared to AIM, GMRES-FFT, or FDTD simulations that use pixel-based models (meshed with voxel elements).

The rest of the thesis is organized as follows: Chapter 2 reviews the different BioEM simulation methods evaluated in this thesis. Chapter 3 details the comparison methodology. Chapter 4 presents the results. Chapter 5 concludes the thesis.

Chapter 2: Review of Bioelectromagnetic Simulation Methods

This Chapter describes the scattering problems of interest, the governing equations, their discretization, and the three numerical solution methods considered in this thesis—GMRES-FFT, FDTD, and AIM. The FDTD and AIM methods are presented briefly as they are well established; more complete formulations and detailed explanations can be found in [17], [34], [38], [41], [42]. Although GMRES-FFT type methods are also available in the literature [20], [33], [41], [43], the formulation used here is more accurate compared to the existing ones and is thus presented in more detail. The goals of this Chapter are to identify the methods' key features and define all the parameters that must be specified to replicate the results presented in Chapter 4.

2.1 Scattering Problem and Governing Equations

The biological object of interest is modeled as an inhomogeneous, lossy, and nonmagnetic volume V in free space. The object is illuminated by the incident field $\{\mathbf{E}^{\text{inc}}, \mathbf{H}^{\text{inc}}\}$ generated by (nearby or far away) impressed sources. The fields scattered by the object $\{\mathbf{E}^{\text{sca}}, \mathbf{H}^{\text{sca}}\}$ satisfy the equations

$$\begin{aligned} \nabla \times \mathbf{E}^{\text{sca}}(\mathbf{r},t) &= -\mu_0 \partial_t \mathbf{H}^{\text{sca}}(\mathbf{r},t) \\ \nabla \times \mathbf{H}^{\text{sca}}(\mathbf{r},t) &= \varepsilon(\mathbf{r},t) * \partial_t \left[\mathbf{E}^{\text{sca}}(\mathbf{r},t) + \mathbf{E}^{\text{inc}}(\mathbf{r},t) \right] \\ &\quad + \sigma(\mathbf{r},t) * \left[\mathbf{E}^{\text{sca}}(\mathbf{r},t) + \mathbf{E}^{\text{inc}}(\mathbf{r},t) \right] \\ &\quad - \varepsilon_0 \partial_t \mathbf{E}^{\text{inc}}(\mathbf{r},t) \end{aligned} \tag{1}$$

for $\mathbf{r} \in V$. Here, $\{\varepsilon_0, \mu_0\}$ denotes the free-space {permittivity, permeability}, $\{\varepsilon, \sigma\}$ denotes the {permittivity, conductivity} of the object, $*$ denotes temporal convolution, and ∂_t denotes the time derivative. For time-harmonic fields with angular frequency ω, these equations can be simplified as

$$\begin{aligned}\nabla\times\tilde{\mathbf{E}}^{\text{sca}}\left(\mathbf{r},\omega\right)&=-j\omega\mu_0\tilde{\mathbf{H}}^{\text{sca}}\left(\mathbf{r},\omega\right)\\ \nabla\times\tilde{\mathbf{H}}^{\text{sca}}\left(\mathbf{r},\omega\right)&=j\omega\tilde{\varepsilon}\left(\mathbf{r},\omega\right)\tilde{\mathbf{E}}^{\text{sca}}\left(\mathbf{r},\omega\right)\\ &\quad+j\omega\left[\tilde{\varepsilon}\left(\mathbf{r},\omega\right)-\varepsilon_0\right]\tilde{\mathbf{E}}^{\text{inc}}\left(\mathbf{r},\omega\right),\end{aligned}\tag{2}$$

where $\tilde{\varepsilon}=\varepsilon-j\sigma/\omega$ denotes the complex permittivity of the object that includes the effects of static permittivity, dielectric heating, and Ohmic heating. Throughout the thesis, a tilde above a variable identifies it as a frequency-domain quantity.

Because the above partial differential equations are linear, various integro-differential equations that govern the fields can be formulated; e.g., a frequency-domain volume electric field integral equation (V-EFIE) can be formulated [32], [42] by expressing the scattered field in terms of the conduction-current corrected electric flux density $\tilde{\mathbf{D}}^{\text{c}}=\tilde{\varepsilon}[\tilde{\mathbf{E}}^{\text{inc}}+\tilde{\mathbf{E}}^{\text{sca}}]$:

$$\frac{\tilde{\mathbf{D}}^{\text{c}}\left(\mathbf{r},\omega\right)}{\tilde{\varepsilon}\left(\mathbf{r},\omega\right)}-\tilde{\mathbf{E}}^{\text{sca}}\left(\tilde{\mathbf{D}}^{\text{c}},\mathbf{r},\omega\right)=\tilde{\mathbf{E}}^{\text{inc}}\left(\mathbf{r},\omega\right)\ \text{for}\ \mathbf{r}\in V,\tag{3}$$

where,

$$\begin{aligned}\tilde{\mathbf{E}}^{\text{sca}}\left(\tilde{\mathbf{D}}^{\text{c}},\mathbf{r},\omega\right)&=\omega^2\mu_0\iiint_V\frac{\tilde{\kappa}\left(\mathbf{r}',\omega\right)\tilde{\mathbf{D}}^{\text{c}}\left(\mathbf{r}',\omega\right)e^{-j\omega R/c_0}}{4\pi R}dv'\\ &\quad+\nabla\iiint_V\frac{\nabla'\cdot\left(\tilde{\kappa}\left(\mathbf{r}',\omega\right)\tilde{\mathbf{D}}^{\text{c}}\left(\mathbf{r}',\omega\right)\right)e^{-j\omega R/c_0}}{\varepsilon_0 4\pi R}dv'.\end{aligned}\tag{4}$$

In (4), $\tilde{\kappa}\left(\mathbf{r},\omega\right)=\left(\tilde{\varepsilon}\left(\mathbf{r},\omega\right)-\varepsilon_0\right)\big/\tilde{\varepsilon}\left(\mathbf{r},\omega\right)$ is the complex contrast ratio, $R=\left|\mathbf{r}-\mathbf{r}'\right|$, and $c_0=1\big/\sqrt{\varepsilon_0\mu_0}$ is the speed of light in free space. It is worth emphasizing that the unknown $\tilde{\mathbf{D}}^{\text{c}}$ is constrained only to the object volume and the radiation condition is satisfied inherently by the choice of the negative exponent in the Green's function. It should also be noted that the integrals in (4), which have singular kernels, have to be computed rather accurately to ensure that addition of the incident and scattered fields, both of which are computed using the free-space phase speed, equals the total electric field, which propagates at different phase speeds in the inhomogeneous volume [44].

2.2 DISCRETIZATION

To solve the scattering problem, the fields are discretized in a volume V^{num} that either approximates V (for integral-equation based methods) or includes an extended region around V so that the radiation condition can be approximated accurately enough by local absorbing boundary conditions (for differential-equation based methods) [17]. This is typically accomplished by dividing V^{num} into small cells that are assigned homogeneous material properties [17], [32]. For the numerical methods studied in this thesis, either voxel or tetrahedral cells are used (Figure 1).

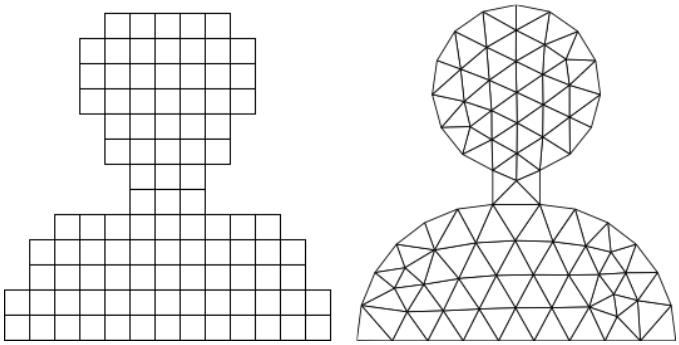

Figure 1: A biological object volume V meshed using voxel cells (left) or tetrahedral cells (right). The staircasing in voxel meshes yield poorer representation of the orginal boundaries.

Most anatomical models are created by segmenting a dataset of 2-D images and extruding pixels into voxels [16]. The resulting pixel-based models and their voxel meshes are immediately suitable for methods constrained to regular meshes (e.g., classical FDTD and GMRES-FFT methods). Unfortunately, voxel meshes constrain the material boundaries to align with a Cartesian coordinate system and thus can result in significantly less accurate solutions [45]. Indeed, the errors from staircasing in volumes that have curved surfaces can reduce the rate of convergence of the solution to zeroth-order locally and first-order globally (regardless of the simulation method) [46]. Furthermore, particularly with

coarser meshes, voxel meshes can yield extremely inaccurate volumes for small or thin tissues, e.g., the skin layer (see Chapter 3.1); thus, even if the overall solution is accurate, secondary quantities of interest derived from the solution that are localized, for instance, the total power absorbed by a small or thin tissue, can be inaccurate.

Unstructured tetrahedral meshes represent material boundaries significantly more accurately than voxels (Figure 1). Well-behaved tetrahedral meshes of V can be generated using standard algorithms [47], [48] provided that a surface-based model is available whose geometry can be represented analytically/drawn in a CAD program. Unfortunately, anatomical BioEM models cannot be easily represented as parameterized surfaces because of the complex topology, intricate spatial connectivity, and the multiple length scales of the tissues and because of the pixelated nature and very large size of the medical image datasets used to create these models. One avenue for generating quality tetrahedral meshes is to consider voxel meshes of pixel-based models as samples on a rectilinear grid of the volume V, extract isosurfaces for each tissue, smooth/improve these surfaces, combine the improved isosurfaces into one surface model, and then mesh the model with tetrahedra [14], [49]; this is also known as mesh-based geometry reconstruction [49]–[51]. Although it is relatively simple to extract one tissue/organ and construct a surface model for it from a pixel-based model, it is generally impossible to process each tissue/organ independently (one at a time) to obtain a topologically consistent (non-intersecting) set of surfaces that can be combined to form a surface-based anatomical BioEM model [30], [52]. Nevertheless, by introducing additional constraints on the surface construction algorithm, simplifying the surfaces, and introducing a background material [53], very complex surface-based anatomical models can be constructed [14], [29].

2.3 FFT-Accelerated Integral Equation Methods

This Subchapter reviews the two FFT-accelerated integral equation methods that are evaluated in this thesis. First, the classical iterative MOM solution of the frequency-domain V-EFIE is reviewed; then, the GMRES-FFT and AIM algorithms are described.

2.3.1 Method of Moments (MOM)

The classical MOM solution of the V-EFIE consists of three steps: (i) The scattering volume is meshed into tetrahedral/voxel cells and the unknown quantity $\tilde{\mathbf{D}}^{\mathrm{c}}$ is expanded using N_{MOM} sub-domain basis functions:

$$\tilde{\mathbf{D}}^{\mathrm{c}}(\mathbf{r},\omega) \approx \sum_{n=1}^{N_{\mathrm{MOM}}} \tilde{I}_n(\omega)\mathbf{f}_n(\mathbf{r}). \tag{5}$$

Here, $\mathbf{f}_1,\ldots,\mathbf{f}_{N_{\mathrm{MOM}}}$ are either SWG basis functions [32] defined on tetrahedral cells or volumetric rooftop basis functions [33] defined on voxel cells (Figure 2) and $\tilde{I}_1,\ldots,\tilde{I}_{N_{\mathrm{MOM}}}$ are their unknown coefficients. Both types of basis functions are divergence-conforming and are associated with cell faces such that the function support is over two cells if the face is an interior face and over only one cell if the face is on the boundary of V (Figure 2).

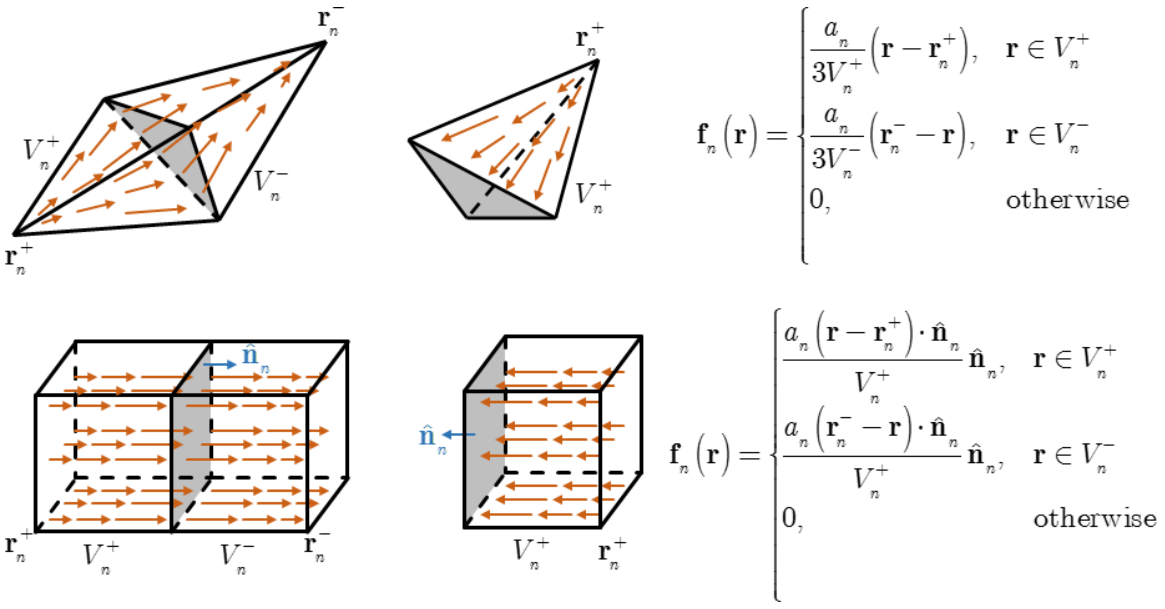

Figure 2: SWG [32] and volumetric rooftop [33] basis functions. The support of the basis functions is either over two cells if it is associated with an interior face (left) or over a single cell if it is associated with a boundary face (middle). In the formulas, a_n denotes the area of the face associated with the basis function, $\mathbf{r}_n^{\pm}$ is the position of a node that belongs to $V_n^{\pm}$ that is not on the associated face, and $\hat{\mathbf{n}}_n$ is the unit vector normal to the associated face pointing from V_n^+ to V_n^-.

(ii) For each frequency of interest, the V-EFIE is converted into a linear system of equations by Galerkin testing it with contrast-weighted basis functions:

$$\left\langle \tilde{\kappa}_m(\mathbf{r},\omega)\mathbf{f}_m(\mathbf{r}), \frac{\tilde{\mathbf{D}}^c(\mathbf{r},\omega)}{\tilde{\varepsilon}(\mathbf{r},\omega)} \right\rangle - \left\langle \tilde{\kappa}_m(\mathbf{r},\omega)\mathbf{f}_m(\mathbf{r}), \tilde{\mathbf{E}}^{\text{sca}}(\mathbf{r},\omega) \right\rangle = \left\langle \tilde{\kappa}_m(\mathbf{r},\omega)\mathbf{f}_m(\mathbf{r}), \tilde{\mathbf{E}}^{\text{inc}}(\mathbf{r},\omega) \right\rangle \tag{6}$$

for $m = 1,\ldots,N_{\text{MOM}}$. Here, $\tilde{\kappa}_m(\mathbf{r},\omega) = \left(\tilde{\varepsilon}_m(\mathbf{r},\omega) - \varepsilon_0\right)/\tilde{\varepsilon}_m(\mathbf{r},\omega)$ is an approximation of the contrast ratio that is piecewise-constant over the support of $\mathbf{f}_m$, i.e., $\tilde{\varepsilon}$ and $\tilde{\kappa}$ are assumed constant in each cell. In (6), $\langle , \rangle$ denotes the inner product of the two arguments; in the following, the integral resulting from the $\tilde{\mathbf{D}}^c/\tilde{\varepsilon}$ term is referred to as the self-term. The resulting system of equations can be written in matrix form as

$$\mathbf{Z}(\omega)\mathbf{I}(\omega) = \left[\mathbf{Z}^{\text{self}}(\omega) + \mathbf{Z}^{\text{sca}}(\omega)\right]\mathbf{I}(\omega) = \mathbf{V}^{\text{inc}}(\omega), \tag{7}$$

where $\mathbf{Z}$, $\mathbf{Z}^{\text{self}}$, and $\mathbf{Z}^{\text{sca}}$ are $N_{\text{MOM}} \times N_{\text{MOM}}$ impedance matrices and $\mathbf{I}$ and $\mathbf{V}^{\text{inc}}$ are $N_{\text{MOM}} \times 1$ vectors that store the unknown coefficients and the tested incident field, respectively. The sparse matrix $\mathbf{Z}^{\text{self}}$ stores the self-term contribution in (6) and the dense matrix $\mathbf{Z}^{\text{sca}}$ results in the tested scattered field when multiplied with $\mathbf{I}$; the entries of these matrices and vectors are:

$$\begin{aligned}
\mathbf{Z}^{\text{self}}[m,n] &= \iiint_{V^{\text{num}}} \frac{\tilde{\kappa}_m(\mathbf{r},\omega)\mathbf{f}_m(\mathbf{r})\bullet\mathbf{f}_n(\mathbf{r})}{\tilde{\varepsilon}_n(\mathbf{r},\omega)}\,dv \\
\mathbf{Z}^{\text{sca}}[m,n] &= -\omega^2\mu_0 \iiint_{V^{\text{num}}}\iiint_{V^{\text{num}}} \frac{\tilde{\kappa}_m(\mathbf{r},\omega)\mathbf{f}_m(\mathbf{r})\bullet\tilde{\kappa}_n(\mathbf{r}',\omega)\mathbf{f}_n(\mathbf{r}')e^{-j\omega R/c_0}}{4\pi R}\,dv'dv \\
&\quad + \frac{1}{\varepsilon_0}\iiint_{V^{\text{num}}}\iiint_{V^{\text{num}}} \frac{\nabla\bullet\left(\tilde{\kappa}_m(\mathbf{r},\omega)\mathbf{f}_m(\mathbf{r})\right)\nabla'\bullet\left(\tilde{\kappa}_n(\mathbf{r}',\omega)\mathbf{f}_n(\mathbf{r}')\right)e^{-j\omega R/c_0}}{4\pi R}\,dv'dv \\
\mathbf{V}^{\text{inc}}[m] &= \iiint_{V^{\text{num}}} \tilde{\kappa}_m(\mathbf{r},\omega)\mathbf{f}_m(\mathbf{r})\bullet\tilde{\mathbf{E}}^{\text{inc}}(\mathbf{r})\,dv.
\end{aligned} \tag{8}$$

(iii) The linear system of equations in (7) is formed and solved. Because the $\mathbf{Z}^{\text{sca}}$ matrix is dense, the classical iterative MOM procedure requires $O\left(N_{\text{MOM}}^2\right)$ operations to fill this matrix, $O\left(N_{\text{MOM}}^2\right)$ bytes of memory to store it, and $O\left(N_{\text{MOM}}^2\right)$ operations to multiply it at each iteration. These costs imply that the MOM procedure quickly becomes unfeasible for the problem sizes encountered in BioEM analysis, which reach up to $N_{\text{MOM}} = 10^9$ [23], and advanced algorithms must be used to reduce the computational costs.

2.3.2 GMRES-FFT

Similar to the CG-FFT [33], [43], BCG-FFT [20], [41], and TFQMR-FFT [54] methods, the GMRES-FFT method accelerates the MOM solution by exploiting the translational invariance of the Green's function. In the following, the GMRES-FFT method is formulated by first describing the common CG-FFT method, then highlighting the

shortcomings of this formulation and presenting alternate formulations, including the GMRES-FFT implementation used in this thesis.

Common CG-FFT Formulation

As is commonly formulated (e.g., see [33]), the CG-FFT method follows the MOM formulation in Chapter 2.3.1. Here, the smallest cuboid that encloses V is meshed into $N_x \times N_y \times N_z$ voxels for the discretization step (Figure 3). The mesh is defined by the voxel cell size ($\Delta x, \Delta y, \Delta z$), the number of voxels in each dimension (N_x, N_y, N_z), and the mesh offset ($\mathbf{r}_0$) from the Cartesian origin. The mesh, which includes both free-space cells and cells inside V , is a regular mesh, i.e., the edge lengths of the voxels must all be the same size but are not required to be uniform ($\Delta x, \Delta y, \Delta z$ are constant throughout the mesh but not equal to each other). Voxels are identified using the mesh indices, $i \in \{1, \ldots, N_x\}$, $j \in \{1, \ldots, N_y\}$, $k \in \{1, \ldots, N_z\}$, e.g., the center of voxel i, j, k is located at $\mathbf{r}_{(i,j,k)} = \mathbf{r}_0 + (i - 0.5)\Delta x\hat{\mathbf{x}} + (j - 0.5)\Delta y\hat{\mathbf{y}} + (k - 0.5)\Delta z\hat{\mathbf{z}}$.

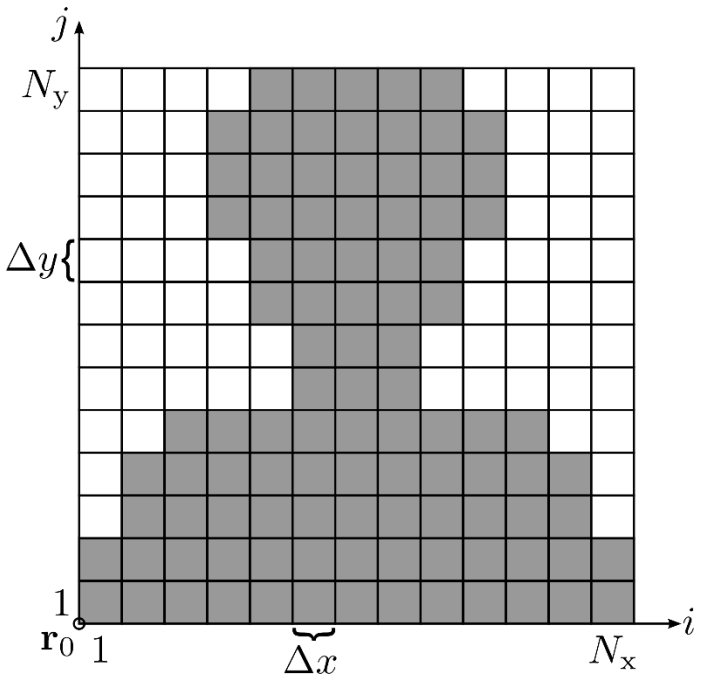

Figure 3: The smallest cuboid that encloses the biological object volume V (shaded) from Figure 1. The voxel mesh of the cuboid is defined by the the mesh offset ($\mathbf{r}_0$), the voxel size ($\Delta x, \Delta y, \Delta z$), and the number of voxels in each dimension (N_x, N_y, N_z). The z dependent quantities are not shown in this 2-D cut.

In the common CG-FFT method [33], the sub-domain vector basis functions are volumetric rooftop functions (that are piecewise linear in one dimension and piecewise constant in the other two dimensions) and are defined across pairs of voxels whose support both lie in V [33]. The orientation and location of the volumetric rooftop functions on the voxel mesh are denoted using the notation $\mathbf{f}_{\mathbf{n}}^{q}$, where $q \in \{x, y, z\}$ indicates the function's orientation and the vector $\mathbf{n} = (i, j, k)$ indicates the position of the common face between two voxels (Figure 4). More specifically, the volumetric rooftop function $\mathbf{f}_{\mathbf{n}}^{q}$ is defined over the two voxels whose centers are at $\mathbf{r}_{\mathbf{n}} = \mathbf{r}_0 + (i-0.5)\Delta x\hat{\mathbf{x}} + (j-0.5)\Delta y\hat{\mathbf{y}} + (k-0.5)\Delta z\hat{\mathbf{z}}$ and $\mathbf{r}_{\mathbf{n}+\Delta^q} = \mathbf{r}_{\mathbf{n}} + \left[\hat{\mathbf{q}} \bullet (\Delta x\hat{\mathbf{x}} + \Delta y\hat{\mathbf{y}} + \Delta z\hat{\mathbf{z}})\right]\hat{\mathbf{q}}$, where Δ^q is the +1 shift operator in the $\hat{\mathbf{q}}$ direction; e.g., $\mathbf{f}_{(i,j,k)}^{x}$ would denote an x-directed rooftop function whose center of the shared face is located at $\mathbf{r}_0 + (i\Delta x, (j-0.5)\Delta y, (k-0.5)\Delta z)$. A total of $(N_x - 1) \times N_y \times N_z$ x-

directed, $N_x \times (N_y - 1) \times N_z$ y-directed, and $N_x \times N_y \times (N_z - 1)$ z-directed volumetric rooftop functions are used[1], i.e.,

$$\mathbf{f}_{\mathbf{n}}^{q} \in \left\{ \mathbf{f}_{(i,j,k)}^{q} \,|\, 1 \le i \le N_x - \hat{\mathbf{q}} \bullet \hat{\mathbf{x}},\ 1 \le j \le N_y - \hat{\mathbf{q}} \bullet \hat{\mathbf{y}},\ 1 \le k \le N_z - \hat{\mathbf{q}} \bullet \hat{\mathbf{z}} \right\} \text{ for } q \in \{x, y, z\}. \quad (9)$$

Thus, the unknown is expanded as[2]

$$\tilde{\mathbf{D}}^{c}(\mathbf{r}, \omega) \approx \sum_{q \in \{x,y,z\}} \sum_{\mathbf{n}} \tilde{I}_{\mathbf{n}}^{q}(\omega) \mathbf{f}_{\mathbf{n}}^{q}(\mathbf{r}). \quad (10)$$

It is important to notice that, unlike the expansion in (5), all of the basis functions in (10) have a support over two cells, i.e., the "half" volumetric rooftop function depicted in Figure 2 is not used in CG-FFT when only one voxel lies in V, such as those on the boundary (see various alternative formulations that address this shortcoming below).

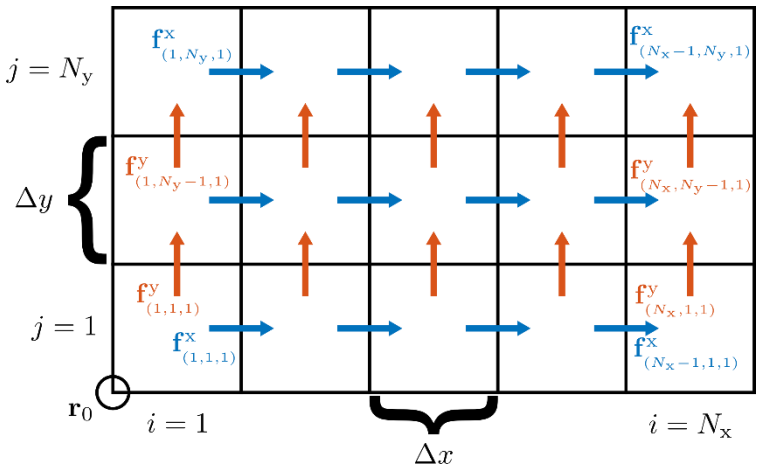

Figure 4: The notation used to refer to the volumetric rooftop functions. The x-directed (blue) and y-directed (orange) basis/testing functions are shown as arrows across the shared face. The figure shows $N_x \times N_y = 5 \times 3$ voxels, $(N_x - 1) \times N_y$ x-directed volumetric rooftop functions $\mathbf{f}^x_{(i,j,k)}$, and $N_x \times (N_y - 1)$ y-directed functions. The z-directed basis/testing functions are not shown in this 2-D cut.

[1] These basis functions include those defined over free-space voxels inside the cuboid enclosing V.
[2] The coefficients $\tilde{I}_{\mathbf{n}}^{q}$ corresponding to basis functions whose support include free-space voxels are set to 0.

In the CG-FFT method of [33], the V-EFIE is Galerkin tested with the basis functions[3]:

$$\left\langle \mathbf{f}_{\mathbf{m}}^{p}(\mathbf{r}), \frac{\tilde{\mathbf{D}}^{\mathrm{c}}(\mathbf{r},\omega)}{\tilde{\varepsilon}(\mathbf{r},\omega)} \right\rangle - \left\langle \mathbf{f}_{\mathbf{m}}^{p}(\mathbf{r}), \tilde{\mathbf{E}}^{\mathrm{sca}}(\mathbf{r},\omega) \right\rangle = \left\langle \mathbf{f}_{\mathbf{m}}^{p}(\mathbf{r}), \tilde{\mathbf{E}}^{\mathrm{inc}}(\mathbf{r},\omega) \right\rangle, \tag{11}$$

where

$$\mathbf{f}_{\mathbf{m}}^{p} \in \left\{ \mathbf{f}_{(i,j,k)}^{p} \,|\, 1 \le i \le N_{\mathrm{x}} - \hat{\mathbf{p}}\bullet\hat{\mathbf{x}},\ 1 \le j \le N_{\mathrm{y}} - \hat{\mathbf{p}}\bullet\hat{\mathbf{y}},\ 1 \le k \le N_{\mathrm{z}} - \hat{\mathbf{p}}\bullet\hat{\mathbf{z}} \right\} \text{ for } p \in \{\mathrm{x},\mathrm{y},\mathrm{z}\}. \tag{12}$$

Separating the basis and testing functions by their orientation, the equation that is enforced by each[4] testing function $\mathbf{f}_{\mathbf{m}}^{p}$ can be written as:

$$\sum_{q\in\{x,y,z\}} \sum_{\mathbf{n}} \left(Z_{\mathbf{mn}}^{\mathrm{self},pq}(\omega) + Z_{\mathbf{mn}}^{\mathbf{A},pq}(\omega) + Z_{\mathbf{mn}}^{\phi,pq}(\omega) \right) I_{\mathbf{n}}^{q}(\omega) = V_{\mathbf{m}}^{\mathrm{inc},p}(\omega), \tag{13}$$

where

$$V_{\mathbf{m}}^{\mathrm{inc},p}(\omega) = \iiint_{V_{\mathbf{m}}^{p}} \mathbf{f}_{\mathbf{m}}^{p}(\mathbf{r})\bullet\tilde{\mathbf{E}}^{\mathrm{inc}}(\mathbf{r},\omega)\,dv \tag{14}$$

$$Z_{\mathbf{mn}}^{\mathrm{self},pq}(\omega) = \iiint_{V_{\mathbf{m}}^{p}} \frac{\mathbf{f}_{\mathbf{m}}^{p}(\mathbf{r})\bullet\mathbf{f}_{\mathbf{n}}^{q}(\mathbf{r})}{\tilde{\varepsilon}_{\mathbf{n}}(\mathbf{r},\omega)}\,dv \tag{15}$$

$$Z_{\mathbf{mn}}^{\mathbf{A},pq}(\omega) = -\omega^2\mu_0 \iiint_{V_{\mathbf{m}}^{p}} \iiint_{V_{\mathbf{n}}^{q}} \frac{\mathbf{f}_{\mathbf{m}}^{p}(\mathbf{r})\bullet\tilde{\kappa}_{\mathbf{n}}(\mathbf{r}',\omega)\mathbf{f}_{\mathbf{n}}^{q}(\mathbf{r}')e^{-j\omega R/c_0}}{4\pi R}\,dv'dv \tag{16}$$

$$Z_{\mathbf{mn}}^{\phi,pq}(\omega) = \frac{1}{\varepsilon_0} \iiint_{V_{\mathbf{m}}^{p}} \iiint_{V_{\mathbf{n}}^{q}} \frac{\nabla\bullet\left(\mathbf{f}_{\mathbf{m}}^{p}(\mathbf{r})\right)\nabla'\bullet\left(\tilde{\kappa}_{\mathbf{n}}(\mathbf{r}',\omega)\mathbf{f}_{\mathbf{n}}^{q}(\mathbf{r}')\right)e^{-j\omega R/c_0}}{4\pi R}\,dv'dv. \tag{17}$$

Here, $V_{\mathbf{m}}^{p}$ and $V_{\mathbf{n}}^{q}$ denote the support of the testing function $\mathbf{f}_{\mathbf{m}}^{p}$ and basis function $\mathbf{f}_{\mathbf{n}}^{q}$, respectively. Note that $Z_{\mathbf{mn}}^{\mathrm{self},pq}$ and $Z_{\mathbf{mn}}^{\mathbf{A},pq}$ are both 0 for $p \neq q$ due to the dot product.

[3]The careful reader will notice another difference between the CG-FFT method of [33] and the integral-equation methods in this thesis: The V-EFIE is tested with contrast-weighted functions in (6). Although this testing scheme—also referred to as "symmetric testing" [55], [56]—lowers AIM matrix fill time and memory requirement (because it yields identical anterpolation and interpolation coefficients), it appears not to have a significant effect on the number of iterations or other MOM or GMRES-FFT costs [56]. Nevertheless, symmetric testing is also used for GMRES-FFT and MOM to ensure that all integral-equation methods in this thesis attempt to (approximately) solve the exact same set of equations; in other words, AIM and GMRES-FFT solutions will converge to the MOM ones.

[4] The equations corresponding to testing functions whose support include free-space voxels are discarded.

Furthermore, $Z_{\mathbf{mn}}^{\text{self},pq}$ is almost always zero: it has at most 3 testing functions that give non-zero values per basis function.

Using the formula for the volumetric rooftop function given in Figure 2, the basis functions can each be separated into two pieces: $\mathbf{f}_{\mathbf{n}}^{q+}$ and $\mathbf{f}_{\mathbf{n}+\boldsymbol{\Delta}^q}^{q-}$ defined over the two voxels that are centered at $\mathbf{r}_{\mathbf{n}}$ and $\mathbf{r}_{\mathbf{n}+\boldsymbol{\Delta}^q}$, i.e., the support of these two pieces are $V_{\mathbf{n}}$ and $V_{\mathbf{n}+\boldsymbol{\Delta}^q}$, respectively. This separation ensures that the contrast ratio is constant over the integration domain, i.e., $\tilde{\kappa}_{\mathbf{n}}(\mathbf{r},\omega)$ is equal to $\tilde{\kappa}_{\mathbf{n}}(\omega)$ in the first voxel and $\tilde{\kappa}_{\mathbf{n}+\boldsymbol{\Delta}^q}(\omega)$ in the second one. Thus, (16) can be rewritten as

$$Z_{\mathbf{mn}}^{\mathbf{A},pq}(\omega) = -\omega^2\mu_0 \left\{ \begin{array}{l} \tilde{\kappa}_{\mathbf{n}}(\omega) \iiint\limits_{V_{\mathbf{m}}^p} \iiint\limits_{V_{\mathbf{n}}} \dfrac{\mathbf{f}_{\mathbf{m}}^{p}(\mathbf{r}) \bullet \mathbf{f}_{\mathbf{n}}^{q+}(\mathbf{r}') e^{-j\omega R/c_0}}{4\pi R} dv' dv \\ + \tilde{\kappa}_{\mathbf{n}+\boldsymbol{\Delta}^q}(\omega) \iiint\limits_{V_{\mathbf{m}}^p} \iiint\limits_{V_{\mathbf{n}+\boldsymbol{\Delta}^q}} \dfrac{\mathbf{f}_{\mathbf{m}}^{p}(\mathbf{r}) \bullet \mathbf{f}_{\mathbf{n}+\boldsymbol{\Delta}^q}^{q-}(\mathbf{r}') e^{-j\omega R/c_0}}{4\pi R} dv' dv \end{array} \right\}, \tag{18}$$

which emphasizes the translational invariance of the two integrals (they only depend on $\mathbf{m}-\mathbf{n}$). Prior to updating (17), $\nabla' \bullet \left(\tilde{\kappa}(\mathbf{r}',\omega) \mathbf{f}_{\mathbf{n}}^{q}(\mathbf{r}') \right)$ is expanded using the chain rule:

$$\nabla' \bullet \left(\tilde{\kappa}(\mathbf{r}',\omega) \mathbf{f}_{\mathbf{n}}^{q}(\mathbf{r}') \right) = \begin{cases} \tilde{\kappa}_{\mathbf{n}}(\omega) \nabla' \bullet \mathbf{f}_{\mathbf{n}}^{q+}(\mathbf{r}'), & \mathbf{r}' \in V_{\mathbf{n}} \\ \tilde{\kappa}_{\mathbf{n}+\boldsymbol{\Delta}^q}(\omega) \nabla' \bullet \mathbf{f}_{\mathbf{n}+\boldsymbol{\Delta}^q}^{q-}(\mathbf{r}'), & \mathbf{r}' \in V_{\mathbf{n}+\boldsymbol{\Delta}^q} \\ \tilde{\kappa}_{\mathbf{n}+\boldsymbol{\Delta}^q}(\omega) - \tilde{\kappa}_{\mathbf{n}}(\omega), & \mathbf{r}' \in S_{\mathbf{n}}^{q} \\ 0, & \text{otherwise} \end{cases} \tag{19}$$

yielding

$$
\begin{aligned}
Z_{\mathbf{mn}}^{\phi,pq}(\omega) &= \frac{\tilde{\kappa}_{\mathbf{n}}(\omega)}{\varepsilon_0} \iiint_{V_{\mathbf{m}}^p} \iiint_{V_{\mathbf{n}}} \frac{\nabla\bullet\left(\mathbf{f}_{\mathbf{m}}^{p}(\mathbf{r})\right)\nabla'\bullet\left(\mathbf{f}_{\mathbf{n}}^{q+}(\mathbf{r}')\right)e^{-j\omega R/c_0}}{4\pi R} dv'dv \\
&\quad + \frac{\tilde{\kappa}_{\mathbf{n}+\Delta^q}(\omega)}{\varepsilon_0} \iiint_{V_{\mathbf{m}}^p} \iiint_{V_{\mathbf{n}+\Delta^q}} \frac{\nabla\bullet\left(\mathbf{f}_{\mathbf{m}}^{p}(\mathbf{r})\right)\nabla'\bullet\left(\mathbf{f}_{\mathbf{n}+\Delta^q}^{q-}(\mathbf{r}')\right)e^{-j\omega R/c_0}}{4\pi R} dv'dv \\
&\quad + \frac{\left(\tilde{\kappa}_{\mathbf{n}+\Delta^q}(\omega)-\tilde{\kappa}_{\mathbf{n}}(\omega)\right)}{\varepsilon_0} \iiint_{V_{\mathbf{m}}^p} \iint_{S_{\mathbf{n}}^q} \frac{\nabla\bullet\left(\mathbf{f}_{\mathbf{m}}^{p}(\mathbf{r})\right)e^{-j\omega R/c_0}}{4\pi R} ds'dv \\
&= \frac{\tilde{\kappa}_{\mathbf{n}}(\omega)}{\varepsilon_0} \left\{ \begin{array}{l} \displaystyle\iiint_{V_{\mathbf{m}}^p} \iiint_{V_{\mathbf{n}}} \frac{\nabla\bullet\left(\mathbf{f}_{\mathbf{m}}^{p}(\mathbf{r})\right)\nabla'\bullet\left(\mathbf{f}_{\mathbf{n}}^{q+}(\mathbf{r}')\right)e^{-j\omega R/c_0}}{4\pi R} dv'dv \\ \displaystyle -\iiint_{V_{\mathbf{m}}^p} \iint_{S_{\mathbf{n}}^q} \frac{\nabla\bullet\left(\mathbf{f}_{\mathbf{m}}^{p}(\mathbf{r})\right)e^{-j\omega R/c_0}}{4\pi R} ds'dv \end{array} \right\} \\
&\quad + \frac{\tilde{\kappa}_{\mathbf{n}+\Delta^q}(\omega)}{\varepsilon_0} \left\{ \begin{array}{l} \displaystyle\iiint_{V_{\mathbf{m}}^p} \iiint_{V_{\mathbf{n}+\Delta^q}} \frac{\nabla\bullet\left(\mathbf{f}_{\mathbf{m}}^{p}(\mathbf{r})\right)\nabla'\bullet\left(\mathbf{f}_{\mathbf{n}+\Delta^q}^{q-}(\mathbf{r}')\right)e^{-j\omega R/c_0}}{4\pi R} dv'dv \\ \displaystyle +\iiint_{V_{\mathbf{m}}^p} \iint_{S_{\mathbf{n}}^q} \frac{\nabla\bullet\left(\mathbf{f}_{\mathbf{m}}^{p}(\mathbf{r})\right)e^{-j\omega R/c_0}}{4\pi R} ds'dv \end{array} \right\}.
\end{aligned} \tag{20}
$$

where $S_{\mathbf{n}}^q$ is the common face between the two voxels. The terms in curly brackets in (20) are also translationally invariant and only depend on $\mathbf{m}-\mathbf{n}$. Thus, (13) can be expressed as

$$
\begin{aligned}
V_{\mathbf{m}}^{\text{inc},p}(\omega) &= \sum_{\mathbf{n}} Z_{\mathbf{mn}}^{\text{self},pp}(\omega) I_{\mathbf{n}}^{p}(\omega) + V_{\mathbf{m}}^{\text{sca},p}(\omega) \\
V_{\mathbf{m}}^{\text{sca},p}(\omega) &= \sum_{q\in\{x,y,z\}} \sum_{\mathbf{n}} Z_{\mathbf{m}-\mathbf{n}}^{pq+}(\omega)\tilde{\kappa}_{\mathbf{n}}(\omega) I_{\mathbf{n}}^{q}(\omega) + Z_{\mathbf{m}-\mathbf{n}}^{pq-}(\omega)\tilde{\kappa}_{\mathbf{n}+\Delta^q}(\omega) I_{\mathbf{n}}^{q}(\omega),
\end{aligned} \tag{21}
$$

where $V_{\mathbf{m}}^{\text{sca},p}$ is the scattered electric field tested by the volumetric rooftop function $\mathbf{f}_{\mathbf{m}}^{p}$ and

$$
\begin{aligned}
Z_{\mathbf{m}-\mathbf{n}}^{pq+}(\omega) &= -\omega^2\mu_0 \iiint_{V_{\mathbf{m}}^p} \iiint_{V_{\mathbf{n}}} \frac{\mathbf{f}_{\mathbf{m}}^{p}(\mathbf{r})\bullet\mathbf{f}_{\mathbf{n}}^{q+}(\mathbf{r}')e^{-j\omega R/c_0}}{4\pi R} dv'dv \\
&\quad + \frac{1}{\varepsilon_0} \iiint_{V_{\mathbf{m}}^p} \iiint_{V_{\mathbf{n}}} \frac{\nabla\bullet\left(\mathbf{f}_{\mathbf{m}}^{p}(\mathbf{r})\right)\nabla'\bullet\left(\mathbf{f}_{\mathbf{n}}^{q+}(\mathbf{r}')\right)e^{-j\omega R/c_0}}{4\pi R} dv'dv \\
&\quad - \frac{1}{\varepsilon_0} \iiint_{V_{\mathbf{m}}^p} \iint_{S_{\mathbf{n}}^q} \frac{\nabla\bullet\left(\mathbf{f}_{\mathbf{m}}^{p}(\mathbf{r})\right)e^{-j\omega R/c_0}}{4\pi R} ds'dv
\end{aligned} \tag{22}
$$

$$
\begin{aligned}
Z_{\mathbf{m}-\mathbf{n}}^{pq-}(\omega) = -\omega^2\mu_0 \iiint_{V_{\mathbf{m}}^p} \iiint_{V_{\mathbf{n}+\Delta^q}} \frac{\mathbf{f}_{\mathbf{m}}^{p}(\mathbf{r}) \bullet \mathbf{f}_{\mathbf{n}+\Delta^q}^{q-}(\mathbf{r}') e^{-j\omega R/c_0}}{4\pi R} dv' dv \\
+ \frac{1}{\varepsilon_0} \iiint_{V_{\mathbf{m}}^p} \iiint_{V_{\mathbf{n}+\Delta^q}} \frac{\nabla \bullet \left(\mathbf{f}_{\mathbf{m}}^{p}(\mathbf{r})\right) \nabla' \bullet \left(\mathbf{f}_{\mathbf{n}+\Delta^q}^{q-}(\mathbf{r}')\right) e^{-j\omega R/c_0}}{4\pi R} dv' dv \\
+ \frac{1}{\varepsilon_0} \iiint_{V_{\mathbf{m}}^p} \iint_{S_{\mathbf{n}}^q} \frac{\nabla \bullet \left(\mathbf{f}_{\mathbf{m}}^{p}(\mathbf{r})\right) e^{-j\omega R/c_0}}{4\pi R} ds' dv.
\end{aligned}
\tag{23}
$$

These equations can be organized into 3-level block-Toeplitz matrix-equation form and the multiplications in (21) can be accelerated using 3-D FFTs as follows:

$$
\widehat{\mathbf{V}}^{\mathrm{sca},p}(\omega) = \mathrm{IFFT}_{3\mathrm{D}} \left\{ \sum_{q \in \{\mathrm{x,y,z}\}} \left[\begin{array}{l} \mathrm{FFT}_{3\mathrm{D}} \left\{ \widehat{\mathbf{Z}}^{pq+}(\omega) \right\} \bullet \mathrm{FFT}_{3\mathrm{D}} \left\{ \widehat{\boldsymbol{\kappa}}^{q+}(\omega) \bullet \widehat{\mathbf{I}}^{q}(\omega) \right\} \\ + \mathrm{FFT}_{3\mathrm{D}} \left\{ \widehat{\mathbf{Z}}^{pq-}(\omega) \right\} \bullet \mathrm{FFT}_{3\mathrm{D}} \left\{ \widehat{\boldsymbol{\kappa}}^{q-}(\omega) \bullet \widehat{\mathbf{I}}^{q}(\omega) \right\} \end{array} \right] \right\} \tag{24}
$$

for $p \in \{\mathrm{x,y,z}\}$. Here, $\bullet$ denotes element-wise multiplication and $\widehat{\mathbf{V}}^{\mathrm{sca},p}$, $\widehat{\mathbf{I}}^{q}$, $\widehat{\boldsymbol{\kappa}}^{q\pm}$, and $\widehat{\mathbf{Z}}^{pq\pm}$ are 3-D arrays of size $N_{\text{CG-FFT}} = (2N_{\mathrm{x}}-1)\times(2N_{\mathrm{y}}-1)\times(2N_{\mathrm{z}}-1)$ whose entries are

$$\widehat{\mathbf{V}}^{\mathrm{sca},p}[i,j,k]=\begin{cases}V^{\mathrm{sca},p}_{(i,j,k)} & \text{if } 1\le i\le N_{\mathrm{x}}-\hat{\mathbf{p}}\bullet\hat{\mathbf{x}},\ 1\le j\le N_{\mathrm{y}}-\hat{\mathbf{p}}\bullet\hat{\mathbf{y}},\ 1\le k\le N_{\mathrm{z}}-\hat{\mathbf{p}}\bullet\hat{\mathbf{z}}\\ \times & \text{otherwise}\end{cases}$$

$$\widehat{\mathbf{I}}^{q}[i,j,k]=\begin{cases}I^{q}_{(i,j,k)} & \text{if } 1\le i\le N_{\mathrm{x}}-\hat{\mathbf{q}}\bullet\hat{\mathbf{x}},\ 1\le j\le N_{\mathrm{y}}-\hat{\mathbf{q}}\bullet\hat{\mathbf{y}},\ 1\le k\le N_{\mathrm{z}}-\hat{\mathbf{q}}\bullet\hat{\mathbf{z}}\\ 0 & \text{otherwise}\end{cases}$$

$$\widehat{\boldsymbol{\kappa}}^{q+}[i,j,k]=\begin{cases}\tilde{\kappa}_{(i,j,k)} & \text{if } 1\le i\le N_{\mathrm{x}}-\hat{\mathbf{q}}\bullet\hat{\mathbf{x}},\ 1\le j\le N_{\mathrm{y}}-\hat{\mathbf{q}}\bullet\hat{\mathbf{y}},\ 1\le k\le N_{\mathrm{z}}-\hat{\mathbf{q}}\bullet\hat{\mathbf{z}}\\ 0 & \text{otherwise}\end{cases}$$

$$\widehat{\boldsymbol{\kappa}}^{q-}[i,j,k]=\begin{cases}\tilde{\kappa}_{(i,j,k)+\boldsymbol{\Delta}^{q}} & \text{if } 1\le i\le N_{\mathrm{x}}-\hat{\mathbf{q}}\bullet\hat{\mathbf{x}},\ 1\le j\le N_{\mathrm{y}}-\hat{\mathbf{q}}\bullet\hat{\mathbf{y}},\ 1\le k\le N_{\mathrm{z}}-\hat{\mathbf{q}}\bullet\hat{\mathbf{z}}\\ 0 & \text{otherwise}\end{cases}$$

$$\widehat{\mathbf{Z}}^{pq\pm}[i,j,k]=\begin{cases}Z^{pq\pm}_{(i-1,j-1,k-1)} & \text{if } i\in S^{\mathrm{x}}_1,\ j\in S^{\mathrm{y}}_1,\ k\in S^{\mathrm{z}}_1\\ Z^{pq\pm}_{(i-2N_{\mathrm{x}},j-1,k-1)} & \text{if } i\in S^{\mathrm{x}}_2,\ j\in S^{\mathrm{y}}_1,\ k\in S^{\mathrm{z}}_1\\ Z^{pq\pm}_{(i-1,j-2N_{\mathrm{y}},k-1)} & \text{if } i\in S^{\mathrm{x}}_1,\ j\in S^{\mathrm{y}}_2,\ k\in S^{\mathrm{z}}_1\\ Z^{pq\pm}_{(i-2N_{\mathrm{x}},j-2N_{\mathrm{y}},k-1)} & \text{if } i\in S^{\mathrm{x}}_2,\ j\in S^{\mathrm{y}}_2,\ k\in S^{\mathrm{z}}_1\\ Z^{pq\pm}_{(i-1,j-1,k-2N_{\mathrm{z}})} & \text{if } i\in S^{\mathrm{x}}_1,\ j\in S^{\mathrm{y}}_1,\ k\in S^{\mathrm{z}}_2\\ Z^{pq\pm}_{(i-2N_{\mathrm{x}},j-1,k-2N_{\mathrm{z}})} & \text{if } i\in S^{\mathrm{x}}_2,\ j\in S^{\mathrm{y}}_1,\ k\in S^{\mathrm{z}}_2\\ Z^{pq\pm}_{(i-1,j-2N_{\mathrm{y}},k-2N_{\mathrm{z}})} & \text{if } i\in S^{\mathrm{x}}_1,\ j\in S^{\mathrm{y}}_2,\ k\in S^{\mathrm{z}}_2\\ Z^{pq\pm}_{(i-2N_{\mathrm{x}},j-2N_{\mathrm{y}},k-2N_{\mathrm{z}})} & \text{if } i\in S^{\mathrm{x}}_2,\ j\in S^{\mathrm{y}}_2,\ k\in S^{\mathrm{z}}_2\end{cases}\tag{25}$$

for $(i,j,k)\in\left\{(1,1,1),\ldots,\left(2N_{\mathrm{x}}-1,2N_{\mathrm{y}}-1,2N_{\mathrm{z}}-1\right)\right\}$. In (25), the sets are given as

$$\begin{aligned}&S^{\mathrm{x}}_1=\{1,\ldots,N_{\mathrm{x}}\},\ S^{\mathrm{x}}_2=\{N_{\mathrm{x}}+1,\ldots,2N_{\mathrm{x}}-1\}\\ &S^{\mathrm{y}}_1=\{1,\ldots,N_{\mathrm{y}}\},\ S^{\mathrm{y}}_2=\{N_{\mathrm{y}}+1,\ldots,2N_{\mathrm{y}}-1\}\\ &S^{\mathrm{z}}_1=\{1,\ldots,N_{\mathrm{z}}\},\ S^{\mathrm{z}}_2=\{N_{\mathrm{z}}+1,\ldots,2N_{\mathrm{z}}-1\}.\end{aligned}\tag{26}$$

It should be observed that in (25) the $\widehat{\mathbf{Z}}^{pq\pm}$ arrays are filled by computing $Z^{pq\pm}_{\mathbf{m}-\mathbf{n}}$ terms such that $\mathbf{m}-\mathbf{n}$ values are in the set

$$\mathbf{m}-\mathbf{n}\in\left\{(i,j,k)\middle|1-N_{\mathrm{x}}\le i\le N_{\mathrm{x}}-1,\ 1-N_{\mathrm{y}}\le j\le N_{\mathrm{y}}-1,\ 1-N_{\mathrm{z}}\le k\le N_{\mathrm{z}}-1\right\}.\tag{27}$$

Because of the translational invariance of the terms, they can be computed in various ways, e.g., by setting $\mathbf{n}=(0,0,0)$ and varying $\mathbf{m}$ or by setting $\mathbf{m}=(1,1,1)$ and varying $\mathbf{n}$. Note that the unique values that $\mathbf{m}-\mathbf{n}$ can take for all basis/testing functions on the mesh are limited to the smaller set

$$\mathbf{m}-\mathbf{n}\in\left\{(i,j,k)\left|\begin{array}{l}1-N_{\mathrm{x}}+\hat{\mathbf{q}}\bullet\hat{\mathbf{x}}\le i\le N_{\mathrm{x}}-\hat{\mathbf{p}}\bullet\hat{\mathbf{x}}-1,\\ 1-N_{\mathrm{y}}+\hat{\mathbf{q}}\bullet\hat{\mathbf{y}}\le j\le N_{\mathrm{y}}-\hat{\mathbf{p}}\bullet\hat{\mathbf{y}}-1,\\ 1-N_{\mathrm{z}}+\hat{\mathbf{q}}\bullet\hat{\mathbf{z}}\le k\le N_{\mathrm{z}}-\hat{\mathbf{p}}\bullet\hat{\mathbf{z}}-1\end{array}\right.\right\}\ \text{for}\ p,q\in\{\mathrm{x},\mathrm{y},\mathrm{z}\}\qquad(28)$$

which can be found using (9) and (12). That is, some of the $Z_{\mathbf{m}-\mathbf{n}}^{pq\pm}$ correspond to testing-basis function pairs that are not present in the mesh of the cuboid that encloses V. These $Z_{\mathbf{m}-\mathbf{n}}^{pq\pm}$ values arise because of the zero-padding scheme in (25) and are either multiplied by zero coefficients in $\widehat{\mathbf{I}}^{q}$ arrays or the result of the multiplication is discarded after the $\widehat{\mathbf{V}}^{\mathrm{sca},p}$ arrays are computed in (24).

The costs of computing (24) dominate the computational costs of the CG-FFT method. The self-term contribution in (21) requires negligible computations (a sparse matrix-vector multiplication) compared to the FFTs. The 18 $\widehat{\mathbf{Z}}^{pq\pm}$ matrices can be pre-FFTed and stored prior to the matrix-vector multiplications during the iterative solution. At each iteration, 6 FFTs ($\widehat{\boldsymbol{\kappa}}^{q+}\bullet\widehat{\mathbf{I}}^{q}$ and $\widehat{\boldsymbol{\kappa}}^{q-}\bullet\widehat{\mathbf{I}}^{q}$ for $q\in\{\mathrm{x},\mathrm{y},\mathrm{z}\}$) and 3 IFFTs must be performed to compute $\widehat{\mathbf{V}}^{\mathrm{sca},p}$ for $p\in\{\mathrm{x},\mathrm{y},\mathrm{z}\}$. Each FFT and IFFT requires $O\left(N_{\text{CG-FFT}}\log N_{\text{CG-FFT}}\right)$ operations.

Alternate Formulations

The above common CG-FFT formulation [33] does not include the "half" volumetric rooftop functions that are defined over only one voxel (a "boundary voxel" that is just inside V and has at least one face on the boundary of V) in the list of basis or testing functions. These missing basis/testing functions at the boundaries of the volume have an important role in the MOM system of equations and should not be left out. Indeed, leaving these functions out is tantamount to approximating the component of $\tilde{\mathbf{D}}^{\mathrm{c}}$ normal to the boundary surface as 0 at the boundary and as linearly increasing away from the boundary throughout each boundary voxel inside V. Although common CG-FFT variants that use volumetric rooftop functions do not mention any special treatment for basis or testing

functions on the boundary [20], [43], [54], various approaches can be used to address this shortcoming.

One approach might be to simply define a regular ("full") volumetric rooftop basis and testing function over each boundary voxel and its neighbor that is outside V. The multiplication with the contrast ratio (which is zero in every voxel outside of V) effectively transforms the full volumetric rooftop basis functions into half basis functions when calculating the $Z_{\mathbf{mn}}^{\mathbf{A},pq}$ and $Z_{\mathbf{mn}}^{\phi,pq}$ entries in (16) and (17). There is no contrast ratio term to transform the full basis functions into half basis functions, however, when calculating the $Z_{\mathbf{mn}}^{\text{self},pq}$ entries in (15). Thus, this alternative would yield a system of equations that is not exactly the same as the MOM system of equations. More importantly, the full volumetric rooftop basis functions at the boundaries would approximate the component of $\tilde{\mathbf{D}}^{\text{c}}$ normal to the boundary surface as a function that linearly decreases to zero from each boundary face to the opposite face of each neighboring voxel outside V [41]. Thus, compared to the common CG-FFT formulation, this formulation would replace one incorrect expansion with another incorrect (but perhaps more accurate) one.

Another approach for addressing the discrepancy between CG-FFT and MOM system of equations was proposed in [41]. In this alternative, the "full" volumetric rooftop functions defined over boundary voxels and their neighbors outside V are only used as testing functions and "mixed" volumetric functions that are half volumetric rooftop functions (defined over boundary voxels) and half volumetric pulse functions (defined over neighbor voxels outside V) are used as basis functions. This is equivalent to approximating the component of $\tilde{\mathbf{E}}^{\text{inc}}+\tilde{\mathbf{E}}^{\text{sca}}$ normal to the boundary surface as constant over each neighboring voxel outside of V. While this alternative yields a system of equations that is not exactly the same as the MOM system of equations, it should improve the agreement between CG-FFT and traditional MOM results significantly as the additional

approximation introduced is rather benign. Although this approach has negligible additional computational costs compared to the common CG-FFT formulation, the modified CG-FFT solution will still fail to match the MOM solution exactly (within machine precision).

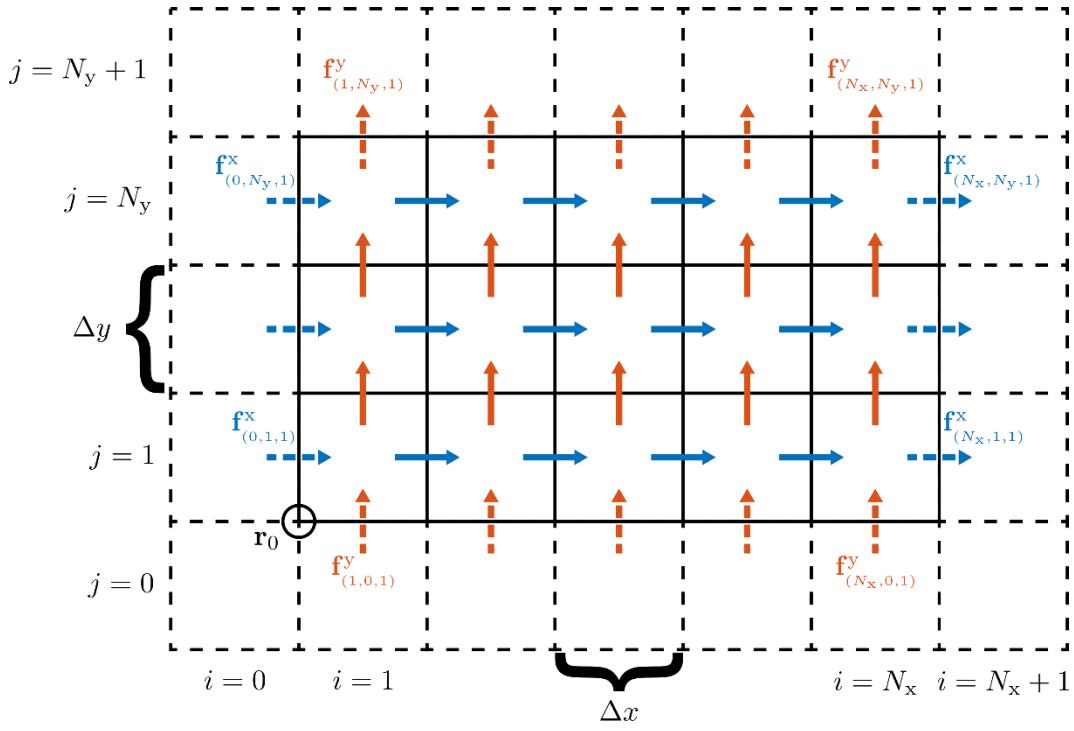

Figure 5: The notation used to refer to the volumetric rooftop functions for the GMRES-FFT formulation used in thesis. The *x*-directed (blue) and *y*-directed (orange) basis/testing functions are shown as arrows across the shared face. The additional basis/testing functions (compared to the common CG-FFT formulation in Figure 4) are shown using dashed arrows. To fit the additional basis/testing functions, the mesh is exteneded by one cell in each dimension (dashed mesh). There are $(N_x+1)\times N_y$ *x*-directed rooftop functions and $N_x\times(N_y+1)$ *y*-directed functions. The *z*-directed basis/testing functions are not shown in this 2-D cut.

Proposed GMRES-FFT Formulation

In this thesis, as detailed below, an alternative approach that exactly matches the MOM solution (within machine precision) is developed and used for the numerical

experiments. In this approach, the common CG-FFT formulation is also modified to use regular ("full") volumetric rooftop basis and testing function over each boundary voxel and its neighbor that is outside V. Importantly, however, the testing functions are contrast-weighted; thus, the resulting system of equations have 0 contributions from any voxel outside V ($\tilde{\kappa}(\omega)=0$ in the background medium by definition) and are identical to those in (7) and (8). The symmetric testing [55], [56] of the V-EFIE yields the equations in (6); using the notation introduced above to identify the orientation and location of the rooftop functions, these equations can be expressed as:

$$\begin{aligned}&\left\langle \tilde{\kappa}_m(\mathbf{r},\omega)\mathbf{f}_{\mathbf{m}}^{p}(\mathbf{r}), \frac{\tilde{\mathbf{D}}^{\mathrm{c}}(\mathbf{r},\omega)}{\tilde{\varepsilon}(\mathbf{r},\omega)} \right\rangle - \left\langle \tilde{\kappa}_m(\mathbf{r},\omega)\mathbf{f}_{\mathbf{m}}^{p}(\mathbf{r}), \tilde{\mathbf{E}}^{\mathrm{sca}}(\mathbf{r},\omega) \right\rangle \\ &\quad = \left\langle \tilde{\kappa}_m(\mathbf{r},\omega)\mathbf{f}_{\mathbf{m}}^{p}(\mathbf{r}), \tilde{\mathbf{E}}^{\mathrm{inc}}(\mathbf{r},\omega) \right\rangle\end{aligned} \tag{29}$$

where

$$\mathbf{f}_{\mathbf{m}}^{p} \in \left\{ \mathbf{f}_{(i,j,k)}^{p} \,|\, 1-\hat{\mathbf{p}}\bullet\hat{\mathbf{x}} \le i \le N_{\mathrm{x}},\ 1-\hat{\mathbf{p}}\bullet\hat{\mathbf{y}} \le j \le N_{\mathrm{y}},\ 1-\hat{\mathbf{p}}\bullet\hat{\mathbf{z}} \le k \le N_{\mathrm{z}} \right\} \text{ for } p \in \{\mathrm{x},\mathrm{y},\mathrm{z}\}. \tag{30}$$

These equations can be expressed in terms of the unknown coefficients just as in (13):

$$\sum_{q\in\{x,y,z\}} \sum_{\mathbf{n}} \left(Z_{\mathbf{mn}}^{\mathrm{self},pq}(\omega) + Z_{\mathbf{mn}}^{\mathbf{A},pq}(\omega) + Z_{\mathbf{mn}}^{\phi,pq}(\omega) \right) I_{\mathbf{n}}^{q}(\omega) = V_{\mathbf{m}}^{\mathrm{inc},p}(\omega). \tag{31}$$

Unlike (13), however, the basis functions are in the extended set

$$\mathbf{f}_{\mathbf{n}}^{q} \in \left\{ \mathbf{f}_{(i,j,k)}^{q} \,|\, 1-\hat{\mathbf{q}}\bullet\hat{\mathbf{x}} \le i \le N_{\mathrm{x}},\ 1-\hat{\mathbf{q}}\bullet\hat{\mathbf{y}} \le j \le N_{\mathrm{y}},\ 1-\hat{\mathbf{q}}\bullet\hat{\mathbf{z}} \le k \le N_{\mathrm{z}} \right\} \text{ for } q \in \{\mathrm{x},\mathrm{y},\mathrm{z}\}, \tag{32}$$

and the matrix entries are

$$V_{\mathbf{m}}^{\mathrm{inc},p}(\omega) = \iiint_{V_{\mathbf{m}}^{p}} \tilde{\kappa}_m(\mathbf{r},\omega)\mathbf{f}_{\mathbf{m}}^{p}(\mathbf{r})\bullet\tilde{\mathbf{E}}^{\mathrm{inc}}(\mathbf{r},\omega)\,dv \tag{33}$$

$$Z_{\mathbf{mn}}^{\mathrm{self},pq}(\omega) = \iiint_{V_{\mathbf{m}}^{p}} \frac{\tilde{\kappa}_m(\mathbf{r},\omega)\mathbf{f}_{\mathbf{m}}^{p}(\mathbf{r})\bullet\mathbf{f}_{\mathbf{n}}^{q}(\mathbf{r})}{\tilde{\varepsilon}_{\mathbf{n}}(\mathbf{r},\omega)}\,dv \tag{34}$$

$$Z_{\mathbf{mn}}^{\mathbf{A},pq}(\omega) = -\omega^2\mu_0 \iiint_{V_{\mathbf{m}}^{p}} \iiint_{V_{\mathbf{n}}^{q}} \frac{\tilde{\kappa}_m(\mathbf{r},\omega)\mathbf{f}_{\mathbf{m}}^{p}(\mathbf{r})\bullet\tilde{\kappa}_{\mathbf{n}}(\mathbf{r}',\omega)\mathbf{f}_{\mathbf{n}}^{q}(\mathbf{r}')e^{-j\omega R/c_0}}{4\pi R} dv'dv \tag{35}$$

$$Z_{\mathbf{mn}}^{\phi,pq}(\omega)=\frac{1}{\varepsilon_0}\iiint_{V_{\mathbf{m}}^p}\iiint_{V_{\mathbf{n}}^q}\frac{\nabla\bullet\left(\tilde{\kappa}_m(\mathbf{r},\omega)\mathbf{f}_{\mathbf{m}}^{\,p}(\mathbf{r})\right)\nabla'\bullet\left(\tilde{\kappa}_{\mathbf{n}}(\mathbf{r}',\omega)\mathbf{f}_{\mathbf{n}}^{\,q}(\mathbf{r}')\right)e^{-j\omega R/c_0}}{4\pi R}dv'dv. \qquad (36)$$

Next, as before, the basis functions are separated into two pieces such that $\tilde{\kappa}$ is constant for each piece; now, the testing functions $\mathbf{f}_{\mathbf{m}}^{\,p}$ are also separated in two pieces: $\mathbf{f}_{\mathbf{m}}^{\,p+}$ and $\mathbf{f}_{\mathbf{m}+\Delta^p}^{\,p-}$, whose support are $V_{\mathbf{m}}$ and $V_{\mathbf{m}+\Delta^p}$, respectively. The contrast ratio $\tilde{\kappa}_{\mathbf{m}}(\mathbf{r},\omega)$ is equal to $\tilde{\kappa}_{\mathbf{m}}(\omega)$ in the first voxel and $\tilde{\kappa}_{\mathbf{m}+\Delta^p}(\omega)$ in the second one. Thus, just as in (18)-(20), the integrals can be rewritten as:

$$Z_{\mathbf{mn}}^{\mathbf{A},pq}(\omega)=-\omega^2\mu_0\left\{\begin{array}{l}\tilde{\kappa}_{\mathbf{m}}(\omega)\tilde{\kappa}_{\mathbf{n}}(\omega)\iiint_{V_{\mathbf{m}}}\iiint_{V_{\mathbf{n}}}\frac{\mathbf{f}_{\mathbf{m}}^{\,p+}(\mathbf{r})\bullet\mathbf{f}_{\mathbf{n}}^{\,q+}(\mathbf{r}')e^{-j\omega R/c_0}}{4\pi R}dv'dv\\ +\tilde{\kappa}_{\mathbf{m}}(\omega)\tilde{\kappa}_{\mathbf{n}+\Delta^q}(\omega)\iiint_{V_{\mathbf{m}}}\iiint_{V_{\mathbf{n}+\Delta^q}}\frac{\mathbf{f}_{\mathbf{m}}^{\,p+}(\mathbf{r})\bullet\mathbf{f}_{\mathbf{n}+\Delta^q}^{\,q-}(\mathbf{r}')e^{-j\omega R/c_0}}{4\pi R}dv'dv\\ +\tilde{\kappa}_{\mathbf{m}+\Delta^p}(\omega)\tilde{\kappa}_{\mathbf{n}}(\omega)\iiint_{V_{\mathbf{m}+\Delta^p}}\iiint_{V_{\mathbf{n}}}\frac{\mathbf{f}_{\mathbf{m}+\Delta^p}^{\,p-}(\mathbf{r})\bullet\mathbf{f}_{\mathbf{n}}^{\,q+}(\mathbf{r}')e^{-j\omega R/c_0}}{4\pi R}dv'dv\\ +\tilde{\kappa}_{\mathbf{m}+\Delta^p}(\omega)\tilde{\kappa}_{\mathbf{n}+\Delta^q}(\omega)\iiint_{V_{\mathbf{m}+\Delta^p}}\iiint_{V_{\mathbf{n}+\Delta^q}}\frac{\mathbf{f}_{\mathbf{m}+\Delta^p}^{\,p-}(\mathbf{r})\bullet\mathbf{f}_{\mathbf{n}+\Delta^q}^{\,q-}(\mathbf{r}')e^{-j\omega R/c_0}}{4\pi R}dv'dv\end{array}\right\} \qquad (37)$$

$$
\begin{aligned}
Z_{\mathbf{mn}}^{\phi,pq}(\omega) = \frac{\tilde{\kappa}_{\mathbf{m}}(\omega)\tilde{\kappa}_{\mathbf{n}}(\omega)}{\varepsilon_0}
&\left\{
\begin{aligned}
&\iiint_{V_{\mathbf{m}}}\iiint_{V_{\mathbf{n}}} \frac{\nabla\bullet\left(\mathbf{f}_{\mathbf{m}}^{p+}(\mathbf{r})\right)\nabla'\bullet\left(\mathbf{f}_{\mathbf{n}}^{q+}(\mathbf{r}')\right)e^{-j\omega R/c_0}}{4\pi R}\,dv'dv \\
&-\iiint_{V_{\mathbf{m}}}\iint_{S_{\mathbf{n}}^{q}} \frac{\nabla\bullet\left(\mathbf{f}_{\mathbf{m}}^{p+}(\mathbf{r})\right)e^{-j\omega R/c_0}}{4\pi R}\,ds'dv \\
&-\iint_{S_{\mathbf{m}}^{p}}\iiint_{V_{\mathbf{n}}} \frac{\nabla'\bullet\left(\mathbf{f}_{\mathbf{n}}^{q+}(\mathbf{r}')\right)e^{-j\omega R/c_0}}{4\pi R}\,dv'ds + \iint_{S_{\mathbf{m}}^{p}}\iint_{S_{\mathbf{n}}^{q}} \frac{e^{-j\omega R/c_0}}{4\pi R}\,ds'ds
\end{aligned}
\right\} \\
+\frac{\tilde{\kappa}_{\mathbf{m}}(\omega)\tilde{\kappa}_{\mathbf{n}+\Delta^q}(\omega)}{\varepsilon_0}
&\left\{
\begin{aligned}
&\iiint_{V_{\mathbf{m}}}\iiint_{V_{\mathbf{n}+\Delta^q}} \frac{\nabla\bullet\left(\mathbf{f}_{\mathbf{m}}^{p+}(\mathbf{r})\right)\nabla'\bullet\left(\mathbf{f}_{\mathbf{n}+\Delta^q}^{q-}(\mathbf{r}')\right)e^{-j\omega R/c_0}}{4\pi R}\,dv'dv \\
&+\iiint_{V_{\mathbf{m}}}\iint_{S_{\mathbf{n}}^{q}} \frac{\nabla\bullet\left(\mathbf{f}_{\mathbf{m}}^{p+}(\mathbf{r})\right)e^{-j\omega R/c_0}}{4\pi R}\,ds'dv \\
&-\iint_{S_{\mathbf{m}}^{p}}\iiint_{V_{\mathbf{n}+\Delta^q}} \frac{\nabla'\bullet\left(\mathbf{f}_{\mathbf{n}+\Delta^q}^{q-}(\mathbf{r}')\right)e^{-j\omega R/c_0}}{4\pi R}\,dv'ds - \iint_{S_{\mathbf{m}}^{p}}\iint_{S_{\mathbf{n}}^{q}} \frac{e^{-j\omega R/c_0}}{4\pi R}\,ds'ds
\end{aligned}
\right\} \\
+\frac{\tilde{\kappa}_{\mathbf{m}+\Delta^p}(\omega)\tilde{\kappa}_{\mathbf{n}}(\omega)}{\varepsilon_0}
&\left\{
\begin{aligned}
&\iiint_{V_{\mathbf{m}+\Delta^p}}\iiint_{V_{\mathbf{n}}} \frac{\nabla\bullet\left(\mathbf{f}_{\mathbf{m}+\Delta^p}^{p-}(\mathbf{r})\right)\nabla'\bullet\left(\mathbf{f}_{\mathbf{n}}^{q+}(\mathbf{r}')\right)e^{-j\omega R/c_0}}{4\pi R}\,dv'dv \\
&-\iiint_{V_{\mathbf{m}+\Delta^p}}\iint_{S_{\mathbf{n}}^{q}} \frac{\nabla\bullet\left(\mathbf{f}_{\mathbf{m}+\Delta^p}^{p-}(\mathbf{r})\right)e^{-j\omega R/c_0}}{4\pi R}\,ds'dv \\
&+\iint_{S_{\mathbf{m}}^{p}}\iiint_{V_{\mathbf{n}}} \frac{\nabla'\bullet\left(\mathbf{f}_{\mathbf{n}}^{q+}(\mathbf{r}')\right)e^{-j\omega R/c_0}}{4\pi R}\,dv'ds - \iint_{S_{\mathbf{m}}^{p}}\iint_{S_{\mathbf{n}}^{q}} \frac{e^{-j\omega R/c_0}}{4\pi R}\,ds'ds
\end{aligned}
\right\} \\
+\frac{\tilde{\kappa}_{\mathbf{m}+\Delta^p}(\omega)\tilde{\kappa}_{\mathbf{n}+\Delta^q}(\omega)}{\varepsilon_0}
&\left\{
\begin{aligned}
&\iiint_{V_{\mathbf{m}+\Delta^p}}\iiint_{V_{\mathbf{n}+\Delta^q}} \frac{\nabla\bullet\left(\mathbf{f}_{\mathbf{m}+\Delta^p}^{p-}(\mathbf{r})\right)\nabla'\bullet\left(\mathbf{f}_{\mathbf{n}+\Delta^q}^{q-}(\mathbf{r}')\right)e^{-j\omega R/c_0}}{4\pi R}\,dv'dv \\
&+\iiint_{V_{\mathbf{m}+\Delta^p}}\iint_{S_{\mathbf{n}}^{q}} \frac{\nabla\bullet\left(\mathbf{f}_{\mathbf{m}+\Delta^p}^{p-}(\mathbf{r})\right)e^{-j\omega R/c_0}}{4\pi R}\,ds'dv \\
&+\iint_{S_{\mathbf{m}}^{p}}\iiint_{V_{\mathbf{n}+\Delta^q}} \frac{\nabla'\bullet\left(\mathbf{f}_{\mathbf{n}+\Delta^q}^{q-}(\mathbf{r}')\right)e^{-j\omega R/c_0}}{4\pi R}\,dv'ds + \iint_{S_{\mathbf{m}}^{p}}\iint_{S_{\mathbf{n}}^{q}} \frac{e^{-j\omega R/c_0}}{4\pi R}\,ds'ds
\end{aligned}
\right\}.
\end{aligned}
\tag{38}
$$

To emphasize the translational invariance of the integrals in (37) and the terms within curly brackets of (38), (31) can be expressed as

$$
\begin{aligned}
V_{\mathbf{m}}^{\mathrm{inc},p}(\omega) &= \sum_{\mathbf{n}} Z_{\mathbf{mn}}^{\mathrm{self},pp}(\omega) I_{\mathbf{n}}^{p} + V_{\mathbf{m}}^{\mathrm{sca},p}(\omega) \\
V_{\mathbf{m}}^{\mathrm{sca},p}(\omega) &= \sum_{q\in\{x,y,z\}} \sum_{\mathbf{n}} \begin{pmatrix}
\tilde{\kappa}_{\mathbf{m}}(\omega) Z_{\mathbf{m-n}}^{pq++}(\omega) \tilde{\kappa}_{\mathbf{n}}(\omega) I_{\mathbf{n}}^{q}(\omega) \\
+\tilde{\kappa}_{\mathbf{m}}(\omega) Z_{\mathbf{m-n}}^{pq+-}(\omega) \tilde{\kappa}_{\mathbf{n}+\Delta^q}(\omega) I_{\mathbf{n}}^{q}(\omega) \\
+\tilde{\kappa}_{\mathbf{m}+\Delta^p}(\omega) Z_{\mathbf{m-n}}^{pq-+}(\omega) \tilde{\kappa}_{\mathbf{n}}(\omega) I_{\mathbf{n}}^{q}(\omega) \\
+\tilde{\kappa}_{\mathbf{m}+\Delta^p}(\omega) Z_{\mathbf{m-n}}^{pq--}(\omega) \tilde{\kappa}_{\mathbf{n}+\Delta^q}(\omega) I_{\mathbf{n}}^{q}(\omega)
\end{pmatrix},
\end{aligned}
\tag{39}
$$

where

$$
Z_{\mathbf{m-n}}^{pq++}(\omega) = \left\{ \begin{aligned}
&-\omega^2 \mu_0 \iiint_{V_{\mathbf{m}}} \iiint_{V_{\mathbf{n}}} \frac{\mathbf{f}_{\mathbf{m}}^{p+}(\mathbf{r}) \bullet \mathbf{f}_{\mathbf{n}}^{q+}(\mathbf{r}') e^{-j\omega R/c_0}}{4\pi R} dv' dv \\
&+\frac{1}{\varepsilon_0} \iiint_{V_{\mathbf{m}}} \iiint_{V_{\mathbf{n}}} \frac{\nabla \bullet \left(\mathbf{f}_{\mathbf{m}}^{p+}(\mathbf{r})\right) \nabla' \bullet \left(\mathbf{f}_{\mathbf{n}}^{q+}(\mathbf{r}')\right) e^{-j\omega R/c_0}}{4\pi R} dv' dv \\
&-\frac{1}{\varepsilon_0} \iiint_{V_{\mathbf{m}}} \iint_{S_{\mathbf{n}}^{q}} \frac{\nabla \bullet \left(\mathbf{f}_{\mathbf{m}}^{p+}(\mathbf{r})\right) e^{-j\omega R/c_0}}{4\pi R} ds' dv \\
&-\frac{1}{\varepsilon_0} \iint_{S_{\mathbf{m}}^{p}} \iiint_{V_{\mathbf{n}}} \frac{\nabla' \bullet \left(\mathbf{f}_{\mathbf{n}}^{q+}(\mathbf{r}')\right) e^{-j\omega R/c_0}}{4\pi R} dv' ds + \frac{1}{\varepsilon_0} \iint_{S_{\mathbf{m}}^{p}} \iint_{S_{\mathbf{n}}^{q}} \frac{e^{-j\omega R/c_0}}{4\pi R} ds' ds
\end{aligned} \right\}
\tag{40}
$$

$$
Z_{\mathbf{m-n}}^{pq+-}(\omega) = \left\{ \begin{aligned}
&-\omega^2 \mu_0 \iiint_{V_{\mathbf{m}}} \iiint_{V_{\mathbf{n}+\Delta^q}} \frac{\mathbf{f}_{\mathbf{m}}^{p+}(\mathbf{r}) \bullet \mathbf{f}_{\mathbf{n}+\Delta^q}^{q-}(\mathbf{r}') e^{-j\omega R/c_0}}{4\pi R} dv' dv \\
&+\frac{1}{\varepsilon_0} \iiint_{V_{\mathbf{m}}} \iiint_{V_{\mathbf{n}+\Delta^q}} \frac{\nabla \bullet \left(\mathbf{f}_{\mathbf{m}}^{p+}(\mathbf{r})\right) \nabla' \bullet \left(\mathbf{f}_{\mathbf{n}+\Delta^q}^{q-}(\mathbf{r}')\right) e^{-j\omega R/c_0}}{4\pi R} dv' dv \\
&+\frac{1}{\varepsilon_0} \iiint_{V_{\mathbf{m}}} \iint_{S_{\mathbf{n}}^{q}} \frac{\nabla \bullet \left(\mathbf{f}_{\mathbf{m}}^{p+}(\mathbf{r})\right) e^{-j\omega R/c_0}}{4\pi R} ds' dv \\
&-\frac{1}{\varepsilon_0} \iint_{S_{\mathbf{m}}^{p}} \iiint_{V_{\mathbf{n}+\Delta^q}} \frac{\nabla' \bullet \left(\mathbf{f}_{\mathbf{n}+\Delta^q}^{q-}(\mathbf{r}')\right) e^{-j\omega R/c_0}}{4\pi R} dv' ds - \frac{1}{\varepsilon_0} \iint_{S_{\mathbf{m}}^{p}} \iint_{S_{\mathbf{n}}^{q}} \frac{e^{-j\omega R/c_0}}{4\pi R} ds' ds
\end{aligned} \right\}
\tag{41}
$$

$$Z_{\mathbf{m}-\mathbf{n}}^{pq-+}(\omega)=\left\{\begin{array}{l}-\omega^2\mu_0\iiint\limits_{V_{\mathbf{m}+\Delta^p}}\iiint\limits_{V_{\mathbf{n}}}\frac{\mathbf{f}_{\mathbf{m}+\Delta^p}^{p-}(\mathbf{r})\bullet\mathbf{f}_{\mathbf{n}}^{q+}(\mathbf{r}')e^{-j\omega R/c_0}}{4\pi R}dv'dv\\+\frac{1}{\varepsilon_0}\iiint\limits_{V_{\mathbf{m}+\Delta^p}}\iiint\limits_{V_{\mathbf{n}}}\frac{\nabla\bullet\left(\mathbf{f}_{\mathbf{m}+\Delta^p}^{p-}(\mathbf{r})\right)\nabla'\bullet\left(\mathbf{f}_{\mathbf{n}}^{q+}(\mathbf{r}')\right)e^{-j\omega R/c_0}}{4\pi R}dv'dv\\-\frac{1}{\varepsilon_0}\iiint\limits_{V_{\mathbf{m}+\Delta^p}}\iint\limits_{S_{\mathbf{n}}^q}\frac{\nabla\bullet\left(\mathbf{f}_{\mathbf{m}+\Delta^p}^{p-}(\mathbf{r})\right)e^{-j\omega R/c_0}}{4\pi R}ds'dv\\+\frac{1}{\varepsilon_0}\iint\limits_{S_{\mathbf{m}}^p}\iiint\limits_{V_{\mathbf{n}}}\frac{\nabla'\bullet\left(\mathbf{f}_{\mathbf{n}}^{q+}(\mathbf{r}')\right)e^{-j\omega R/c_0}}{4\pi R}dv'ds-\frac{1}{\varepsilon_0}\iint\limits_{S_{\mathbf{m}}^p}\iint\limits_{S_{\mathbf{n}}^q}\frac{e^{-j\omega R/c_0}}{4\pi R}ds'ds\end{array}\right\} \tag{42}$$

$$Z_{\mathbf{m}-\mathbf{n}}^{pq--}(\omega)=\left\{\begin{array}{l}-\omega^2\mu_0\iiint\limits_{V_{\mathbf{m}+\Delta^p}}\iiint\limits_{V_{\mathbf{n}+\Delta^q}}\frac{\mathbf{f}_{\mathbf{m}+\Delta^p}^{p-}(\mathbf{r})\bullet\mathbf{f}_{\mathbf{n}+\Delta^q}^{q-}(\mathbf{r}')e^{-j\omega R/c_0}}{4\pi R}dv'dv\\+\frac{1}{\varepsilon_0}\iiint\limits_{V_{\mathbf{m}+\Delta^p}}\iiint\limits_{V_{\mathbf{n}+\Delta^q}}\frac{\nabla\bullet\left(\mathbf{f}_{\mathbf{m}+\Delta^p}^{p-}(\mathbf{r})\right)\nabla'\bullet\left(\mathbf{f}_{\mathbf{n}+\Delta^q}^{q-}(\mathbf{r}')\right)e^{-j\omega R/c_0}}{4\pi R}dv'dv\\+\frac{1}{\varepsilon_0}\iiint\limits_{V_{\mathbf{m}+\Delta^p}}\iint\limits_{S_{\mathbf{n}}^q}\frac{\nabla\bullet\left(\mathbf{f}_{\mathbf{m}+\Delta^p}^{p-}(\mathbf{r})\right)e^{-j\omega R/c_0}}{4\pi R}ds'dv\\+\frac{1}{\varepsilon_0}\iint\limits_{S_{\mathbf{m}}^p}\iiint\limits_{V_{\mathbf{n}+\Delta^q}}\frac{\nabla'\bullet\left(\mathbf{f}_{\mathbf{n}+\Delta^q}^{q-}(\mathbf{r}')\right)e^{-j\omega R/c_0}}{4\pi R}dv'ds+\frac{1}{\varepsilon_0}\iint\limits_{S_{\mathbf{m}}^p}\iint\limits_{S_{\mathbf{n}}^q}\frac{e^{-j\omega R/c_0}}{4\pi R}ds'ds\end{array}\right\}. \tag{43}$$

Next, these equations are organized into 3-level block-Toeplitz form and the multiplications in (39) are accelerated using 3-D FFTs:

$$\begin{aligned}\widehat{\mathbf{V}}^{\mathrm{sca},p}(\omega)=&\\&\widehat{\boldsymbol{\kappa}}^{p+}(\omega)\bullet\mathrm{IFFT}_{3\mathrm{D}}\left\{\sum_{q\in\{x,y,z\}}\left[\begin{array}{l}\mathrm{FFT}_{3\mathrm{D}}\left\{\widehat{\mathbf{Z}}_{\mathbf{m}-\mathbf{n}}^{pq++}(\omega)\right\}\bullet\mathrm{FFT}_{3\mathrm{D}}\left\{\widehat{\boldsymbol{\kappa}}^{q+}(\omega)\bullet\widehat{\mathbf{I}}_{\mathbf{n}}^{q}(\omega)\right\}\\+\mathrm{FFT}_{3\mathrm{D}}\left\{\widehat{\mathbf{Z}}_{\mathbf{m}-\mathbf{n}}^{pq+-}(\omega)\right\}\bullet\mathrm{FFT}_{3\mathrm{D}}\left\{\widehat{\boldsymbol{\kappa}}^{q-}(\omega)\bullet\widehat{\mathbf{I}}_{\mathbf{n}}^{q}(\omega)\right\}\end{array}\right]\right\}\\&+\widehat{\boldsymbol{\kappa}}^{p-}(\omega)\bullet\mathrm{IFFT}_{3\mathrm{D}}\left\{\sum_{q\in\{x,y,z\}}\left[\begin{array}{l}\mathrm{FFT}_{3\mathrm{D}}\left\{\widehat{\mathbf{Z}}_{\mathbf{m}-\mathbf{n}}^{pq-+}(\omega)\right\}\bullet\mathrm{FFT}_{3\mathrm{D}}\left\{\widehat{\boldsymbol{\kappa}}^{q+}(\omega)\bullet\widehat{\mathbf{I}}_{\mathbf{n}}^{q}(\omega)\right\}\\+\mathrm{FFT}_{3\mathrm{D}}\left\{\widehat{\mathbf{Z}}_{\mathbf{m}-\mathbf{n}}^{pq--}(\omega)\right\}\bullet\mathrm{FFT}_{3\mathrm{D}}\left\{\widehat{\boldsymbol{\kappa}}^{q-}(\omega)\bullet\widehat{\mathbf{I}}_{\mathbf{n}}^{q}(\omega)\right\}\end{array}\right]\right\}\end{aligned} \tag{44}$$

for $p\in\{\mathrm{x},\mathrm{y},\mathrm{z}\}$. Here, $\widehat{\mathbf{V}}^{\mathrm{sca},p}$, $\widehat{\mathbf{I}}^{q}$, $\widehat{\boldsymbol{\kappa}}^{q\pm}$, $\widehat{\boldsymbol{\kappa}}^{p\pm}$ and $\widehat{\mathbf{Z}}^{pq\pm\pm}$ are 3-D arrays of size $N_{\text{GMRES-FFT}}=(2N_{\mathrm{x}}+1)\times(2N_{\mathrm{y}}+1)\times(2N_{\mathrm{z}}+1)$ whose entries are

$$\widehat{\mathbf{V}}^{\mathrm{sca},p}[i,j,k]=\begin{cases}V^{\mathrm{sca},p}_{(i,j,k)} & \text{if } 1-\hat{\mathbf{p}}\bullet\hat{\mathbf{x}}\le i\le N_{\mathrm{x}},\ 1-\hat{\mathbf{p}}\bullet\hat{\mathbf{y}}\le j\le N_{\mathrm{y}},\ 1-\hat{\mathbf{p}}\bullet\hat{\mathbf{z}}\le k\le N_{\mathrm{z}}\\ \times & \text{otherwise}\end{cases}$$

$$\widehat{\boldsymbol{\kappa}}^{p+}[i,j,k]=\begin{cases}\tilde{\kappa}_{(i,j,k)} & \text{if } 1-\hat{\mathbf{p}}\bullet\hat{\mathbf{x}}\le i\le N_{\mathrm{x}},\ 1-\hat{\mathbf{p}}\bullet\hat{\mathbf{y}}\le j\le N_{\mathrm{y}},\ 1-\hat{\mathbf{p}}\bullet\hat{\mathbf{z}}\le k\le N_{\mathrm{z}}\\ 0 & \text{otherwise}\end{cases}$$

$$\widehat{\boldsymbol{\kappa}}^{p-}[i,j,k]=\begin{cases}\tilde{\kappa}_{(i,j,k)+\boldsymbol{\Delta}^{p}} & \text{if } 1-\hat{\mathbf{p}}\bullet\hat{\mathbf{x}}\le i\le N_{\mathrm{x}},\ 1-\hat{\mathbf{p}}\bullet\hat{\mathbf{y}}\le j\le N_{\mathrm{y}},\ 1-\hat{\mathbf{p}}\bullet\hat{\mathbf{z}}\le k\le N_{\mathrm{z}}\\ 0 & \text{otherwise}\end{cases}$$

$$\widehat{\mathbf{I}}^{q}[i,j,k]=\begin{cases}I^{q}_{(i,j,k)} & \text{if } 1-\hat{\mathbf{q}}\bullet\hat{\mathbf{x}}\le i\le N_{\mathrm{x}},\ 1-\hat{\mathbf{q}}\bullet\hat{\mathbf{y}}\le j\le N_{\mathrm{y}},\ 1-\hat{\mathbf{q}}\bullet\hat{\mathbf{z}}\le k\le N_{\mathrm{z}}\\ 0 & \text{otherwise}\end{cases}$$

$$\widehat{\boldsymbol{\kappa}}^{q+}[i,j,k]=\begin{cases}\tilde{\kappa}_{(i,j,k)} & \text{if } 1-\hat{\mathbf{q}}\bullet\hat{\mathbf{x}}\le i\le N_{\mathrm{x}},\ 1-\hat{\mathbf{q}}\bullet\hat{\mathbf{y}}\le j\le N_{\mathrm{y}},\ 1-\hat{\mathbf{q}}\bullet\hat{\mathbf{z}}\le k\le N_{\mathrm{z}}\\ 0 & \text{otherwise}\end{cases}$$

$$\widehat{\boldsymbol{\kappa}}^{q-}[i,j,k]=\begin{cases}\tilde{\kappa}_{(i,j,k)+\boldsymbol{\Delta}^{q}} & \text{if } 1-\hat{\mathbf{q}}\bullet\hat{\mathbf{x}}\le i\le N_{\mathrm{x}},\ 1-\hat{\mathbf{q}}\bullet\hat{\mathbf{y}}\le j\le N_{\mathrm{y}},\ 1-\hat{\mathbf{q}}\bullet\hat{\mathbf{z}}\le k\le N_{\mathrm{z}}\\ 0 & \text{otherwise}\end{cases}$$

$$\widehat{\mathbf{Z}}^{pq\pm\pm}[i,j,k]=\begin{cases}Z^{pq\pm}_{(i-1,j-1,k-1)} & \text{if } i\in S_1^{\mathrm{x}},\ j\in S_1^{\mathrm{y}},\ k\in S_1^{\mathrm{z}}\\ Z^{pq\pm}_{(i-2N_{\mathrm{x}},j-1,k-1)} & \text{if } i\in S_2^{\mathrm{x}},\ j\in S_1^{\mathrm{y}},\ k\in S_1^{\mathrm{z}}\\ Z^{pq\pm}_{(i-1,j-2N_{\mathrm{y}},k-1)} & \text{if } i\in S_1^{\mathrm{x}},\ j\in S_2^{\mathrm{y}},\ k\in S_1^{\mathrm{z}}\\ Z^{pq\pm}_{(i-2N_{\mathrm{x}},j-2N_{\mathrm{y}},k-1)} & \text{if } i\in S_2^{\mathrm{x}},\ j\in S_2^{\mathrm{y}},\ k\in S_1^{\mathrm{z}}\\ Z^{pq\pm}_{(i-1,j-1,k-2N_{\mathrm{z}})} & \text{if } i\in S_1^{\mathrm{x}},\ j\in S_1^{\mathrm{y}},\ k\in S_2^{\mathrm{z}}\\ Z^{pq\pm}_{(i-2N_{\mathrm{x}},j-1,k-2N_{\mathrm{z}})} & \text{if } i\in S_2^{\mathrm{x}},\ j\in S_1^{\mathrm{y}},\ k\in S_2^{\mathrm{z}}\\ Z^{pq\pm}_{(i-1,j-2N_{\mathrm{y}},k-2N_{\mathrm{z}})} & \text{if } i\in S_1^{\mathrm{x}},\ j\in S_2^{\mathrm{y}},\ k\in S_2^{\mathrm{z}}\\ Z^{pq\pm}_{(i-2N_{\mathrm{x}},j-2N_{\mathrm{y}},k-2N_{\mathrm{z}})} & \text{if } i\in S_2^{\mathrm{x}},\ j\in S_2^{\mathrm{y}},\ k\in S_2^{\mathrm{z}}\end{cases} \tag{45}$$

for $(i,j,k)\in\left\{(0,0,0),\ldots,\left(2N_{\mathrm{x}},2N_{\mathrm{y}},2N_{\mathrm{z}}\right)\right\}$. Here, the sets are given as

$$\begin{aligned}S_1^{\mathrm{x}}&=\{0,\ldots,N_{\mathrm{x}}\},\ S_2^{\mathrm{x}}=\{N_{\mathrm{x}}+1,\ldots,2N_{\mathrm{x}}\}\\ S_1^{\mathrm{y}}&=\{0,\ldots,N_{\mathrm{y}}\},\ S_2^{\mathrm{y}}=\{N_{\mathrm{y}}+1,\ldots,2N_{\mathrm{y}}\}\\ S_1^{\mathrm{z}}&=\{0,\ldots,N_{\mathrm{z}}\},\ S_2^{\mathrm{z}}=\{N_{\mathrm{z}}+1,\ldots,2N_{\mathrm{z}}\}.\end{aligned} \tag{46}$$

The $\widehat{\mathbf{Z}}^{pq\pm}$ arrays are filled by computing $Z^{pq\pm}_{\mathbf{m}-\mathbf{n}}$ terms such that $\mathbf{m}-\mathbf{n}$ values are in the extended set

$$\mathbf{m}-\mathbf{n}\in\left\{(i,j,k)\middle|-N_{\mathrm{x}}\le i\le N_{\mathrm{x}},\ -N_{\mathrm{y}}\le j\le N_{\mathrm{y}},\ -N_{\mathrm{z}}\le k\le N_{\mathrm{z}}\right\}. \tag{47}$$

Note that the actual basis/testing functions on the mesh give rise to a $\mathbf{m}-\mathbf{n}$ values that are limited to the smaller set

$$\mathbf{m}-\mathbf{n} \in \left\{ (i,j,k) \middle| \begin{array}{l} 1-\hat{\mathbf{p}}\bullet\hat{\mathbf{x}} - N_{\mathrm{x}} \le i \le N_{\mathrm{x}} - 1 + \hat{\mathbf{q}}\bullet\hat{\mathbf{x}}, \\ 1-\hat{\mathbf{p}}\bullet\hat{\mathbf{y}} - N_{\mathrm{y}} \le j \le N_{\mathrm{y}} - 1 + \hat{\mathbf{q}}\bullet\hat{\mathbf{y}}, \\ 1-\hat{\mathbf{p}}\bullet\hat{\mathbf{z}} - N_{\mathrm{z}} \le k \le N_{\mathrm{z}} - 1 + \hat{\mathbf{q}}\bullet\hat{\mathbf{z}} \end{array} \right\} \text{ for } p,q \in \{\mathrm{x},\mathrm{y},\mathrm{z}\} \tag{48}$$

which can be verified by using (30)-(32). The $Z_{\mathbf{m}-\mathbf{n}}^{pq\pm}$ corresponding to testing-basis function pairs that are not present in the mesh exist because of the zero-padding scheme in (44) and are either multiplied by zero coefficients in the $\widehat{\boldsymbol{\kappa}}^{q\pm}\bullet\widehat{\mathbf{I}}^{q}$ arrays or the result of the multiplication is discarded after the $\widehat{\mathbf{V}}^{\mathrm{sca},p}$ arrays are computed in (44).

The self-term contribution is still computationally negligible (sparse matrix-vector multiplication) compared to the FFTs. The 36 $\widehat{\mathbf{Z}}^{pq\pm\pm}$ matrices can be pre-FFTed and stored prior to the matrix-vector multiplications in the solve step. At each iteration, 6 FFTs ($\widehat{\boldsymbol{\kappa}}_{\mathbf{n}}^{q+}\bullet\widehat{\mathbf{I}}_{\mathbf{n}}^{q}$ and $\widehat{\boldsymbol{\kappa}}_{\mathbf{n}}^{q-}\bullet\widehat{\mathbf{I}}_{\mathbf{n}}^{q}$ for $q\in\{x,y,z\}$) and 6 IFFTs must be performed to compute $\widehat{\mathbf{V}}^{\mathrm{sca},p}$ for $p\in\{x,y,z\}$. Table 1 compares the computational costs of the proposed GMRES-FFT method to the common CG-FFT method: (i) The proposed GMRES-FFT requires nearly twice as much memory because of the additional separation of matrices arising from the contrast-weighted testing functions. (ii) The matrix-fill time (including the time to pre-FFT the block-Toeplitz matrices) of the proposed method will be essentially the same as that of the common CG-FFT method because both times are dominated by the computation of the integrals and because both methods construct about the same number of equations. (iii) The proposed GMRES-FFT will require approximately 33% more operations to multiply matrices at each iteration because it computes more inverse FFTs.

Table 1 Computational costs of common CG-FFT vs. proposed GMRES-FFT

Method	Large Arrays Stored	Pre-FFTs	FFTs / Iteration	IFFTs / Iteration
Common CG-FFT	22 $18\ (\hat{\mathbf{Z}}^{pq\pm}) + 1\ (\hat{\mathbf{I}}^{q}) + 3\ (\hat{\mathbf{V}}^{\mathrm{sca},p})$	18	6	3
Proposed GMRES-FFT	43 $36\ (\hat{\mathbf{Z}}^{pq\pm\pm}) + 1\ (\hat{\mathbf{I}}^{q}) + 6\ (\hat{\mathbf{V}}^{\mathrm{sca},p\pm})$	36	6	6

In summary, by filling and storing only the unique entries of the block-Toeplitz matrix components of $\mathbf{Z}$ and by using 3-D FFTs to accelerate the matrix-vector multiplication during the iterative solution, the GMRES-FFT method reduces the MOM computational costs to $O\left(N_{\text{GMRES-FFT}}\right)$ matrix fill operations, $O\left(N_{\text{GMRES-FFT}}\right)$ memory space, and $O\left(N_{\text{GMRES-FFT}} \log N_{\text{GMRES-FFT}}\right)$ operations per iteration. The GMRES-FFT method yields solutions that are identical (within machine precision) to the MOM solution as it makes no approximations while compressing the $\mathbf{Z}$ matrix; however, the method constrains the geometry discretization to voxels and is thus inapplicable for irregular (tetrahedral) meshes [34].

2.3.3 Adaptive Integral Method (AIM)

While AIM also utilizes the translational invariance of the Green's function to reduce the MOM computational costs, it does not require the geometry to be regularly meshed. Instead, in the AIM approach, an auxiliary regular grid of point sources and observers is used to approximate the impedance matrix entries: (i) The primary mesh of V is enclosed by an auxiliary grid composed of $N_{\mathrm{C}} = N_{\mathrm{cx}} \times N_{\mathrm{cy}} \times N_{\mathrm{cz}}$ grid points. (ii) The impedance matrix $\mathbf{Z}$ is then split into two terms [34], [57]:

$$\mathbf{Z}\mathbf{I}^{*} \approx \mathbf{Z}^{\mathrm{FFT}}\mathbf{I}^{*} + \mathbf{Z}^{\mathrm{corr}}\mathbf{I}^{*}, \tag{49}$$

where

$$\mathbf{Z}_{N\times N}^{\mathrm{FFT}} = \sum_{i\in\{x,y,z,\nabla\}} \mathbf{\Lambda}^{i\dagger}\mathbf{G}\mathbf{\Lambda}^{i}. \tag{50}$$

The sparse anterpolation matrices $\mathbf{\Lambda}^{i}$ map currents from the primary mesh to the auxiliary grid, the 3-level block Toeplitz matrix $\mathbf{G}$ propagates potentials from source points on the auxiliary grid to observer points on the same grid, and the transpose matrices $\mathbf{\Lambda}^{i\dagger}$ interpolate the fields from the auxiliary grid back to the primary mesh. In (10), $\mathbf{Z}^{\mathrm{corr}}$ is a sparse correction matrix with N_{corr} non-zero entries defined as:

$$\mathbf{Z}^{\mathrm{corr}}[m,n] = \begin{cases} \mathbf{Z}[m,n] - \mathbf{Z}^{\mathrm{FFT}}[m,n], & \text{if } \mathbf{f}_m \text{ near } \mathbf{f}_n \\ 0, & \text{otherwise.} \end{cases} \tag{51}$$

The functions $\mathbf{f}_m$ and $\mathbf{f}_n$ are considered near if the minimum distance among the points that they map to is less than a pre-specified distance along each Cartesian direction [34], [58]; i.e., only if all three of the following conditions are met:

$$\min_{u\in C_m, u'\in C_n} |x_u - x_{u'}| < \gamma_{\mathrm{x}}\Delta c_{\mathrm{x}}, \quad \min_{u\in C_m, u'\in C_n} |y_u - y_{u'}| < \gamma_{\mathrm{y}}\Delta c_{y}, \quad \min_{u\in C_m, u'\in C_n} |z_u - z_{u'}| < \gamma_{\mathrm{z}}\Delta c_{\mathrm{z}}. \tag{52}$$

Here, $\Delta c_{\mathrm{x,y,z}}$ denote the auxiliary grid spacing along different Cartesian directions, $C_{m,n}$ denote the set of auxiliary grid points associated with $\mathbf{f}_m$ and $\mathbf{f}_n$, and $\gamma_{\mathrm{x,y,z}}$ are independent parameters that define the size of the near-zone correction region.

The anterpolation matrix, $\mathbf{\Lambda}^{i}$, is a sparse matrix with N_{map} non-zero entries that are found by matching multipole moments of potential functions at M grid points to the functions, $\kappa_n\mathbf{f}_n$ [34]. The propagation matrix $\mathbf{G}$ is an $N_{\mathrm{C}}\times N_{\mathrm{C}}$ matrix that has N_{C} unique entries arranged in a 3-level block-Toeplitz structure; thus it requires $O(N_{\mathrm{C}})$ operations to fill $\mathbf{G}$, $O(N_{\mathrm{C}})$ bytes to store it, and $O(N_{\mathrm{C}}\log N_{\mathrm{C}})$ operations to perform an accelerated matrix-vector multiplication with 3-D FFTs just as in (44) [35]. For the BioEM simulations considered in this thesis, $\Delta c_{\mathrm{x,y,z}}$, $\gamma_{\mathrm{x,y,z}}$, and M can be chosen such that $N_{\mathrm{C}} \sim N_{\mathrm{MOM}}$, $N_{\mathrm{corr}} \sim N_{\mathrm{MOM}}$, and $N_{\mathrm{map}} \sim N_{\mathrm{MOM}}$, resulting in $O(N_{\mathrm{MOM}})$ operations to fill all of the matrices, $O(N_{\mathrm{MOM}})$ bytes to store them, and $O(N_{\mathrm{MOM}}\log N_{\mathrm{MOM}})$ operations to perform

the multiplication at each iteration [59]. These parameters also offer a tradeoff between the accuracy and the computational costs of the method.

2.4 FINITE-DIFFERENCE TIME-DOMAIN (FDTD)

The FDTD solution of (1) is performed in five steps: (i) A regular voxel mesh of V^{num} (with spacing $\{\Delta x, \Delta y, \Delta z\}$) is used to sample the scattered fields in space and time according to the Yee scheme: Electric field components are sampled on the cell edges at times $\Delta t, 2\Delta t, ..., N_{\text{T}}\Delta t$ and magnetic field components are sampled at the center of the faces at times $0.5\Delta t, 1.5\Delta t, ..., (N_{\text{T}} - 0.5)\Delta t$ [60]. The FDTD time-step size must be chosen to satisfy the Courant-Freidrisch-Levy stability condition $\Delta t \leq 1/c_0\sqrt{\Delta x^{-2} + \Delta y^{-2} + \Delta z^{-2}}$ [17], [61]. (ii) The material properties $\{\varepsilon, \sigma\}$ of the scattering volume are assumed frequency independent. Because constant parameters can represent tissue properties accurately only over narrow bands of frequencies [62], this simplification sacrifices an inherent advantage of time-domain methods: their ability to find results over a broad frequency band with a single transient simulation. That is, just like frequency-domain methods, the solution must be re-calculated using different constant material parameters when different frequencies are of interest. Nevertheless, using frequency-independent material properties is the most efficient approach when time harmonic solutions are of interest because temporal convolutions in (1) become multiplications. (iii) The partial derivatives in (1) are approximated using a second-order accurate central differencing scheme; this yields the FDTD update equations [38], e.g., for the $\hat{\mathbf{x}}$ components of the electric and magnetic fields:

$$H_x^{\text{sca}}\Big|_{i,j+\frac{1}{2},k+\frac{1}{2}}^{l+\frac{1}{2}} \approx H_x^{\text{sca}}\Big|_{i,j+\frac{1}{2},k+\frac{1}{2}}^{l-\frac{1}{2}} + \frac{\Delta t}{\mu_0}\left(\frac{E_y^{\text{sca}}\Big|_{i,j+\frac{1}{2},k+1}^{l} - E_y^{\text{sca}}\Big|_{i,j+\frac{1}{2},k}^{l}}{\Delta z} - \frac{E_z^{\text{sca}}\Big|_{i,j+1,k+\frac{1}{2}}^{l} - E_z^{\text{sca}}\Big|_{i,j,k+\frac{1}{2}}^{l}}{\Delta y} \right)$$

$$E_x^{\text{sca}}\Big|_{i+\frac{1}{2},j,k}^{l+1} \approx \frac{\varepsilon_{i+\frac{1}{2},j,k} - \frac{\Delta t}{2}\sigma_{i+\frac{1}{2},j,k}}{\varepsilon_{i+\frac{1}{2},j,k} + \frac{\Delta t}{2}\sigma_{i+\frac{1}{2},j,k}} E_x^{\text{sca}}\Big|_{i+\frac{1}{2},j,k}^{l} +$$

$$\frac{\Delta t}{\varepsilon_{i+\frac{1}{2},j,k} + \frac{\Delta t}{2}\sigma_{i+\frac{1}{2},j,k}} \left(\begin{array}{l} \dfrac{H_z^{\text{sca}}\Big|_{i+\frac{1}{2},j+\frac{1}{2},k}^{l+\frac{1}{2}} - H_z^{\text{sca}}\Big|_{i+\frac{1}{2},j-\frac{1}{2},k}^{l+\frac{1}{2}}}{\Delta y} - \\ \dfrac{H_y^{\text{sca}}\Big|_{i+\frac{1}{2},j,k+\frac{1}{2}}^{l+\frac{1}{2}} - H_y^{\text{sca}}\Big|_{i+\frac{1}{2},j,k-\frac{1}{2}}^{l+\frac{1}{2}}}{\Delta z} - \\ \sigma_{i+\frac{1}{2},j,k}\, E_x^{\text{inc}}\Big|_{i+\frac{1}{2},j,k}^{l+\frac{1}{2}} + \left(\varepsilon_0 - \varepsilon_{i+\frac{1}{2},j,k}\right)\partial_t\, E_x^{\text{inc}}\Big|_{i+\frac{1}{2},j,k}^{l+\frac{1}{2}} \end{array} \right), \tag{53}$$

where the subscript indicates the spatial position and the superscript the time instant, e.g. $E_x^{\text{sca}}\Big|_{i+\frac{1}{2},j,k}^{l+1} = E_x^{\text{sca}}\left(\left(i+\tfrac{1}{2}\right)\Delta x, j\Delta y, k\Delta z, \left(l+1\right)\Delta t\right)$. The electric field update equations require $\{\varepsilon, \sigma\}$ values at the location of the electric field samples, i.e., on the voxel edges. As is common, effective material properties that are equal to the average of the material properties of the four cells that share the edge are used in this case [63], [64]. (iv) The mesh is truncated by introducing an absorbing layer outside the scattering volume to minimize erroneous reflections from the grid's artificial truncation [17], [31]. The absorbing layer is comprised of a PML that is backed by a perfect electrically conducting wall. The split-field PML formulation used in this thesis is constructed by splitting the scattered field into two non-physical fields and artificially introducing conductivities for each component such that theoretically there are no reflections at the PML interface [17], [31]. In the actual implementation, however, there are some reflections at the interface due to finite precision arithmetic, numerical errors, and the layer's finite thickness. The PML is characterized by

the layer thickness, the conductivity profile over the region, and its distance from the scattering volume. (v) The electric and magnetic field samples are found by a leap-frog time-marching scheme [17], [60]. The FDTD implementation used in this thesis is described in greater detail in [38].

Let N_{FDTD} represent the total number of cells in the FDTD mesh of volume V^{num}, which includes an extended region around V, and the PML region; clearly, $N_{\text{FDTD}} > N_{\text{vox}}$. Then, $O\left(N_{\text{FDTD}}\right)$ operations are required to precompute the averaged material properties required at each sample point in (53), $O\left(N_{\text{FDTD}}\right)$ bytes are required to store the material properties and field values at each sample point, and $O\left(N_{\text{FDTD}}\right)$ operations must be performed at each time step. Since the fields are sampled using a regular mesh, FDTD also suffers from staircasing errors. Several approaches have been proposed to reduce the staircasing error for FDTD, e.g., subgridding [65] and conformal FDTD [66], but come with additional computational costs, stability limitations, and implementation complexity.

Chapter 3: Comparison Methodology

This Chapter presents the benchmark scattering problems and the performance criteria that are used to systematically compare the different numerical methods in Chapter 4.

3.1 BENCHMARK PROBLEMS

The numerical methods of interest are quite general and can be used to perform a large variety of BioEM simulations in the UHF band. To be able to draw useful and broad conclusions about the performance of these methods, a BioEM benchmark is introduced. The benchmark is intended to provide information about the performance of different BioEM simulation methods when computing the power absorbed by a human model illuminated with an impressed time-harmonic source. The human and source models in the benchmark are as follows.

3.1.1 Pixel- and Surface-based Models

The BioEM benchmark consists of three inhomogeneous models: a multilayered spherical head phantom, an anatomical male, and an anatomical female model. The head phantom is a sphere of 108-mm radius that is composed of four layers: 4 mm skin (dry), 4 mm fat, 8 mm bone average (mean of bone cortical and bone marrow), and 92 mm brain average (mean of grey matter and white matter) [40]. The human models are the AustinMan v2.2 and AustinWoman v2.1 [16], which were developed from the anatomical cross-sectional images in the Visible Human Project [67]. The AustinMan model fits in a rectangular cuboid of size $325\times569\times1877$ mm^3 and is comprised of 63 different tissues, and the AustinWoman model fits in a rectangular cuboid of size $292\times536\times1730$ mm^3 and is comprised of 56 different tissues. The material properties of the tissues in the models are obtained from [62], [68] for the frequencies of interest; see Appendix A.

Both a pixel-based and a surface-based model are used for the spherical head phantom, while only pixel-based models are used for the AustinMan and AustinWoman models. The pixel-based spherical and anatomical models were created in a similar manner starting from a set of fine-resolution ($\frac{1}{3}\times\frac{1}{3}\times 1\ \text{mm}^3$) pixelated cross-sectional images, segmenting the pixels using the original resolution of the images, and coarsening the pixels to various resolutions [16]. The pixels were then extruded to create voxel meshes of the models. The tetrahedral meshes for the head phantom were generated from the analytical surface definitions using a CAD program [69]. The meshes are visualized in Figure 6 (head phantom), Figure 7 (AustinMan), and Figure 8 (AustinWoman) and the number of cells in each mesh is listed in Table 2. For additional visualizations and material properties, see [70]. All the meshes used in this thesis are available for download in [70], [71].

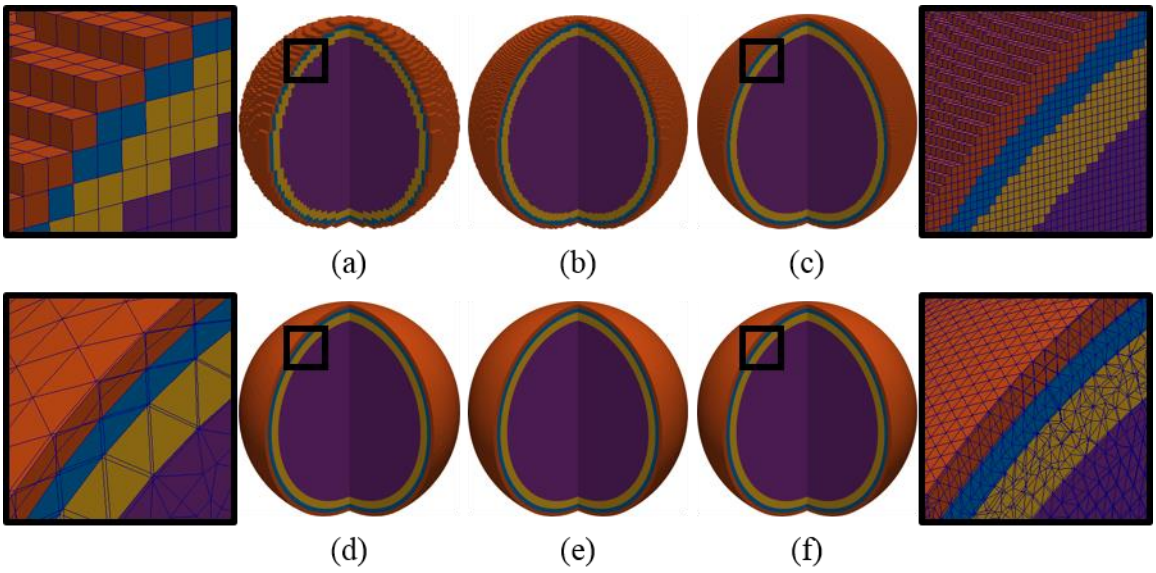

Figure 6: The multilayered spherical head phantom with one quadrant removed to show the inner layers. Voxel – (a) 4×4×4 mm^3 with a zoomed in portion to its left, (b) 2×2×2 mm^3, (c) 1×1×1 mm^3 with a zoomed in portion to its right, Tetrahedral – (d) 60.7 mm^3 with a zoomed in portion to its left, (e) 8.32 mm^3, and (f) 0.91 mm^3 with a zoomed in portion to its right. Staircasing causes a poor representation of the original boundaries in the voxel mesh.

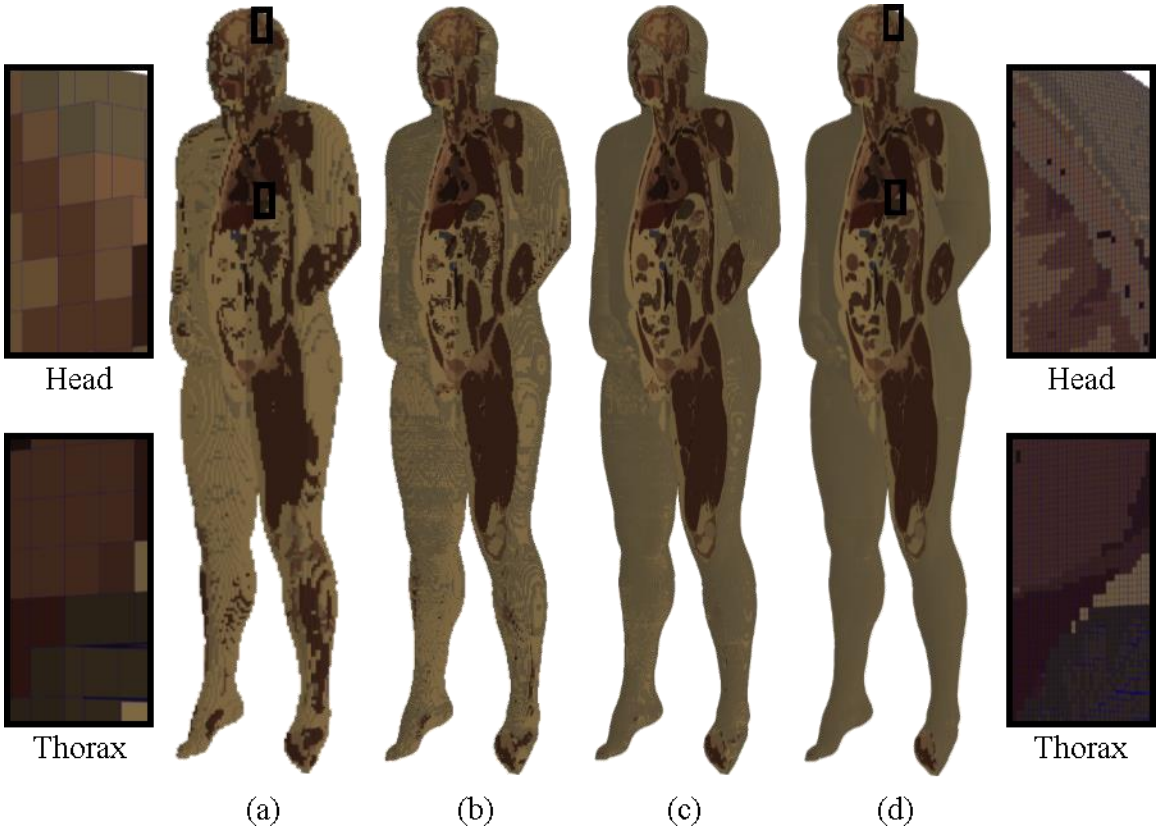

Figure 7: AustinMan v2.2 visualizations with one quadrant removed to show the internal tissues for the (a) 8×8×8 mm^3, (b) 4×4×4 mm^3, (c) 2×2×2 mm^3, and (d) 1×1×1 mm^3 resolutions. Portions of the head and thorax are zoomed in for the 8×8×8 mm^3 and 1×1×1 mm^3 resolutions on the left and right, respectively.

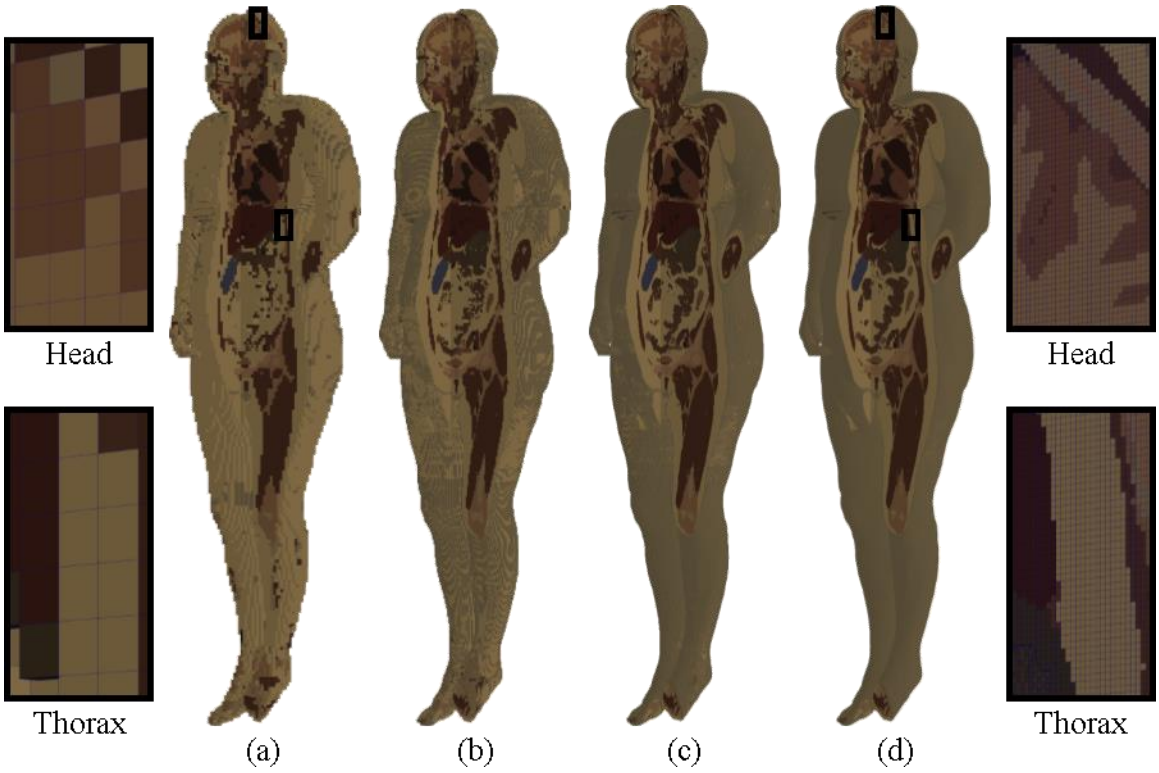

Figure 8: AustinWoman v2.1 visualizations with one quadrant removed to show the internal tissue details for the (a) 8×8×8 mm^3, (b) 4×4×4 mm^3, (c) 2×2×2 mm^3, and (d) 1×1×1 mm^3 resolutions. Portions of the head and thorax are zoomed in for the 8×8×8 mm^3 and 1×1×1 mm^3 resolutions on the left and right, respectively.

Table 2 Mesh properties for the benchmark models

Model	Cell Type	Avg. Cell Volume	Number of Cells	Avg. Edge Length
Head Sphere	Tetra	60.7 mm^3	86 663	8.53 mm
Head Sphere	Tetra	8.32 mm^3	633 632	4.38 mm
Head Sphere	Tetra	0.91 mm^3	5 803 958	2.09 mm
Head Sphere	Voxel	4×4×4 mm^3	82 504	4 mm
Head Sphere	Voxel	2×2×2 mm^3	658 976	2 mm
Head Sphere	Voxel	1×1×1 mm^3	5 276 488	1 mm
AustinMan v2.2	Voxel	8×8×8 mm^3	195 556	8 mm
AustinMan v2.2	Voxel	4×4×4 mm^3	1 588 389	4 mm
AustinMan v2.2	Voxel	2×2×2 mm^3	12 743 667	2 mm
AustinMan v2.2	Voxel	1×1×1 mm^3	102 009 137	1 mm
AustinWoman v2.1	Voxel	8×8×8 mm^3	157 082	8 mm
AustinWoman v2.1	Voxel	4×4×4 mm^3	1 276 976	4 mm
AustinWoman v2.1	Voxel	2×2×2 mm^3	10 241 026	2 mm
AustinWoman v2.1	Voxel	1×1×1 mm^3	81 949 413	1 mm

3.1.2 Excitations

A plane wave and an impressed Hertzian dipole are used to excite the models. The plane wave excitation, which represents illumination from far away sources such as cell-phone towers, is given as

$$\mathbf{E}^{\text{inc}}(\mathbf{r},t) = \hat{\mathbf{p}}_{\text{PW}} E_0^{\text{inc}} f\left(t - t_{\text{d}} - \hat{\mathbf{k}} \cdot \mathbf{r} / c_0, \omega\right), \tag{54}$$

where $\hat{\mathbf{p}}_{\text{PW}}$ is the polarization vector, E_0^{inc} is the magnitude, f is the waveform function, $\hat{\mathbf{k}}$ is the propagation direction, and t_{d} is the time delay. The dipole excitation, which represents illumination from nearby sources such as cell-phone antennas, is given as

$$\begin{aligned}\mathbf{E}^{\text{inc}}(\mathbf{r},t) = \frac{IL}{2\pi\varepsilon_0}\Bigg[& \hat{\mathbf{R}}\left(\hat{\mathbf{R}}\cdot\hat{\mathbf{p}}_{\text{HD}}\right)\left(\frac{1}{R^3} + \frac{1}{R^2 c_0}\partial_t\right) + \\ & \frac{\hat{\mathbf{R}}\times\left(\hat{\mathbf{R}}\times\hat{\mathbf{p}}_{\text{HD}}\right)}{2}\left(\frac{1}{R^3} + \frac{1}{R^2 c_0}\partial_t + \frac{1}{R c_0^2}\partial_t^2\right)\Bigg]\int_{-\infty}^{t-\frac{R}{c_0}} f\left(\tau - t_{\text{d}}, \omega\right) d\tau,\end{aligned} \tag{55}$$

for a $\hat{\mathbf{p}}_{\mathrm{HD}}$-oriented Hertzian dipole centered at $\mathbf{r}'$ with current I and length L; here, $\hat{\mathbf{R}} = \left(\mathbf{r} - \mathbf{r}'\right)/R$. For time-domain simulations, the sinusoidally modulated ramp defined in [38], which is the turn-on ramp and steady-state portion of the multiple cycle *m*-*n*-*m* pulse in [72], is used as the waveform function, i.e.,

$$f\left(t,\omega\right) = \begin{cases} 0, & t < 0 \\ g\left(t\right)\sin\left(\omega t\right), & 0 \le t \le 2\pi\zeta/\omega \\ \sin\left(\omega t\right), & t > 2\pi\zeta/\omega, \end{cases} \tag{56}$$

where ζ is the number of periods over which the waveform function ramps up before becoming a sinusoid, g is the ramp function in [72], $g\left(t\right) = 10\tau^3 - 15\tau^4 + 6\tau^5$, and $\tau = t/\left(2\pi\zeta/\omega\right)$.

The frequency-domain representation of the incident fields corresponding to the above expressions are

$$\tilde{\mathbf{E}}^{\mathrm{inc}}\left(\mathbf{r},\omega\right) = \hat{\mathbf{p}}_{\mathrm{PW}} E_0^{\mathrm{inc}} e^{-j\omega t_{\mathrm{d}}} e^{-j\left(\hat{\mathbf{k}}\cdot\mathbf{r}\right)\omega/c_0} \tag{57}$$

for the plane wave and

$$\begin{aligned} \tilde{\mathbf{E}}^{\mathrm{inc}}\left(\mathbf{r},\omega\right) = \frac{IL}{2\pi}\sqrt{\frac{\mu_0}{\varepsilon_0}}\, e^{-j\omega t_{\mathrm{d}}} e^{-j\left(\hat{\mathbf{k}}\cdot\mathbf{r}\right)\omega/c_0} \Bigg[\hat{\mathbf{R}}\left(\hat{\mathbf{R}}\cdot\hat{\mathbf{p}}_{\mathrm{HD}}\right)\left(\frac{c_0}{j\omega R^3} + \frac{1}{R^2}\right) \\ + \hat{\mathbf{R}}\times\left(\hat{\mathbf{R}}\times\hat{\mathbf{p}}_{\mathrm{HD}}\right)\frac{j\omega}{2c_0}\left(\frac{c_0^2}{\left(j\omega\right)^2 R^3} + \frac{c_0}{j\omega R^2} + \frac{1}{R}\right)\Bigg] \end{aligned} \tag{58}$$

for the dipole.

3.1.3 Frequencies

Three frequencies in the UHF band are considered: 402 MHz, 900 MHz, and 2.45 GHz, which are in the MICS, GSM-900, and ISM bands used in medical implants, cell phones, and Wi-Fi and microwave ovens, respectively.

3.2 PERFORMANCE CRITERIA

The criteria used in this thesis to quantify the accuracy, computational costs, and the accuracy-cost tradeoff of the simulations are detailed next.

3.2.1 Error Measures

In Chapter 4, five different measures are used to quantify the errors. These error measures are defined using the pointwise time-averaged absorbed power density

$$\begin{aligned}\bar{P}(\mathbf{r},\omega) &= \frac{\omega}{2\pi}\int_{2\pi/\omega}\sigma(\mathbf{r},\omega)\mathbf{E}(\mathbf{r},t)\bullet\mathbf{E}(\mathbf{r},t)\,dt \\ &= \frac{1}{2}\sigma(\mathbf{r},\omega)\tilde{\mathbf{E}}(\mathbf{r},\omega)\bullet\tilde{\mathbf{E}}^{*}(\mathbf{r},\omega)\ \ (\mathrm{W/m^3})\end{aligned} \tag{59}$$

and integrating it over different volumes; e.g.,

$$\begin{aligned}\bar{P}_{\mathrm{cell}_k}(\omega) &= \iiint_{V_k}\bar{P}(\mathbf{r},\omega)\,dV\ (\mathrm{W}) \\ \bar{P}_{\mathrm{tissue}_T}(\omega) &= \iiint_{V_T}\bar{P}(\mathbf{r},\omega)\,dV \approx \sum_{k\ \mathrm{s.t.}\ V_k\subset V_T}\bar{P}_{\mathrm{cell}_k}\ (\mathrm{W}) \\ \bar{P}_{\mathrm{tot}}(\omega) &= \iiint_{V}\bar{P}(\mathbf{r},\omega)\,dV \approx \sum_{\forall k}\bar{P}_{\mathrm{cell}_k}\ (\mathrm{W})\end{aligned} \tag{60}$$

yields the power absorbed in cell k, in tissue T, and the entire scattering volume, respectively. It is important to observe that even if $\bar{P}_{\mathrm{cell}_k}$ could be computed exactly in each cell, the last two integrals in (60) would still be approximate because the volumes V_T and V are approximated in terms of small cells. In the above equations, the superscript * denotes the complex conjugate and the single bar above a variable indicates that it is a time-averaged quantity.

To illustrate the pros and cons of the different error measures defined below, a simple example is used (Figure 9). In this example, the scattering volume is composed of four 1 mm^3 cells illuminated by an unspecified source such that, in the reference solution, the cells on the left absorb the time-averaged power of 1 nW and the cells on the right

absorb 0.1 nW; i.e., the cell-averaged time-averaged absorbed power density ($\overline{\overline{P}}$) in these cells are 1 W/m^3 and 0.1 W/m^3. Three different numerical results are contrasted in Figure 9: in scenario 1, arbitrary numbers are assigned to the cells (the numbers are normalized to match $\overline{P}_{\text{tot}}$ in the reference); in scenarios 2 and 3, $\overline{\overline{P}}$ is identical to the reference in two of the cells, 20% higher than the reference in a third cell, and 10% lower than the reference in the last cell.

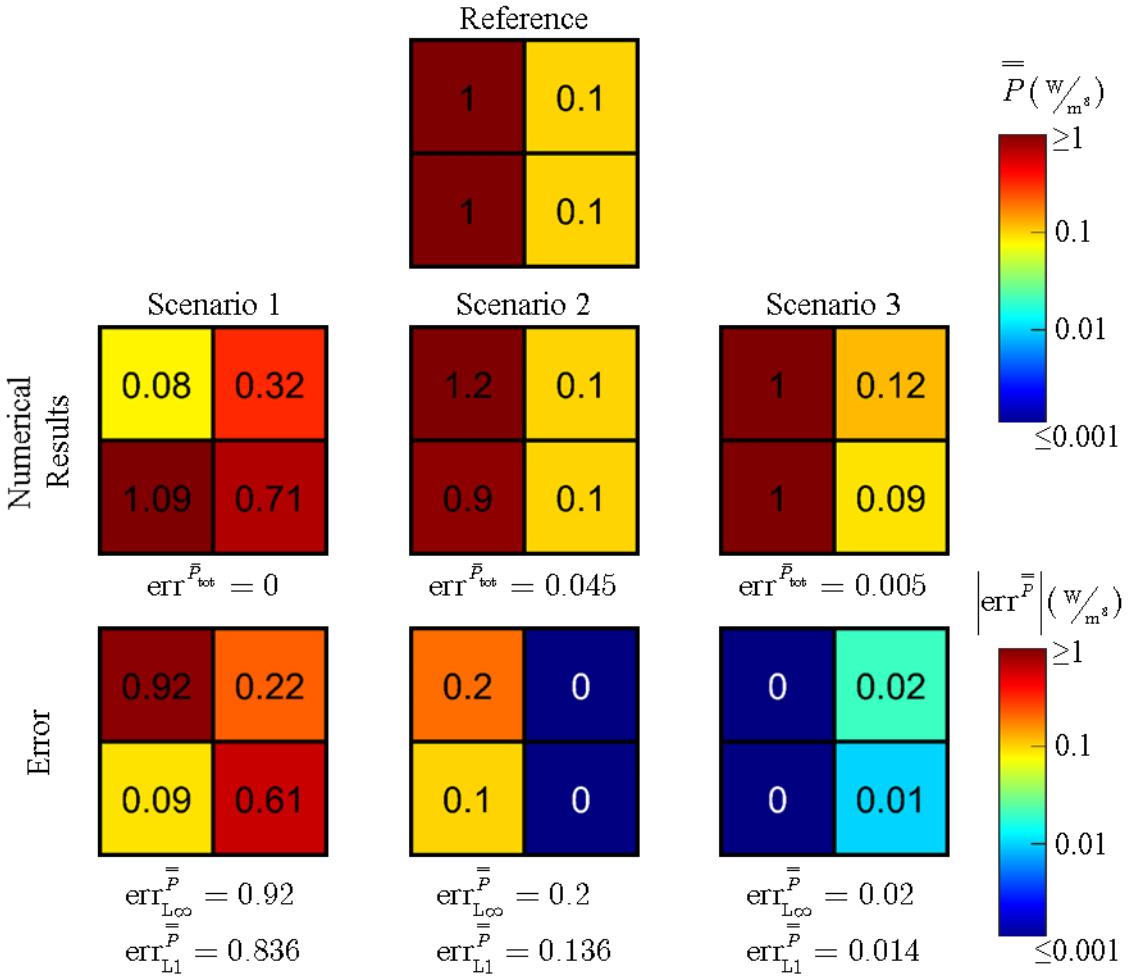

Figure 9: A simple example with four cells that demonstrates the properties of the error measures. Top: Reference solution. Each cell is colored according to the value of $\bar{\bar{P}}$ (W/m^3), which is shown in the middle of the cell. Middle: Three different approximate solutions. The cells are colored according to the value of $\bar{\bar{P}}$ shown in the middle of the cell. The relative error of the total absorbed power $\mathrm{err}^{\bar{P}_{\mathrm{tot}}}$ is also shown for each scenario. Bottom: Cellwise absolute error. Each cell is colored according to the value of $|\mathrm{err}^{\bar{\bar{P}}}|$ shown in the middle of the cell. Also shown are the L∞- and L1-norms of $\mathrm{err}^{\bar{\bar{P}}}$ for each scenario. All colors are set using the logarithmic color bar on the right. All error measures indicate a larger error in Scenario 2 than in Scenario 3 even though in both cases a +20% and a −10% relative error is made in two of cells; this is because the measures are more sensitive to the errors in hot spots.

Error Measure 1: Relative Error of the Total Absorbed Power

The first measure used in this thesis to quantify accuracy is the *relative error of the total absorbed power* defined as

$$\mathrm{err}^{\bar{P}_{\mathrm{tot}}}(\omega) = \frac{\left|\bar{P}_{\mathrm{tot}}^{\mathrm{ref}}(\omega) - \bar{P}_{\mathrm{tot}}(\omega)\right|}{\bar{P}_{\mathrm{tot}}^{\mathrm{ref}}(\omega)}. \tag{61}$$

The reference $\bar{P}_{\mathrm{tot}}^{\mathrm{ref}}$ can be found from analytical, experimental, or more accurate numerical results; e.g., for the multilayered spherical head phantom, the analytical solution is available and is used as the reference in Chapter 4 [73]. On the one hand, $\mathrm{err}^{\bar{P}_{\mathrm{tot}}}$ is straightforward to calculate, is a single number at each frequency, and directly quantifies the accuracy of the total power absorbed by the model $\bar{P}_{\mathrm{tot}}$—an important quantity for assessing compliance with safety standards such as limitations on the whole-body specific absorption rate (SAR) [9], [74]. On the other hand, it is a rather insensitive measure that is often inadequate when comparing numerical methods because two simulations with very different results (field distributions) could have the same $\mathrm{err}^{\bar{P}_{\mathrm{tot}}}$. This is demonstrated in the scenario 1 in Figure 9, where $\mathrm{err}^{\bar{P}_{\mathrm{tot}}} = 0$ despite the fact that the absorbed power density is very different than the reference solution.

This insensitivity is a natural limitation of whole-volume error norms like $\mathrm{err}^{\bar{P}_{\mathrm{tot}}}$ that first integrate a function of interest and then compare the result to a reference. A possible alternative is to use pointwise error norms that first compare the result to a reference at each point and then integrate the difference. For example, consider the pointwise error in the absorbed power density

$$\mathrm{err}^{\bar{P}}(\mathbf{r},\omega) = \bar{P}^{\mathrm{ref}}(\mathbf{r},\omega) - \bar{P}(\mathbf{r},\omega) \ (\mathrm{W/m^3}) \tag{62}$$

and its L∞- and L1-norms:

$$\mathrm{err}_{\mathrm{L}\infty}^{\bar{P}}(\omega)=\frac{\max\limits_{\mathbf{r}\in V}\left|\mathrm{err}^{\bar{P}}(\mathbf{r},\omega)\right|}{\max\limits_{\mathbf{r}\in V}\bar{P}^{\mathrm{ref}}(\mathbf{r},\omega)}=\frac{\max\limits_{\mathbf{r}\in V}\left|\bar{P}^{\mathrm{ref}}(\mathbf{r},\omega)-\bar{P}(\mathbf{r},\omega)\right|}{\max\limits_{\mathbf{r}\in V}\bar{P}^{\mathrm{ref}}(\mathbf{r},\omega)}\approx\frac{\max\limits_{k}\max\limits_{\mathbf{r}\in V_k}\left|\mathrm{err}^{\bar{P}}(\mathbf{r},\omega)\right|}{\max\limits_{\mathbf{r}\in V}\bar{P}^{\mathrm{ref}}(\mathbf{r},\omega)} \quad (63)$$

$$\mathrm{err}_{\mathrm{L}1}^{\bar{P}}(\omega)=\frac{\iiint_V\left|\mathrm{err}^{\bar{P}}(\mathbf{r},\omega)\right|dV}{\iiint_V\bar{P}^{\mathrm{ref}}(\mathbf{r},\omega)\,dV}=\frac{\iiint_V\left|\bar{P}^{\mathrm{ref}}(\mathbf{r},\omega)-\bar{P}(\mathbf{r},\omega)\right|dV}{\iiint_V\bar{P}^{\mathrm{ref}}(\mathbf{r},\omega)\,dV}\approx\frac{\sum\limits_{\forall k}\iiint_{V_k}\left|\mathrm{err}^{\bar{P}}(\mathbf{r},\omega)\right|dV}{\sum\limits_{\forall k}\iiint_{V_k}\bar{P}^{\mathrm{ref}}(\mathbf{r},\omega)\,dV}. \quad (64)$$

Unfortunately, there are difficulties when computing such pointwise error norms (see note 2 below); instead, cell-averaged quantities (also known as "cellwise" rather than pointwise quantities) are used in this thesis as an alternative to pointwise error norms.

Error Measure 2: Absolute Error of the Cell-Averaged Absorbed Power Density—Visualization

The second measure used in this thesis to quantify accuracy is the *absolute error of* $\bar{\bar{P}}$*, the cell-averaged time-averaged absorbed power density,*

$$\bar{\bar{P}}(\mathbf{r},\omega)=\frac{\bar{P}_{\mathrm{cell}_k}(\omega)}{V_k}=\frac{1}{V_k}\iiint_{V_k}\bar{P}(\mathbf{r},\omega)\,dV\ (\mathrm{W/m^3})\quad \text{for } \mathbf{r}\in\mathrm{cell}_k \quad (65)$$

$$\begin{aligned}\mathrm{err}^{\bar{\bar{P}}}(\mathbf{r},\omega)&=\bar{\bar{P}}^{\mathrm{ref}}(\mathbf{r},\omega)-\bar{\bar{P}}(\mathbf{r},\omega)\ (\mathrm{W/m^3})\quad \forall\mathbf{r}\in V\\&=\frac{\iiint_{V_k}\bar{P}^{\mathrm{ref}}(\mathbf{r},\omega)-\bar{P}(\mathbf{r},\omega)\,dV}{V_k}=\frac{\iiint_{V_k}\mathrm{err}^{\bar{P}}(\mathbf{r},\omega)\,dV}{V_k}\ (\mathrm{W/m^3})\ \text{for } \mathbf{r}\in\mathrm{cell}_k.\end{aligned} \quad (66)$$

Because it is a function of position, this error measure contains more information than $\mathrm{err}^{\bar{P}_{\mathrm{tot}}}$. The information is best represented using color images that visualize $\bar{\bar{P}}$ and $\left|\mathrm{err}^{\bar{\bar{P}}}\right|$ using the same color scale (e.g., middle and bottom rows in Figure 9). Because the same quantity (power density) is visualized, the colors in images resulting from simulations that use different sized cells can be compared meaningfully and intuitively.

Error Measures 3-4: L∞- and L1-norm of the Error in the Cell-Averaged Absorbed Power Density

The third and fourth error measures are the *L∞-norm and L1-norm of* $\mathrm{err}^{\bar{\bar{P}}}$:

$$\mathrm{err}_{\mathrm{L}\infty}^{\bar{\bar{P}}}(\omega)=\frac{\max_{\mathbf{r}\in V}\left|\mathrm{err}^{\bar{\bar{P}}}(\mathbf{r},\omega)\right|}{\max_{\mathbf{r}\in V}\bar{\bar{P}}^{\mathrm{ref}}(\mathbf{r},\omega)}=\frac{\max_{\mathbf{r}\in V}\left|\bar{\bar{P}}^{\mathrm{ref}}(\mathbf{r},\omega)-\bar{\bar{P}}(\mathbf{r},\omega)\right|}{\max_{\mathbf{r}\in V}\bar{\bar{P}}^{\mathrm{ref}}(\mathbf{r},\omega)}=\frac{\max_{k}\left|\frac{1}{V_k}\iiint_{V_k}\mathrm{err}^{\bar{P}}(\mathbf{r},\omega)\,dV\right|}{\max_{k}\frac{1}{V_k}\iiint_{V_k}\bar{P}^{\mathrm{ref}}(\mathbf{r},\omega)\,dV} \tag{67}$$

$$=\frac{\max_{k}\left|\bar{P}_{\mathrm{cell}_k}^{\mathrm{ref}}(\omega)-\bar{P}_{\mathrm{cell}_k}(\omega)\right|/V_k}{\max_{k}\bar{P}_{\mathrm{cell}_k}^{\mathrm{ref}}(\omega)/V_k}$$

$$\mathrm{err}_{\mathrm{L1}}^{\bar{\bar{P}}}(\omega)=\frac{\iiint_{V}\left|\mathrm{err}^{\bar{\bar{P}}}(\mathbf{r},\omega)\right|dV}{\iiint_{V}\bar{\bar{P}}^{\mathrm{ref}}(\mathbf{r},\omega)\,dV}=\frac{\iiint_{V}\left|\bar{\bar{P}}^{\mathrm{ref}}(\mathbf{r},\omega)-\bar{\bar{P}}(\mathbf{r},\omega)\right|dV}{\iiint_{V}\bar{\bar{P}}^{\mathrm{ref}}(\mathbf{r},\omega)\,dV}=\frac{\sum_{\forall k}\left|\iiint_{V_k}\mathrm{err}^{\bar{P}}(\mathbf{r},\omega)\,dV\right|}{\sum_{\forall k}\iiint_{V_k}\bar{P}^{\mathrm{ref}}(\mathbf{r},\omega)\,dV} \tag{68}$$

$$=\frac{\sum_{\forall k}\left|\bar{P}_{\mathrm{cell}_k}^{\mathrm{ref}}(\omega)-\bar{P}_{\mathrm{cell}_k}(\omega)\right|}{\sum_{\forall k}\bar{P}_{\mathrm{cell}_k}^{\mathrm{ref}}(\omega)}.$$

These error norms are sensitive to the distribution of power (unlike $\mathrm{err}^{\bar{P}_{\mathrm{tot}}}$), they are relatively easy to compute compared to pointwise error norms (see note 2 below), and they are single numbers at each frequency (unlike $\mathrm{err}^{\bar{\bar{P}}}$) that can be used to analyze the tradeoffs between computation costs and accuracy. The L∞-norm provides a worst-case bound on the error that can be valuable when the simulations are used to ensure safety standards are met. While the L∞-norm provides a global maximum, it still only reports the error at one point. The L1-norm captures the errors over the entire domain.

Error Measure 5: Relative Error of the Power Absorbed in Different Tissues

The last error measure is the *relative error of the power absorbed in each tissue* T:

$$\mathrm{err}^{\bar{P}_{\mathrm{tissue}_T}}(\omega)=\frac{\left|\bar{P}_{\mathrm{tissue}_T}^{\mathrm{ref}}(\omega)-\bar{P}_{\mathrm{tissue}_T}(\omega)\right|}{\bar{P}_{\mathrm{tissue}_T}^{\mathrm{ref}}(\omega)}. \tag{69}$$

This error norm is more sensitive than $\mathrm{err}^{\bar{P}_{\mathrm{tot}}}$ to the location of the errors; indeed, it can even be more sensitive than $\mathrm{err}_{\mathrm{L1}}^{\bar{\bar{P}}_{\mathrm{cell}}}$ to errors in small or localized tissues (e.g., eyes) that absorb relatively small amounts of power. For large tissues, however, it suffers from the same limitations as $\mathrm{err}^{\bar{P}_{\mathrm{tot}}}$ —a simulation that yields a very inaccurate power density can have a very small $\mathrm{err}^{\bar{P}_{\mathrm{tot}}}$; see Figure 15 vs. Figure 16 in Chapter 4.1—and becomes a poor measure for comparing numerical methods.

Note 1: Insensitivity to Cold Spots

It should be observed that all five error measures emphasize the errors in cells that absorb more power (hot spots) over those that absorb less power (cold spots). This effect can be seen in Figure 9, where $\mathrm{err}^{\bar{P}_{\mathrm{tot}}}$, $\mathrm{err}_{\mathrm{L}\infty}^{\bar{\bar{P}}}$, and $\mathrm{err}_{\mathrm{L1}}^{\bar{\bar{P}}}$ are an order of magnitude larger in scenario 2 compared to scenario 3 and the warmest color in visualization of $\mathrm{err}^{\bar{\bar{P}}}$ is orange in scenario 2 and aquamarine in scenario 3, despite both scenarios having the same $+20\%$ and -10% relative error in two cells. In this thesis, this type of measure is preferred over other measures that are more sensitive to errors in cold spots [75], [76] because a major function of BioEM simulators is to quantify whether the power absorbed by the whole model, the power absorbed by specific tissues in the model, or the peak absorbed power density remain below safety thresholds and because errors made in hot spots are more important than the errors made in cold spots for these purposes.

Note 2: Cellwise vs. Pointwise Error Norms

While both pointwise error norms (e.g., $\mathrm{err}_{\mathrm{L}\infty}^{\bar{P}}, \mathrm{err}_{\mathrm{L1}}^{\bar{P}}$) and cellwise error norms (e.g., $\mathrm{err}_{\mathrm{L}\infty}^{\bar{\bar{P}}}, \mathrm{err}_{\mathrm{L1}}^{\bar{\bar{P}}}$) require the evaluation/integration of $\mathrm{err}^{\bar{P}} = \bar{P}^{\mathrm{ref}} - \bar{P}$, there are three major differences between cellwise and pointwise computation of the norms. First, $\mathrm{err}^{\bar{P}}$ is a continuous function whereas $\mathrm{err}^{\bar{\bar{P}}}$ is a piecewise continuous function that is constant over each cell used in the analysis. Second, cellwise error norms average $\mathrm{err}^{\bar{P}}$ over each cell

before finding its maximum/integrating it; thus, they in general give smaller values than pointwise error norms. Third, and most importantly, $\bar{P}^{\text{ref}}$ and $\bar{P}$ must be evaluated at the same points to calculate pointwise error norms (i.e., to evaluate/integrate $\text{err}^{\bar{P}} = \bar{P}^{\text{ref}} - \bar{P}$), whereas they must only be evaluated at the same cells to calculate cellwise error norms (i.e., to evaluate/integrate $\text{err}^{\bar{\bar{P}}} = \bar{\bar{P}}^{\text{ref}} - \bar{\bar{P}}$). In other words, cellwise error norms can be found by independently computing $\bar{P}^{\text{ref}}_{\text{cell}_k}(\omega) = \iiint_{V_k} \bar{P}^{\text{ref}}(\mathbf{r},\omega)\,dV$ and $\bar{P}_{\text{cell}_k}(\omega) = \iiint_{V_k} \bar{P}(\mathbf{r},\omega)\,dV$ rather than by computing $\iiint_{V_k} \left|\bar{P}^{\text{ref}}(\mathbf{r},\omega) - \bar{P}(\mathbf{r},\omega)\right| dV$ in each cell k. This is a significant advantage for cellwise error norms because it is often difficult to accurately integrate $\bar{P}^{\text{ref}}$ and $\left|\bar{P}^{\text{ref}} - \bar{P}\right|$ over the volume V_k: standard cubature rules will often not yield accurate results. This difficulty arises because different representations/ approximations of the volume are used to find $\bar{P}^{\text{ref}}$ and $\bar{P}$ in general; as a result, $\bar{P}^{\text{ref}}$ can vary sharply and even be discontinuous when a change in tissues is encountered in the reference model within V_k. Because $\bar{P}^{\text{ref}}$ and $\bar{P}$ integrations are independent in the cellwise error norms, the complicated integrals can be performed once for each mesh, the reference result in each cell of the mesh can be stored, and the results can be reused whenever needed. Pointwise error norms would have to repeat the complicated integrals every time a new $\bar{P}$ is to be evaluated.

For example, in Chapter 4, cellwise error norms for the spherical phantom are calculated by using a Mie series result as reference. When cells cross analytical boundaries (e.g., the support of the cell belongs to two layers of the multilayered sphere), standard cubature rules fail to give accurate results due to the discontinuity in $\bar{P}^{\text{ref}}$ that occurs at the analytical boundary; thus, $\bar{P}^{\text{ref}}$ is integrated adaptively using a recursive algorithm:

(i) Check if the smallest circumsphere centered at the centroid of the cell crosses an analytical boundary. If the circumsphere belongs to more than one layer, then subdivide the cell. Check the circumsphere for each subcell; repeat the subdivision

until the circumsphere belongs to only one layer. For each (sub)cell whose circumsphere resides in a single layer, perform step (ii).

(ii) Use a standard cubature rule to compute the integral over the (sub)cell. To ensure that the cubature rule has accurately calculated the integral, subdivide the cell, calculate the integral over each subcell, add the results, and compare to the integral. If the two results agree within a threshold (within 10^{-4} of each other for the Mie series reference in Chapter 4) then return the result obtained using the subcells (which should be more accurate than the cubature over the original cell). If the convergence criterion is not met; repeat step (ii) for each of the subcells.

In this thesis, the cells are always subdivided into 8 subcells of the same shape: tetrahedral cells are refined using uniform octasection refinement [77] and voxel cells are divided into 8 subvoxels at their centroid. In Chapter 4, the recursion continues for a maximum of 4 subdivisions (at which point the subcells have a volume of $V_k / 8^4 = V_k / 4096$).

Note 3: Assessing Accuracy without a Reliable Reference

All five error measures rely on a reference solution. Unfortunately, for the most complex models (e.g., the anatomical models), a reliable reference is often not available and different methods can yield significantly different results. To assess the accuracy of the methods without a reliable reference, the following approach is used: Increasingly higher resolutions of the model are simulated, $\bar{P}_{\text{tot}}$ and various $\bar{P}_{\text{tissue}_T}$ values are calculated for the finest resolution models, and the range of values for $\text{err}^{\bar{P}_{\text{tissue}_T}}$ are plotted for different resolutions (similar to an error-bar graph) by using the results from the finest resolution models (simulated by the same method) as reference. The computational costs of each simulation are also presented for the different resolutions. While it is not easy to deduce

the accuracy vs. cost tradeoff from such plots, they enable different methods to be compared even without a reliable reference.

3.2.2 Cost Measures

To compare the computational costs of the different methods, computation times and memory requirements are recorded for different stages of each simulation. The computation time is split into two parts: the *preprocessing time* and the *solve/marching time* (for FFT-accelerated integral equation methods/FDTD). The preprocessing time consists of processing the mesh and filling the relevant matrices for FFT-accelerated integral equation methods; it consists of reading the input parameters from disk, filling in (averaging) material properties, and setting up the grid (including the PML) for FDTD. The solve time consists of filling the right-hand-side (the tested incident field) plus the time the iterative solver takes to converge once the iterations start for FFT-accelerated integral equation methods. The marching time is the time needed to march through all the time steps for FDTD. For simulations involving multiple excitations, such as a sweep over incident plane waves from different directions (e.g., see [23]), the solve/marching time dominates the preprocess time which occurs just once. Therefore, more significance is given to the solve/marching time when analyzing computational costs.

Given the complexity of the problems solved and the increasing importance of parallel computing, BioEM simulations are often performed on parallel computers; in fact, several of the larger-scale simulations in this thesis were performed in parallel. A comprehensive comparison of the parallel efficiency and scalability of the different methods, which would require a multitude of potentially low-efficiency simulations for the different parallel algorithms [23], [57], is out of the scope of this thesis. Instead, all of the simulations in Chapter 4 are performed using the smallest number of processes dictated by

the memory available to each processor and the computer time that could be afforded. The computational costs of the parallel runs are serialized as

$$\begin{aligned} M_{\text{serialized}} &= P \max_{1 \le i \le P} M_i \\ T_{\text{serialized}} &= P T_{\text{wall}}, \end{aligned} \tag{70}$$

where T_{wall} is the wall-clock (parallel) compute time, M_i is the maximum memory required by process i, and P is the total number of processes used.

3.2.3 Accuracy-Efficiency Tradeoffs

To identify the potentially different accuracy-efficiency tradeoffs of different methods, plots of error vs. computational cost are used in this thesis. These plots are drawn by varying the model resolution/mesh density and optimizing the parameters of the numerical method to minimize both the error and the computational costs; indeed, the ideal simulation would yield no errors and use zero computational resources. In a plot of error vs. cost, such a simulation would be represented by the origin of the plot.

Chapter 4: Results

In this Chapter, the performance of GMRES-FFT, AIM, and FDTD are compared and the effects of three factors (frequency, excitation type, model complexity) on the comparison are investigated using the benchmark problems and performance criteria detailed in Chapter 3. To facilitate the comparison, a baseline case is presented first and then differences are observed as the factors of interest are modified one at a time.

The simulations were carried out on Stampede at the Texas Advanced Computing Center (TACC) [78]. Each computing node on Stampede has two Intel Xeon E5-2680 2.7 GHz 8-core processors for a total of 16 cores with 32 GB of memory per node. Each simulation was constrained to a maximum wall-clock time of 48 hours and a maximum of 32 GB memory/process; as mentioned in Chapter 3.2.2, the minimum number of processes that satisfied these constraints were used in the following simulations and the computational costs were serialized. Further details, including the number of processes used for each simulation, can be found in Appendix B.

4.1 Baseline Case – Multilayered Spherical Head Phantom Excited by a 900 MHz Plane Wave

Among the various benchmark problems, the multilayered spherical head phantom illuminated at 900 MHz with a unit-magnitude plane wave ($E_0^{\text{inc}} = 1,\ \hat{\mathbf{p}}_{\text{PW}} = -\hat{\mathbf{x}},\ \hat{\mathbf{k}} = -\hat{\mathbf{z}}$) was selected as the baseline case. The spherical phantom was chosen because an analytical Mie series reference solution can be used to calculate the error measures, 900 MHz was chosen because it is the middle frequency of interest, and the plane-wave excitation was chosen because the incident field is simpler/varies less than that for the Hertzian dipole excitation.

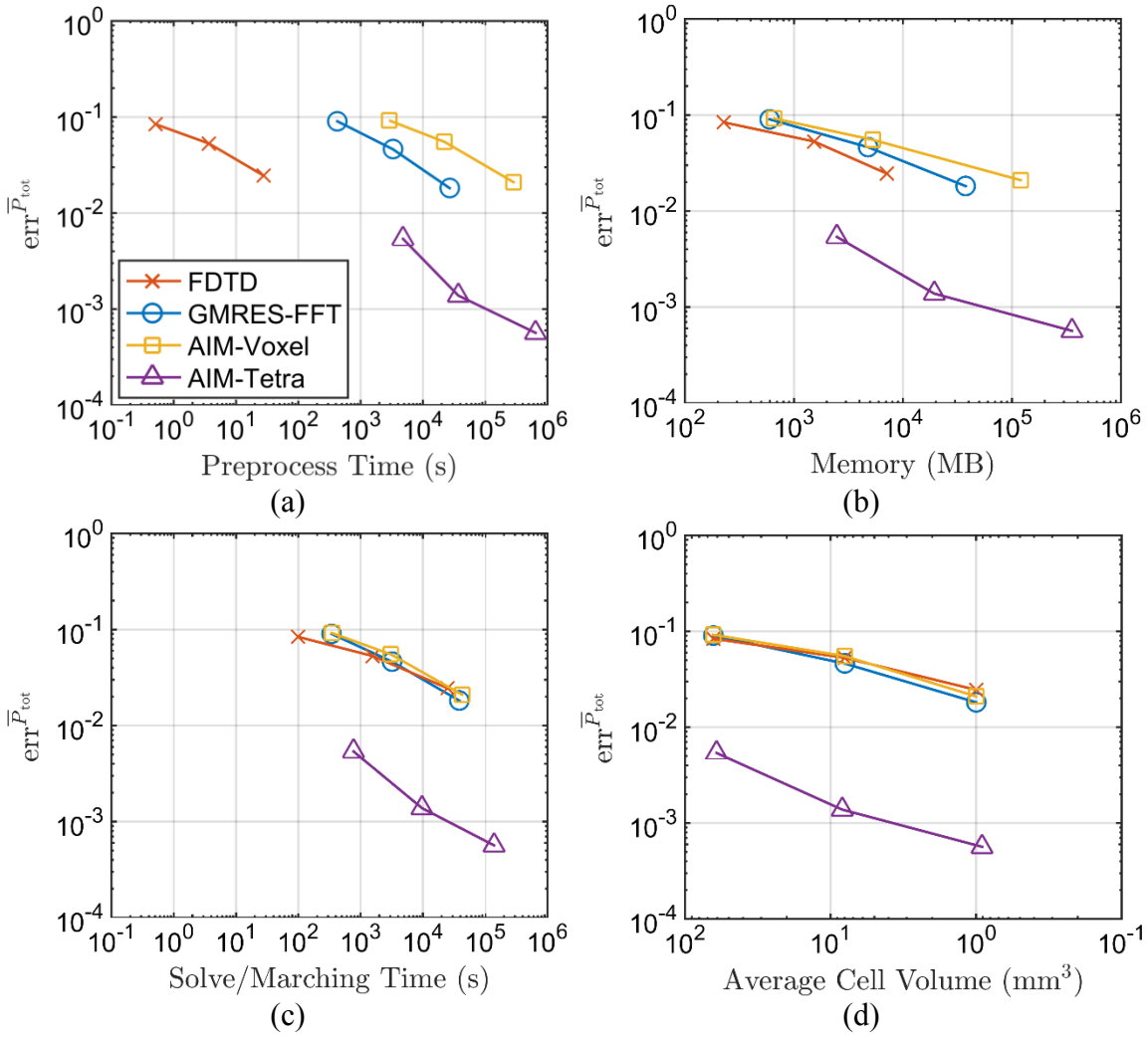

Figure 10: Accuracy-efficiency tradeoffs of the methods for the multilayered spherical head phantom excited by a 900-MHz plane wave. The relative error of $\overline{P}_{\text{tot}}$ is plotted vs. the (a) preprocess time, (b) memory, (c) solve/marching time, and (d) average cell volume as model resolution increases.

First, the total time-averaged power absorbed by the head phantom is computed for various model resolutions and the results are compared to the Mie series solution, which is $\overline{P}_{\text{tot}}^{\text{ref}} = 69.69853\ \mu\text{W}$ [73]. The relative error made in each simulation is plotted vs. the computational costs of that simulation and the average cell volume used in the simulation in Figure 10. Figure 10(d) shows that when a pixel-based model and voxel cells are used,

all three methods (GMRES-FFT, AIM-Voxel, and FDTD) compute the total time-averaged absorbed power with about the same accuracy and when surface-based model and tetrahedral cells are used, AIM achieves results that are one- to two-digits more accurate for the same average cell volume. Figure 10(a)-(c) show that FDTD has a significantly lower preprocess time (about 3 orders of magnitude), somewhat lower memory requirement (about 1 order of magnitude), and about the same solve/marching time cost compared to other methods that use voxel cells[5,6]. The error-vs.-cost tradeoff in Figure 10(a) shows that FDTD data is closer to the origin even compared to the AIM-Tetra case, suggesting that the method is superior to all three alternatives when $\mathrm{err}^{\bar{P}_{\mathrm{tot}}}$ is used as the error measure and the preprocess time is used as the cost measure. Figure 10(b)-(c) show, however, that FDTD performance is comparable to GMRES-FFT and AIM-Voxel, whereas the AIM-Tetra results are closest to the origin; i.e., when using surface-based models and tetrahedral cells, AIM is superior to the other three numerical methods when $\mathrm{err}^{\bar{P}_{\mathrm{tot}}}$ is the error measure and memory requirement or solve/march time are the cost measures. Even though the preprocess times in Figure 10(a) are comparable or larger than the solve/marching time for FFT-accelerated integral equation solvers, as mentioned in Chapter 3.2.2, less emphasis should be placed on the preprocess time as a cost measure because it can be amortized; e.g., it becomes negligible for multiple excitations. Thus, the results in Figure 10 indicate that AIM using tetrahedral cells has the best performance out of the four methods and should be the preferred numerical method for this problem.

---

[5] The higher preprocess time and memory requirement of FFT-accelerated IE methods when using voxels is primarily because of the computationally intensive integrals and the memory space required for filling and storing the relevant portions of the MOM impedance matrix $\mathbf{Z}$.

[6] The GMRES-FFT preprocessing time can be reduced further (by upto a factor of 10) relatively easily by exploiting redundancies that arise because the voxels are not only regular but also uniform (i.e., $\Delta x = \Delta y = \Delta z$). These improvements were not adopted in this thesis, however, to keep the formulation and implementation more general. Moreover, as explained later in the paragraph, preprocessing time is a less important cost measure than solve time and memory requirement.

While $\mathrm{err}^{\bar{P}_{\mathrm{tot}}}$ is of interest for whole-body safety standards [9], [74], it is a rather insensitive error measure and a low $\mathrm{err}^{\bar{P}_{\mathrm{tot}}}$ does not imply that other quantities of interest, such as the absorbed power density, are computed accurately (see Figure 9 in Chapter 3.2.1). Alternatively, the errors can be quantified by visualizing the cell-averaged time-averaged absorbed power density $\bar{\bar{P}}$ and its absolute error $\left|\mathrm{err}^{\bar{\bar{P}}}\right|$ compared to a reference result. The Mie series reference results are plotted in Figure 11 and $\bar{\bar{P}}$ is plotted for the different methods in Figure 12 as the cell sizes are varied. The two figures show that the absorbed power density is large in the skin layer, small in the fat and bone-average layers, and has a hot spot near the center of the brain-average layer. Despite noticeable differences in the peak values of $\bar{\bar{P}}$ and minor differences on the surface and interior cold spots, the power distributions in Figure 12 all appear quite similar. Visualizing the error $\left|\mathrm{err}^{\bar{\bar{P}}}\right|$ in Figure 13 makes it is easier to distinguish the simulation results. Figure 13 shows that the largest errors are typically located in the skin layer (likely as a result of both higher field values and staircasing errors). Overall, the AIM-Tetra error levels are significantly lower than the methods that use pixel-based models; in the skin layer, the results have one to two orders of magnitude lower errors. The FDTD results have somewhat smaller internal error levels compared to the integral equation based methods that use voxel cells, while the maximum error is larger for the FDTD method and does not appear to converge with increased model resolution. In Figure 12, the GMRES-FFT and AIM-Voxel results appear identical, e.g., $\bar{\bar{P}}$ at the surfaces of the coarsest simulations have the same pattern; this is because both methods solve the same underlying MOM system of equations. Yet, there are additional (error-controllable) approximations in AIM compared to GMRES-FFT, which solves the MOM equations exactly (within machine precision). This implies that the errors for AIM-Voxel will not be identical to those for GRMES-FFT. Indeed, Figure 13 shows that $\left|\mathrm{err}^{\bar{\bar{P}}}\right|$ for AIM-Voxel is similar to but slightly higher than that for GMRES-FFT.

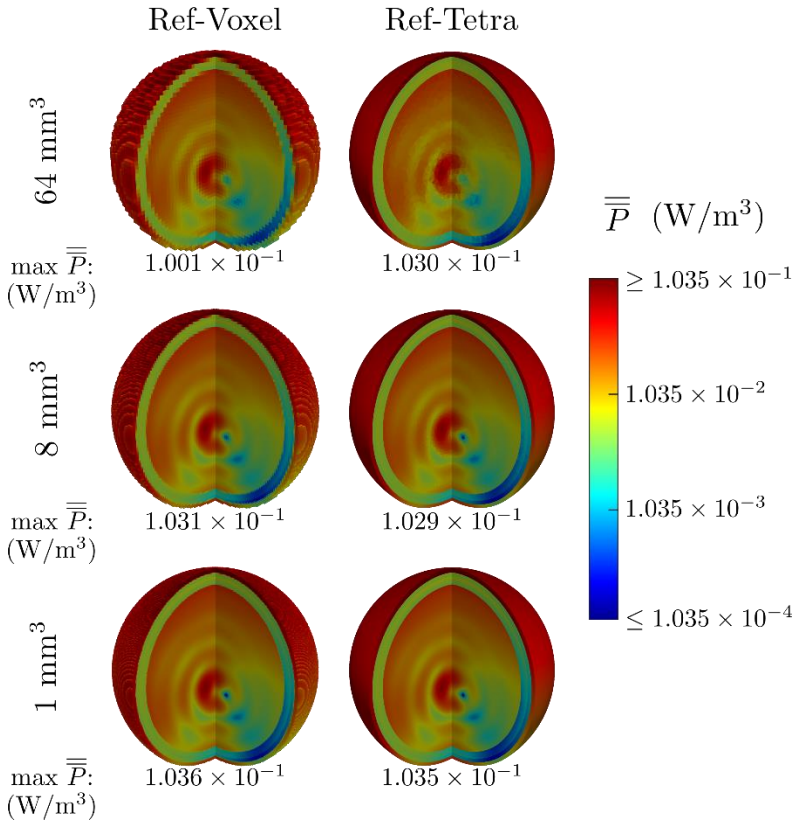

Figure 11: Mie series reference: Cell-averaged time-averaged absorbed power density when the head phantom is excited by a 900 MHz plane wave incident from the top of the model. The reference results are shown as the meshes are refined with average voxel (tetrahedron) volumes of 64 (60.7), 8 (8.32), and 1 (0.91) mm^3. One quadrant of the sphere is removed in the images to show the internal power density.

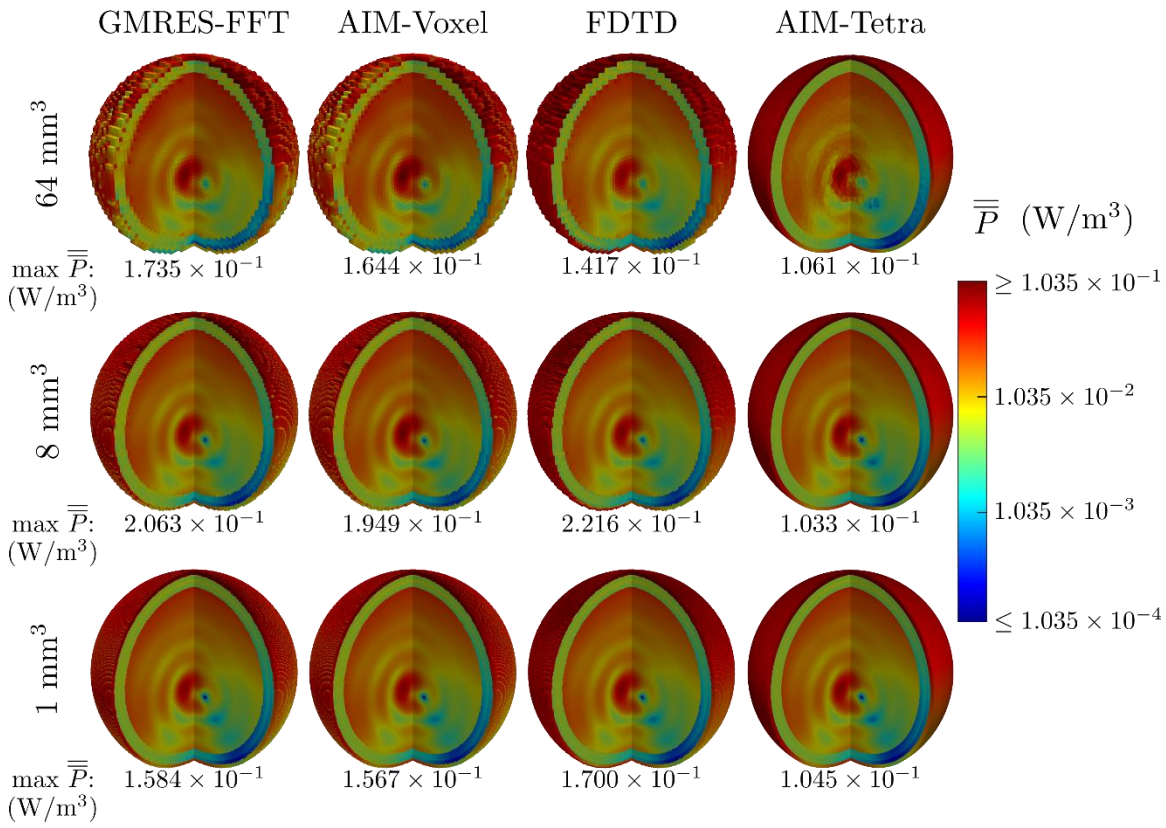

Figure 12: Cell-averaged time-averaged absorbed power density for the baseline case. The results from four different methods are shown: GMRES-FFT, AIM-Voxel, and FDTD use a pixel-based model and voxel cells; AIM-Tetra uses a surface-based model and tetrahedral cells. The meshes are refined for each method with average voxel (tetrahedron) volumes of 64 (60.7), 8 (8.32), and 1 (0.91) mm^3. One quadrant of the sphere is removed in the images to show the internal power density.

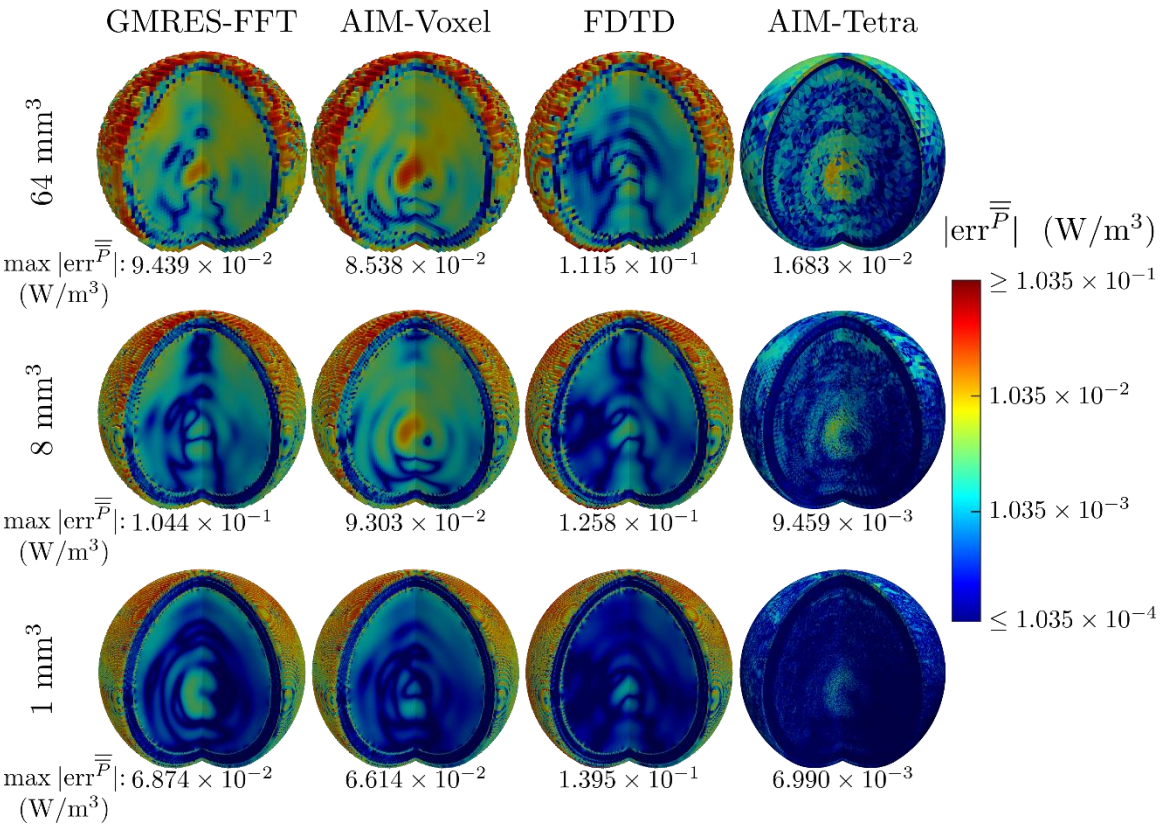

Figure 13: Errors in the absorbed power density plots in Figure 12. The maximum $\left|\text{err}^{\overline{\overline{P}}}\right|$ value in each image is also shown. The meshes are refined for each method with average voxel (tetrahedron) volumes of 64 (60.7), 8 (8.32), and 1 (0.91) mm^3. One quadrant of the sphere is removed in the images to show the internal errors

While the visualizations in Figure 11-Figure 13 are helpful in assessing the power density and its distribution (e.g., to identify hot spots or worst-case error spots), it is not clear how to correlate these images with the computational costs and to identify cost vs. error tradeoffs. The L∞- and L1-norm of the error of the cell-averaged time-averaged absorbed power density defined in (67) and (68) converts the errors visualized in Figure 13 into numbers that can be used in error-vs.-cost plots.

In Figure 14, $\text{err}_{\text{L}\infty}^{\overline{\overline{P}}}$ is plotted vs. the computational costs and average cell volume for each simulation. These plots show the costs associated with the maximum error in the

cell-averaged time-averaged absorbed power density (shown underneath each visualization in Figure 13) normalized by the maximum power density (shown underneath the visualizations in Figure 11); see (67). The AIM-Tetra results have about one extra digit of accuracy compared to other methods and show reasonable convergence as the mesh is refined. AIM-Voxel and GMRES-FFT show similar behavior (again, because they are solving the same underlying system of equations): the error decreases mildly from the coarsest to finest resolution while the results for the $2\times2\times2$ mm^3 cells have the highest error, indicating a somewhat inconsistent convergence trend. The FDTD results, on the other hand, show increasing error as the mesh is refined, which is an undesirable feature in a numerical method. Examining $\mathrm{err}_{L\infty}^{\bar{\bar{P}}}$ with respect to computational costs in Figure 14(a)-(c) suggest that AIM-Tetra should be the preferred method as it is the only method that consistently shows expected behavior for a numerical method (decreasing error as the cost is increased).

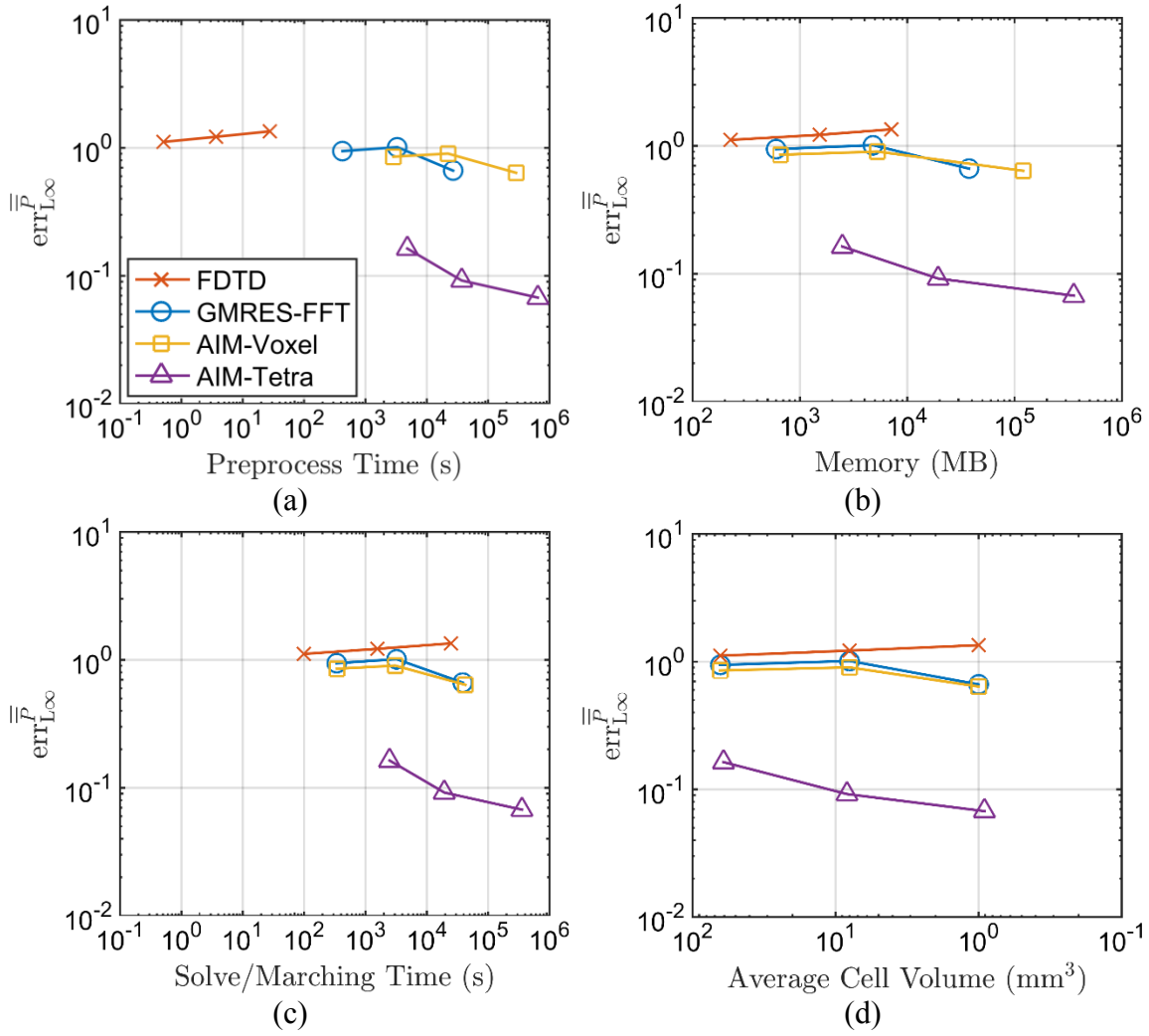

Figure 14: Accuracy-efficiency tradeoffs for the baseline case using the L∞-norm. The L∞-norm of $\overline{\overline{err}}^{\overline{P}}$ is plotted vs. the (a) preprocess time, (b) memory, (c) solve/marching time, and (d) average cell volume as the model resolution is increased.

In Figure 15, $\overline{\overline{err}}^{\overline{P}}_{L1}$ for each simulation is plotted vs. the computational costs of that simulation. According to the $\overline{\overline{err}}^{\overline{P}}_{L1}$ error measure, all of the numerical methods show expected accuracy behavior (decreasing error as costs are increased) unlike $\overline{\overline{err}}^{\overline{P}}_{L\infty}$ shown in Figure 14. In other words, even though FDTD, GMRES-FFT, and AIM-Voxel have difficulty improving their worst-case errors in the power density, improving the resolution

of the models does improve the overall power density computation. At first glance, the error-vs.-cost plots in Figure 15 appear similar to those in Figure 10 but with higher error due to the more sensitive error measure. Indeed, the general trends in the two figures are the same, e.g., AIM-Tetra outperforms the numerical methods using pixel-based models, which are comparable with respect to solve/marching time, and FDTD has a somewhat lower memory requirement and significantly lower preprocess time. Upon closer inspection, however, Figure 15 shows that the FDTD error is slightly lower than GMRES-FFT and AIM-Voxel ones, which agrees with the error visualizations in Figure 13. As a result, FDTD results move closer to the origin compared to GMRES-FFT and AIM-Voxel when $\mathrm{err}_{\mathrm{L1}}^{\overline{\overline{P}}}$ is used as the error measure, suggesting that FDTD is the best method for solving the baseline case (when only pixel-based models and voxel meshes are available). Nonetheless, AIM-Tetra still significantly outperforms FDTD with respect to memory and solve/marching time, while FDTD continues to hold the advantage for the less significant preprocess time.

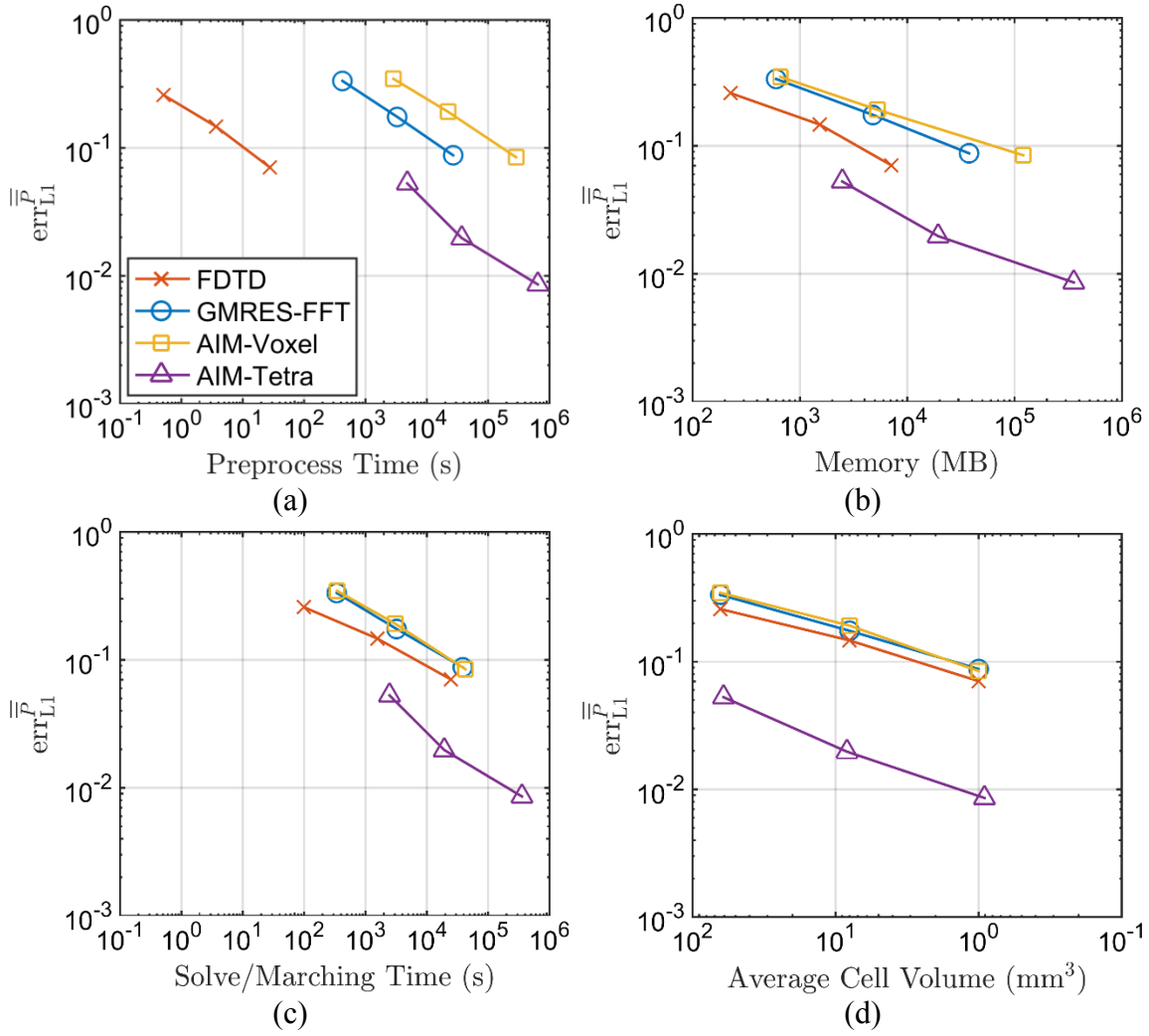

Figure 15: Accuracy-efficiency tradeoffs for the baseline case using the L1-norm. The L1-norm of $\mathrm{err}^{\bar{\bar{P}}}$ is plotted vs. the (a) preprocess time, (b) memory, (c) solve/marching time, and (d) average cell volume as the model resolution is increased.

Next, the accuracy-efficiency tradeoffs are quantified by using $\mathrm{err}^{\bar{P}_{\mathrm{tissue}_T}}$ as the error measure in Figure 16-Figure 18. Figure 17 shows that when estimating the total power absorbed in the brain layer (when $\mathrm{err}^{\bar{P}_{\mathrm{BrainAvg.}}}$ is used as the error measure), the relative performances of the methods remain essentially the same as those in Figure 15 (using $\mathrm{err}_{\mathrm{L1}}^{\bar{\bar{P}}}$ as the error measure). Figure 16 shows that FDTD performs especially poorly and

GMRES-FFT exhibits extraordinary convergence when estimating the total power absorbed in the skin layer (when $\mathrm{err}^{\bar{P}_{\mathrm{Skin}}}$ is used as the error measure). This is because, as mentioned in Chapter 3.2.1, whole-volume error norms are rather insensitive to errors and can be poor measures for judging numerical methods for large tissues. Results for other tissues are shown in Appendix C.

Lastly, Figure 18 presents the computational costs of the methods, their estimates for total power absorbed in different tissues, and $\mathrm{err}^{\bar{P}_{\mathrm{tissue}_T}}$ as function of the model resolution. The values for $\mathrm{err}^{\bar{P}_{\mathrm{tissue}_T}}$ shown in Figure 18(b) correspond to the simulations shown in Figure 18(a). Figure 18(a) shows that for a given average cell volume, all FDTD costs are lower than all other methods. Figure 18(b) shows that the estimated total power absorbed shows good agreement with Mie series result (within ~10% of the Mie series reference) in all the tissues when the finest resolution models are used, regardless of the method. Figure 18(b) also shows that AIM-tetra results have the lowest errors relative to the Mie series result. As mentioned in Note 3 in Chapter 3.2.1, it is not easy to deduce the accuracy vs. cost tradeoff from such plots. Unlike Figure 15, it is not clear that FDTD would require more computational resources than AIM-Tetra to reach the same level of errors. Indeed, while these plots can be used to identify the relative power absorbed in different tissues, the correlation among results from different methods, the range of uncertainty in the results due to model resolution, and to judge the performance of different methods *even when a reliable reference is missing*, the data should be considered very cautiously. It should be emphasized again that $\mathrm{err}^{\bar{P}_{\mathrm{tissue}_T}}$ is a poor error measure when large tissues are considered (see Section 3.2.1).

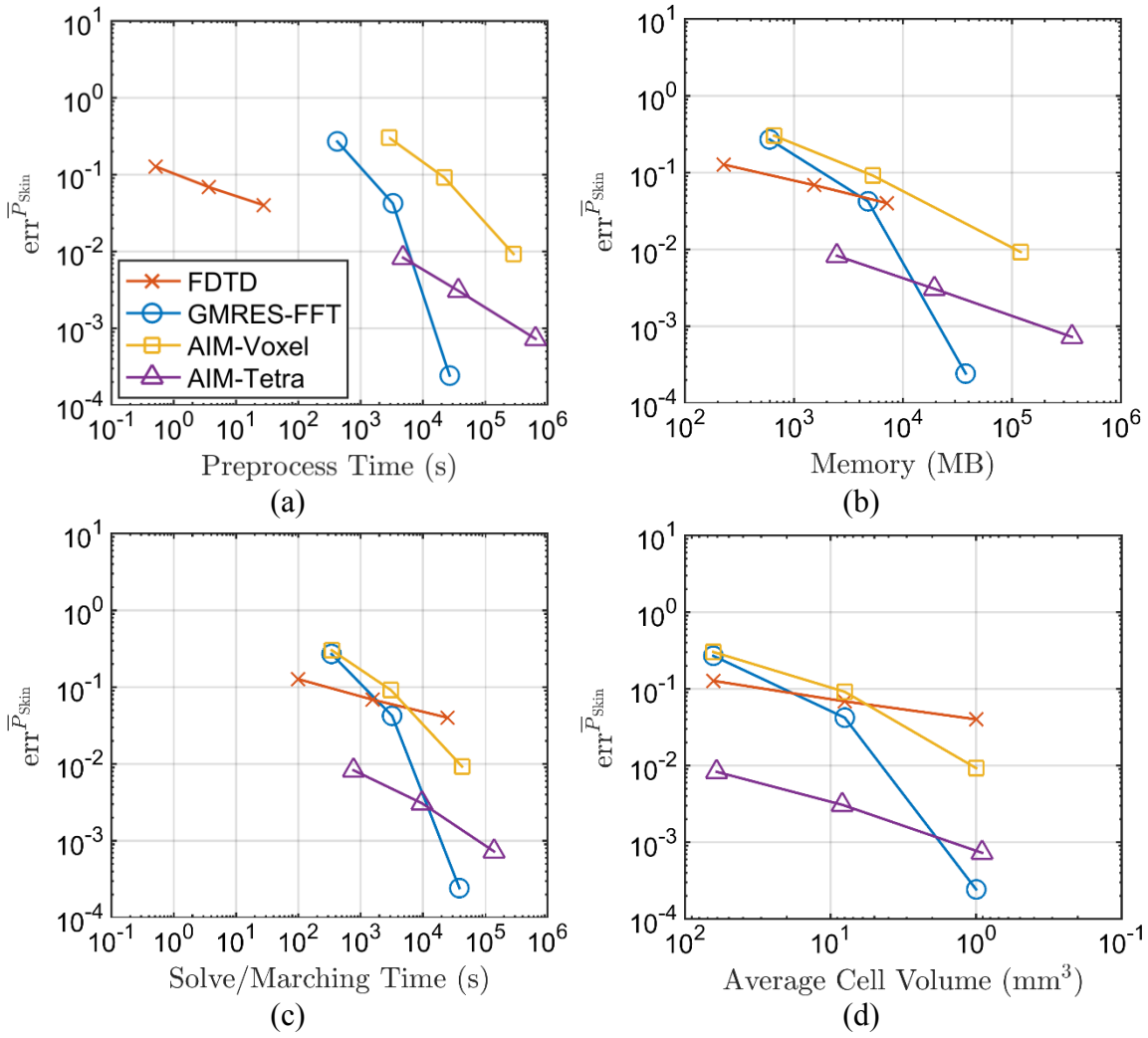

Figure 16: Accuracy-efficiency tradeoffs for the baseline case using the relative error of the power absorbed in the skin layer. The relative error of $\overline{P}_{\text{Skin}}$ is plotted vs. the (a) preprocess time, (b) memory, (c) solve/ marching time, and (d) average cell volume as the model resolution is increased.

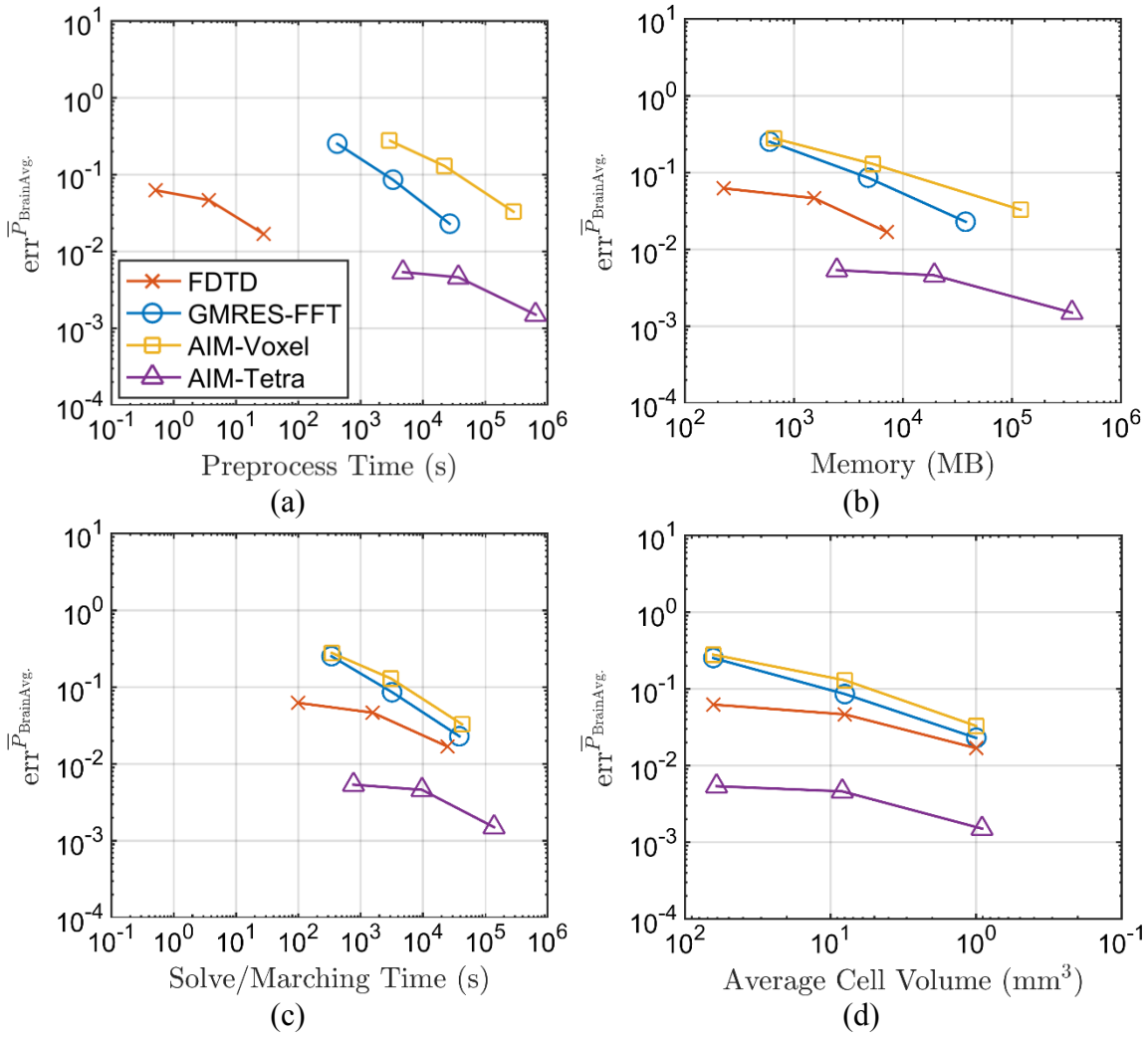

Figure 17: Accuracy-efficiency tradeoffs for the baseline case using the relative error of the power absorbed in the brain layer. The relative error of $\overline{P}_{\text{Brain Avg.}}$ is plotted vs. the (a) preprocess time, (b) memory, (c) solve/ marching time, and (d) average cell volume as the model resolution is increased.

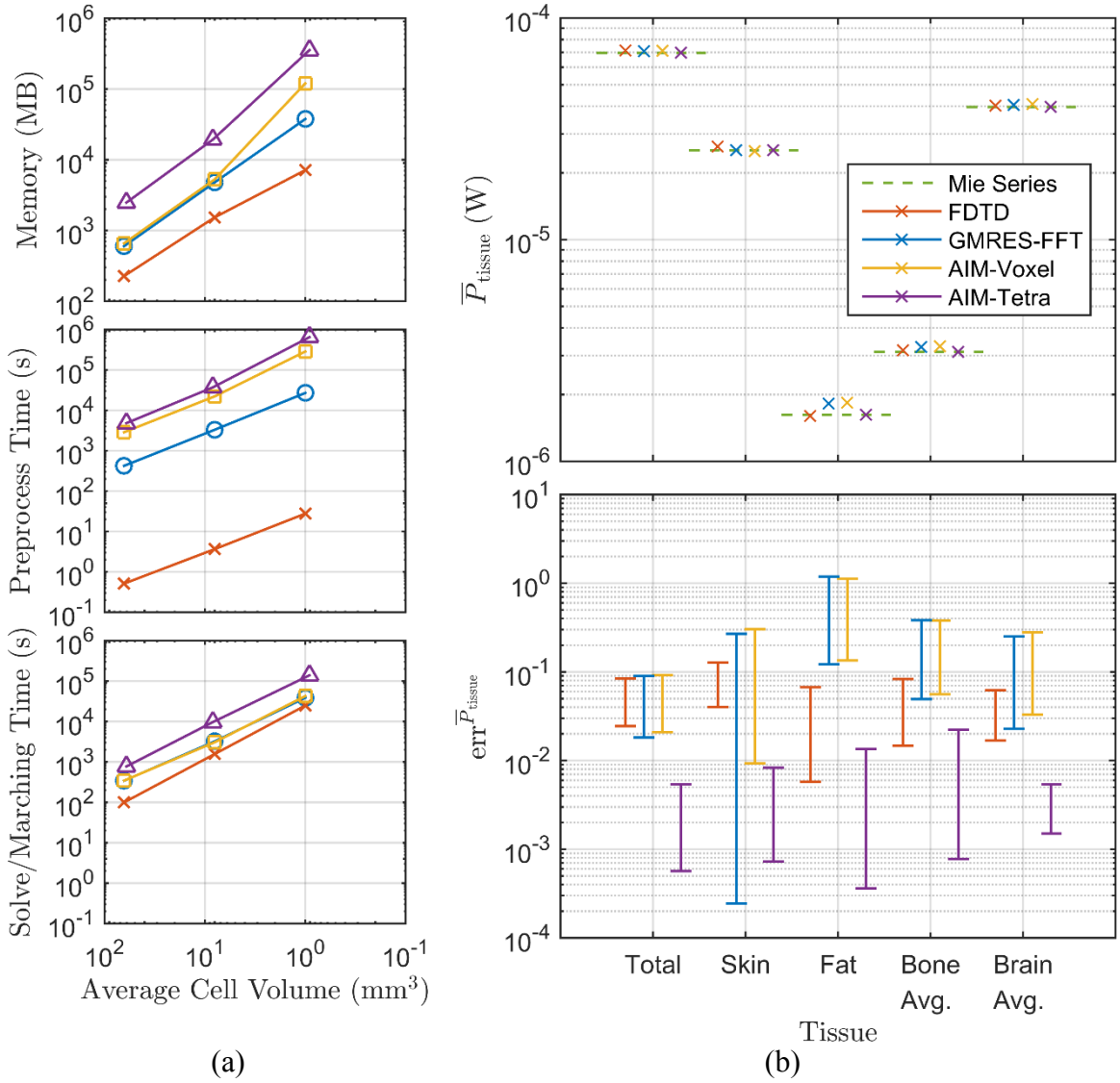

Figure 18: Costs and results of the methods for the multilayered spherical head phantom excited by a 900 MHz plane wave. (a) The computational costs vs. the average cell volume as the model resolution is increased. (b) Top: Plot of the total time-averaged absorbed power for each tissue of the head phantom for the finest mesh (1 mm^3) and the reference absorbed power from the Mie series. Bottom: The relative error made for each tissue as the mesh resolution is increased ($\overline{P}_{\text{tissue}}^{\text{ref}}$ is obtained from the analytical Mie series solution).

In the following, when an analytical reference solution exists (i.e., for the multilayered spherical head phantoms), the L1-norm of the cell-averaged power density

error (defined in (68)) is used as the error measure in the error-vs.-cost plots. When there is not an analytical reference (e.g., the AustinMan and AustinWoman anatomical models), to quantify the performance of the different numerical methods, the computational costs, the power absorbed by different tissues, and $\mathrm{err}^{\bar{P}_{\mathrm{tissue}_T}}$ are plotted (by using the finest resolution results as reference) as model resolutions are varied (similar to Figure 18).

4.2 Frequency Variation – 402 MHz, 2.45 GHz Cases

The head phantom is analyzed at 900 MHz (Figure 15) and two additional frequencies in the UHF band: 402 MHz (MICS band) and 2.45 GHz (ISM band). The results are shown in the error-vs.-cost plots using the L1-norm of the cell-averaged power density error (defined in (68)) in Figure 15, Figure 19, and Figure 20 for 900 MHz, 402 MHz, and 2.45 GHz, respectively. First, examining the error with respect to cell volume (subfigure d) between frequencies indicates that the error increases as the frequency increases; this is due to the wavelength decreasing while the scattering geometries are not changed, resulting in fewer cells per wavelength. This is particularly pronounced for the AIM-Tetra results at 2.45 GHz, which see a large jump in error compared to 900 MHz.

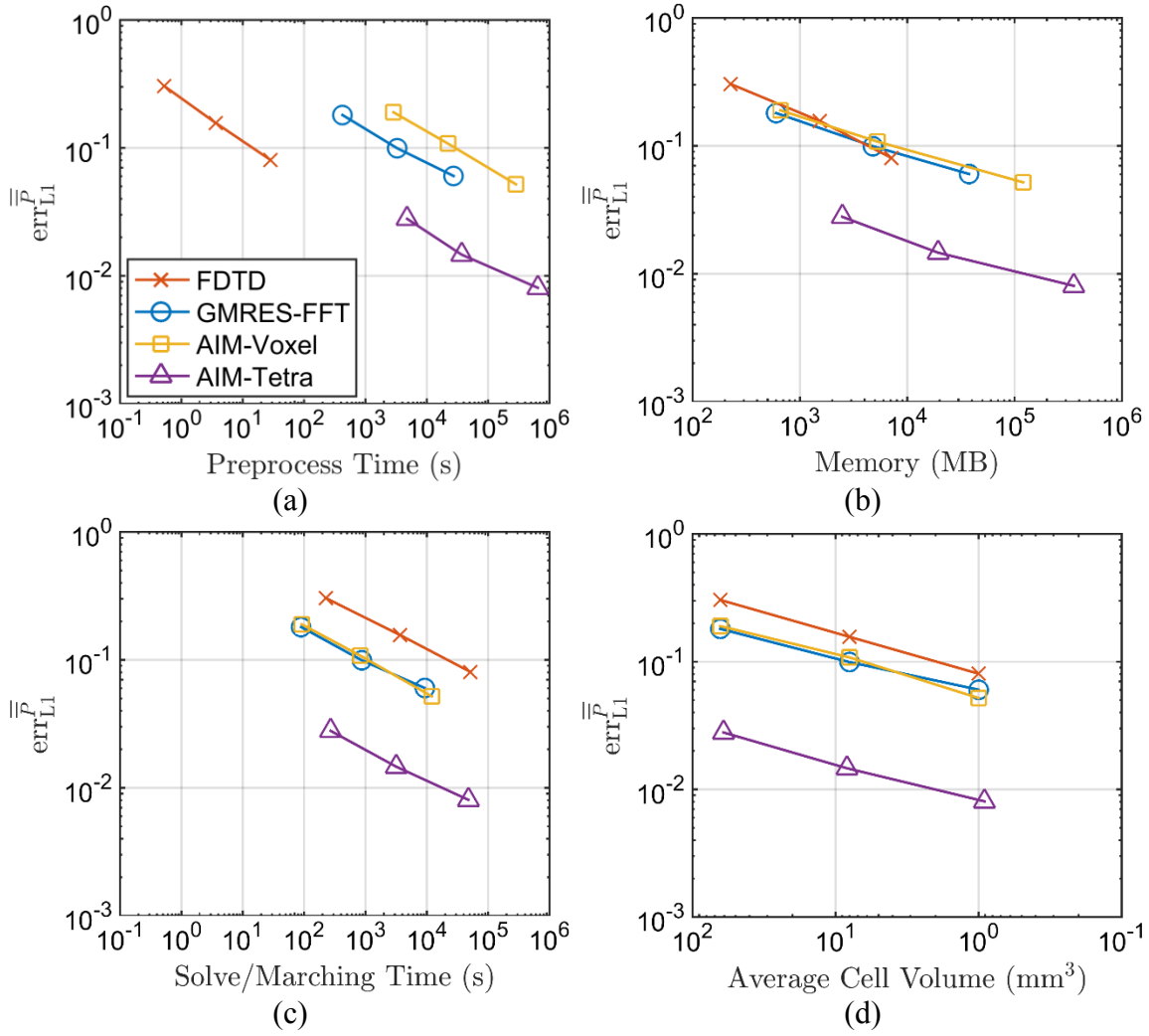

Figure 19: Accuracy-efficiency tradeoffs of the methods for the multilayered spherical head phantom excited by a 402-MHz plane wave. The L1-norm of $\overline{\overline{\mathrm{err}}}^{P}$ is plotted vs. the (a) preprocess time, (b) memory, (c) solve/marching time, and (d) average cell volume as the model resolution is increased.

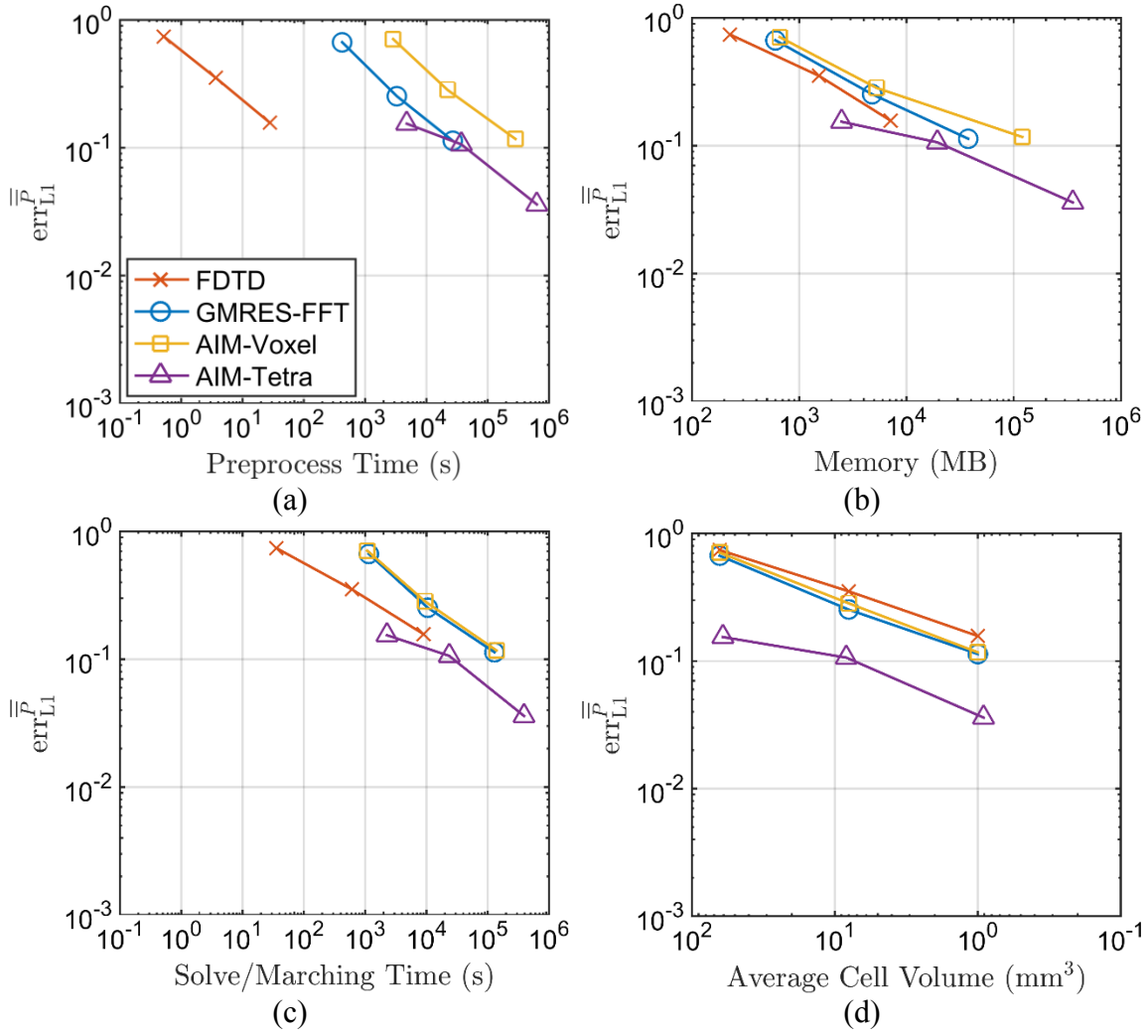

Figure 20: Accuracy-efficiency tradeoffs of the methods for the multilayered spherical head phantom excited by a 2.45 GHz plane wave. The L1-norm of $\overline{\overline{P}}$ is plotted vs. the (a) preprocess time, (b) memory, (c) solve/marching time, and (d) average cell volume as the model resolution is increased.

The preprocess time (subfigure a) and memory (subfigure b) are not strongly affected by frequency for any of the methods. As a result, the only shifts that occur in subfigures a and b between the figures are due to the changes in the error (y-axis). On the contrary, the solve/marching time is quite frequency dependent. For integral equation based methods, larger number of iterations are required for iterative solver convergence as the

frequency increases (see Table 22 in Appendix C). It is worth noting that for both GMRES-FFT and AIM, preconditioners could be applied to reduce the number of iterations required for convergence, which in turn would reduce the total solve time [79], [80]. For FDTD, the marching time decreases as the frequency increases; this is because shorter time intervals are simulated and the time-step sizes, which are dictated by the CFL condition for the meshes simulated, remain the same (thus, fewer number of timesteps are needed to achieve steady state, see Table 22 in Appendix C). These observations for the timing results are consistent with the BCG-FFT vs. FDTD comparison in [27].

Overall, in the error-vs.-cost plots for solve/marching time, AIM-Tetra outperforms FDTD for each of the frequencies investigated – significantly at 402 MHz with the performance gap decreasing as the frequency increases, resulting in almost comparable behavior at 2.45 GHz (with a slight edge to AIM-Tetra). Thus, if a surface-based model is available, the plots suggest that AIM should be used to obtain more accurate results for approximately the same cost compared to the other methods. Among the methods using pixel-based models, GMRES-FFT and AIM-Voxel have similar behavior at all frequencies and outperform FDTD at 402 MHz, are comparable with FDTD at 900 MHz (with a slight edge to FDTD), and have poorer performance than FDTD at 2.45 GHz. These results suggest that, when constrained to a voxel model, it is better to use integral equation based methods at lower frequencies and FDTD at higher frequencies, playing to each of the methods' strengths – lower iterations for integral equation based methods at low frequencies and fewer timesteps for FDTD at high frequencies. It should be noted that it is a significant achievement for the AIM algorithm, which is a more general purpose algorithm not limited to voxel meshes, to obtain comparable performance to GMRES-FFT algorithm for pixel-based models.

4.3 EXCITATION VARIATION – HERTZIAN DIPOLE CASE

Changing the excitation from a plane wave to a Hertzian dipole results in localized field distributions which are prominent when wireless devices are considered in BioEM analysis. Figure 21 shows the error-vs.-cost plots for excitation with a Hertzian dipole that should be compared to the results in Figure 15 obtained with a plane wave excitation.

First, examining the errors with respect to cell volume (Figure 15(d) vs. Figure 21(d)), there is a minor decrease in error when using a Hertzian dipole excitation for the numerical methods that use pixel-based models. AIM-Tetra still achieves the highest accuracy among the numerical methods; when confined to pixel-based models, FDTD yields slightly more accurate results compared to the FFT-accelerated integral equation methods.

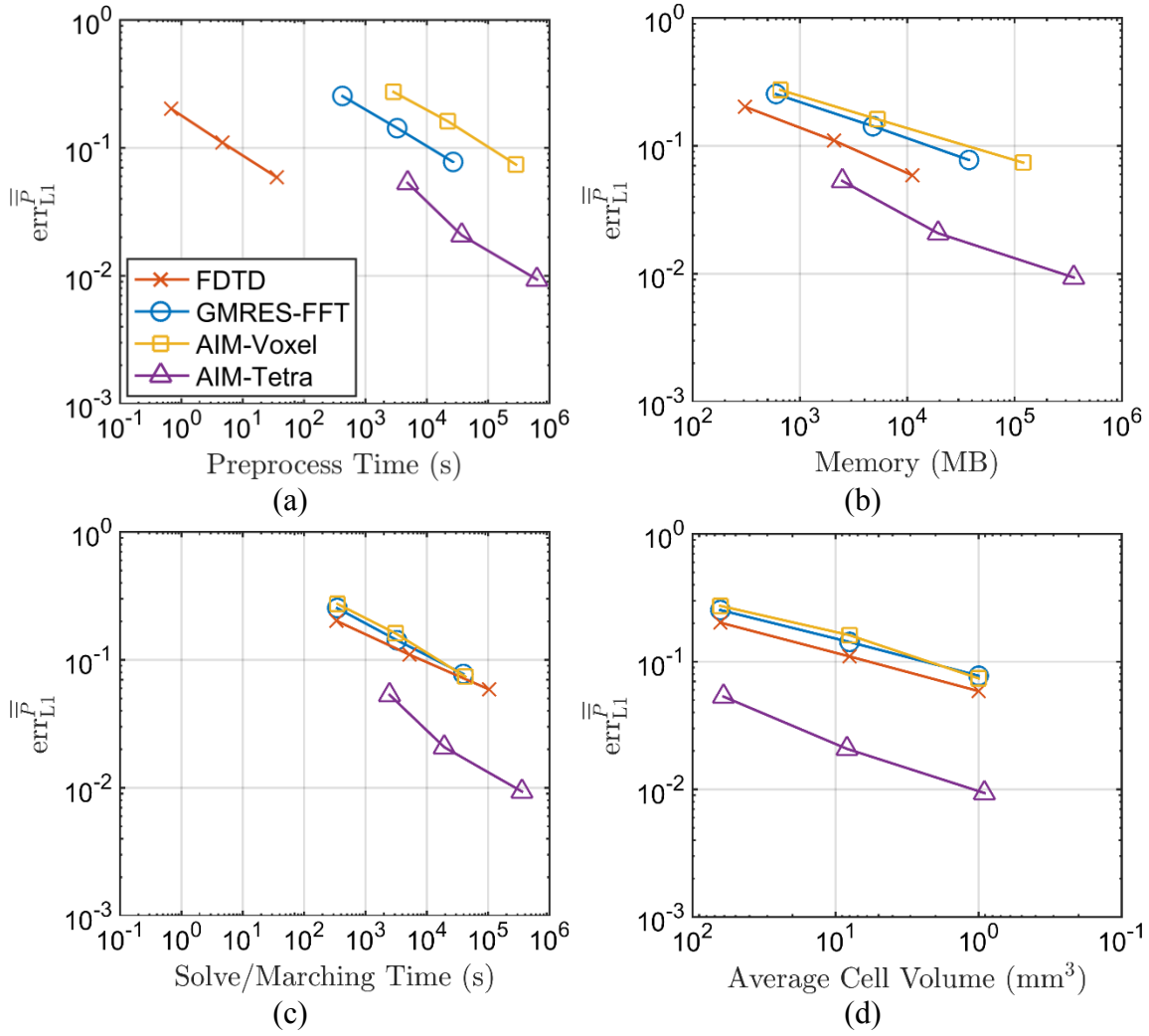

Figure 21: Accuracy-efficiency tradeoffs of the methods for the multilayered spherical head phantom excited by a Hertzian dipole. The dipole is $\hat{\mathbf{z}}$-oriented and located 50 mm away from the outermost surface of the sphere at (0.158m,0,0). The L1-norm of $\overline{\text{err}}^{P}$ is plotted vs. the (a) preprocess time, (b) memory, (c) solve/marching time, and (d) average cell volume as the model resolution is increased.

The preprocess time and memory costs are not dependent on the excitation and thus the results in Figure 21(a) and Figure 21(b) are nearly identical to the results shown in Figure 15(a) and Figure 15(b). The excitation does affect the solve/marching time

differently for each of the numerical methods. The FFT-accelerated integral equation methods have similar solve times for both excitations, while the marching time for FDTD increases due to the more complex formula for the incident field (55) which must be recalculated for each timestep making all of the methods that use voxel models comparable.

It should be noted that even though the Hertzian dipole excitation is provided to show how the numerical methods perform for localized field distributions, the incident field for all space and time is still obtained analytically. For more realistic examples of antennas placed near a human body, AIM is expected to yield significantly more accurate results due to its ability to better model the intricacies of complex antennas [81].

4.4 Model Variation – AustinMan and AustinWoman Cases

Next, the AustinMan and AustinWoman models are simulated. The models are excited by a normally incident 900 MHz plane wave from behind, which is the angle that the AustinMan model absorbs the most power [23]; the field magnitude is normalized to the ICNIRP reference strength ($E_0^{\text{inc}} = 58.34\,\text{V/m},\ \hat{\mathbf{p}}_{\text{PW}} = -\hat{\mathbf{z}},\ \hat{\mathbf{k}} = \hat{\mathbf{x}}$) [23], [74]. The total time-average power absorbed in a few select tissues of the models when the finest-resolution models are simulated are plotted in Figure 22 and Figure 23 and listed in Table 3 and Table 4. The data shows that there is a good agreement between the different numerical methods (less than ~10% difference for all tissues). Comparing the computational costs in Figure 22 and Figure 23 to those in Figure 18 indicate that FDTD marching time has improved relative to the iterative solution time for GMRES-FFT and AIM-voxel; this is because the number of iterations for the AustinMan and AustinWoman simulations are ~3 times higher than those for the spherical phantom (see Appendix C). The absorbed power density found by the three different methods using the finest-resolution models are visualized in Figure 24 and Figure 25.

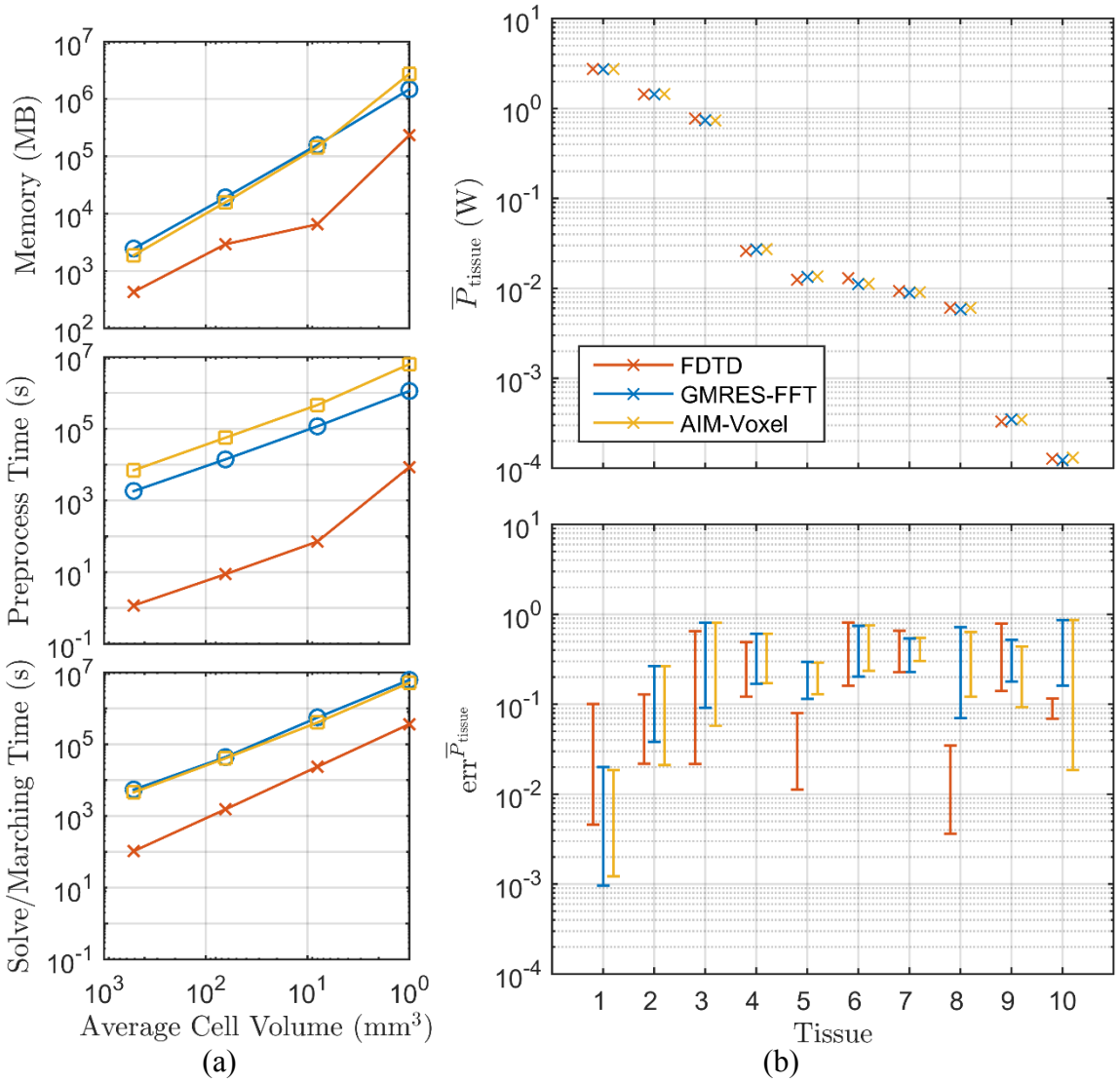

Figure 22: Costs and results of the methods for the AustinMan v2.2 model excited by a 900 MHz plane wave. (a) The computational costs vs. the average cell volume as the model resolution is increased. (b) Top: Plot of the absorbed power for select tissues of the AustinMan model for the finest mesh (1 mm^3). Bottom: The range of $\mathrm{err}^{\bar{P}_{\mathrm{tissue}}}$ for each tissue as the model resolution is increased. The reference, $\bar{P}_{\mathrm{tissue}}^{\mathrm{ref}}$, is found by using the finest model using the same method, i.e., the data plotted in the top.

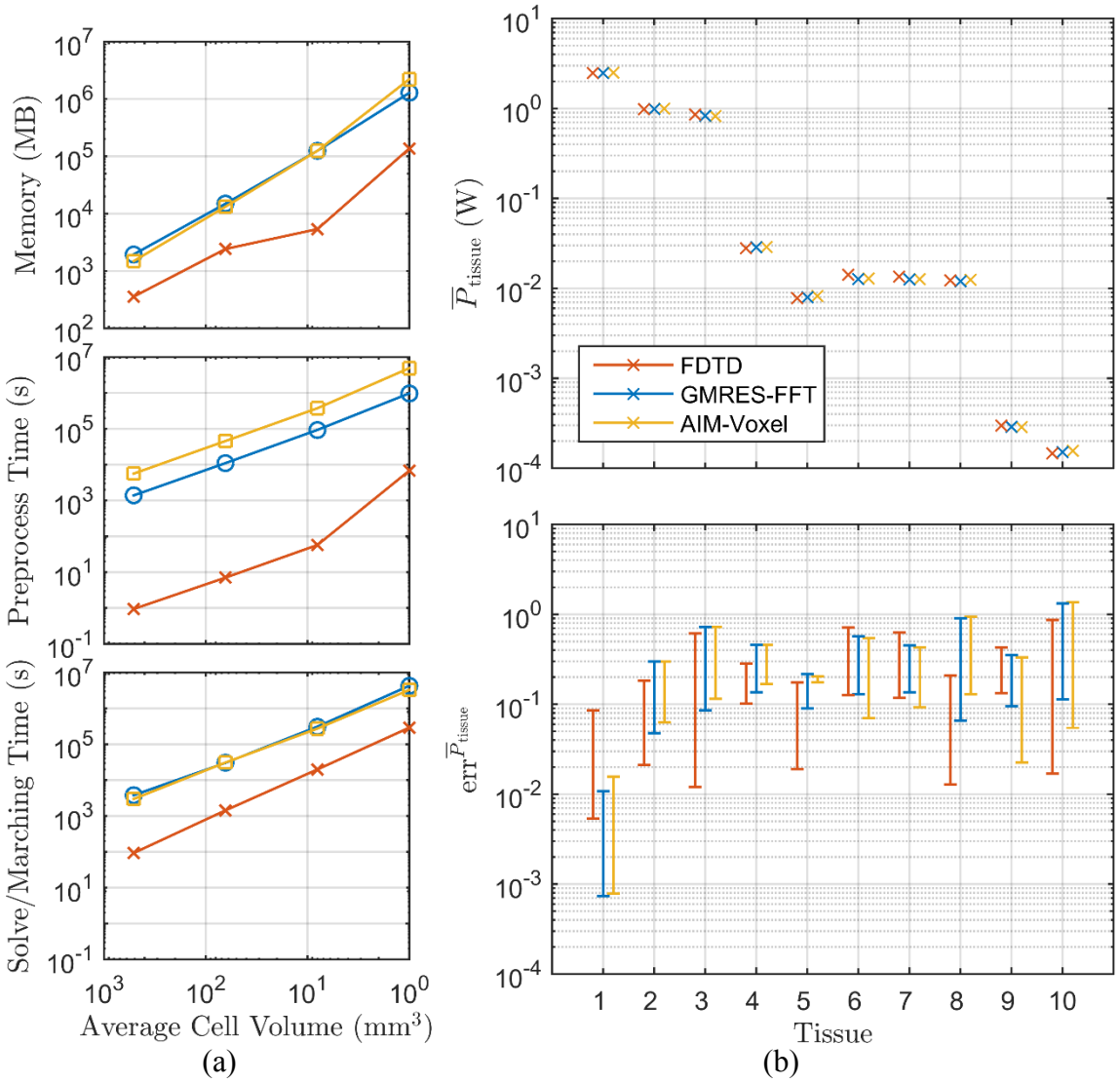

Figure 23: Costs and results of the methods for the AustinWoman v2.1 model excited by a 900 MHz plane wave. (a) The computational costs vs. the average cell volume as the model resolution is increased. (b) Top: Plot of the absorbed power for select tissues of the AustinWoman model for the finest mesh (1 mm^3). Bottom: The range of $\mathrm{err}^{\overline{P}_{\mathrm{tissue}}}$ for each tissue as the model resolution is increased. The reference, $\overline{P}_{\mathrm{tissue}}^{\mathrm{ref}}$, is found by using the finest model using the same method, i.e., the data plotted in the top.

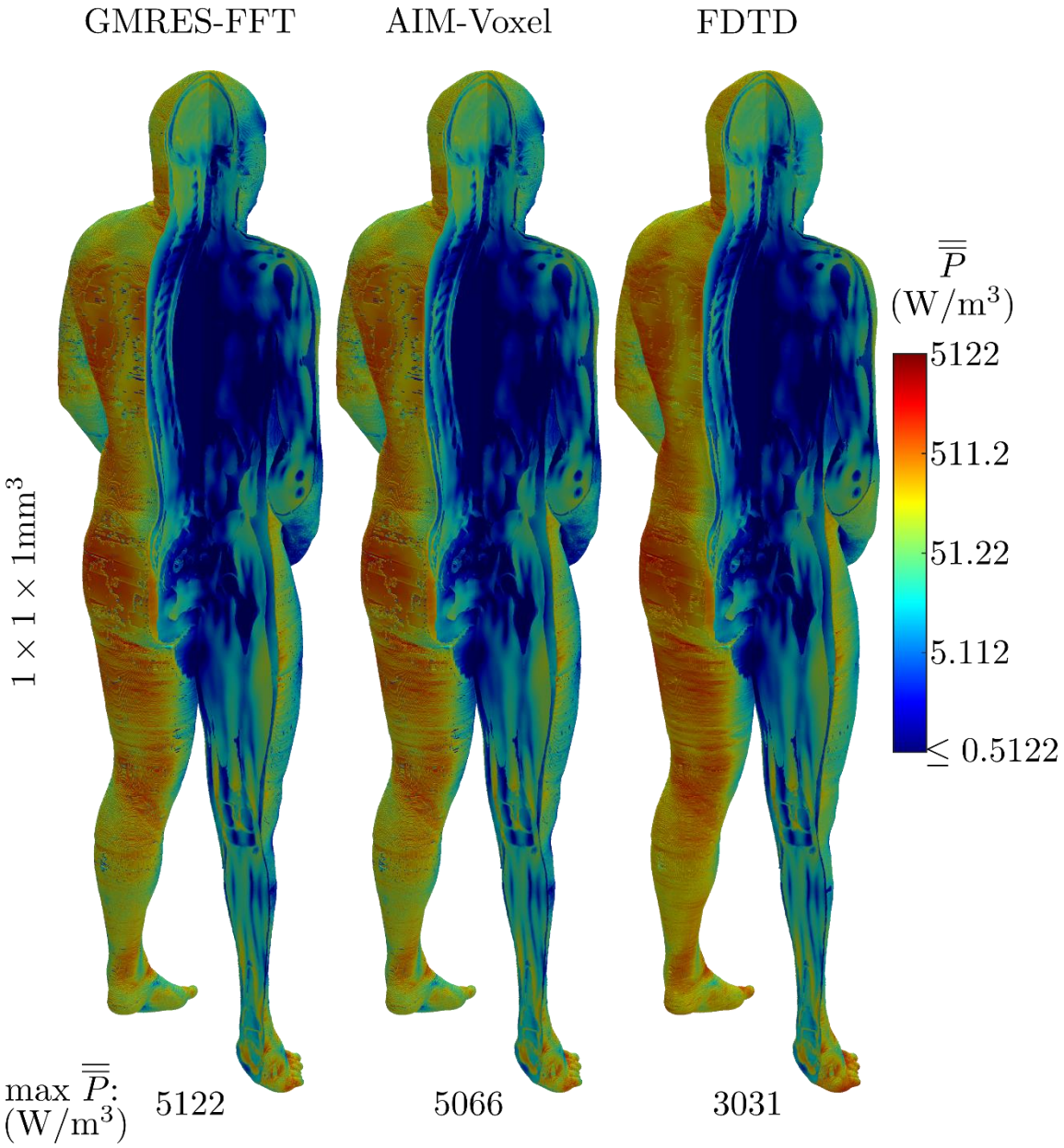

Figure 24: Cell-averaged time-averaged absorbed power density for the finest mesh of the AustinMan v2.2 model excited by a plane wave from behind. The results from three different methods are shown: GMRES-FFT, AIM-Voxel, and FDTD, all of which use a pixel-based model and voxel cells. One quadrant of the model is removed in the images to show the internal power density.

Table 3 Tissue absorbed power for the 1×1×1 mm^3 AustinMan v2.2

Tissue	**Plot ID**	**FDTD** $\overline{P}_{\text{tissue}}$ (W)	**GMRES-FFT** $\overline{P}_{\text{tissue}}$ (W)	**AIM-Voxel** $\overline{P}_{\text{tissue}}$ (W)	**Volume** (m^3)
Total	1	2.750E+00	2.736E+00	2.745E+00	1.020E+08
Muscle	2	1.439E+00	1.440E+00	1.451E+00	4.317E+07
Skin	3	7.720E-01	7.436E-01	7.352E-01	5.140E+06
Grey Matter	4	2.593E-02	2.700E-02	2.721E-02	7.000E+05
White Matter	5	1.249E-02	1.337E-02	1.360E-02	4.710E+05
Blood Vessel	6	1.292E-02	1.112E-02	1.119E-02	9.019E+05
Cerebro Spinal Fluid	7	9.355E-03	8.901E-03	9.020E-03	1.481E+05
Liver	8	6.069E-03	5.810E-03	6.086E-03	1.815E+06
Eye	9	3.315E-04	3.503E-04	3.473E-04	1.327E+04
Prostate	10	1.279E-04	1.226E-04	1.311E-04	1.949E+04

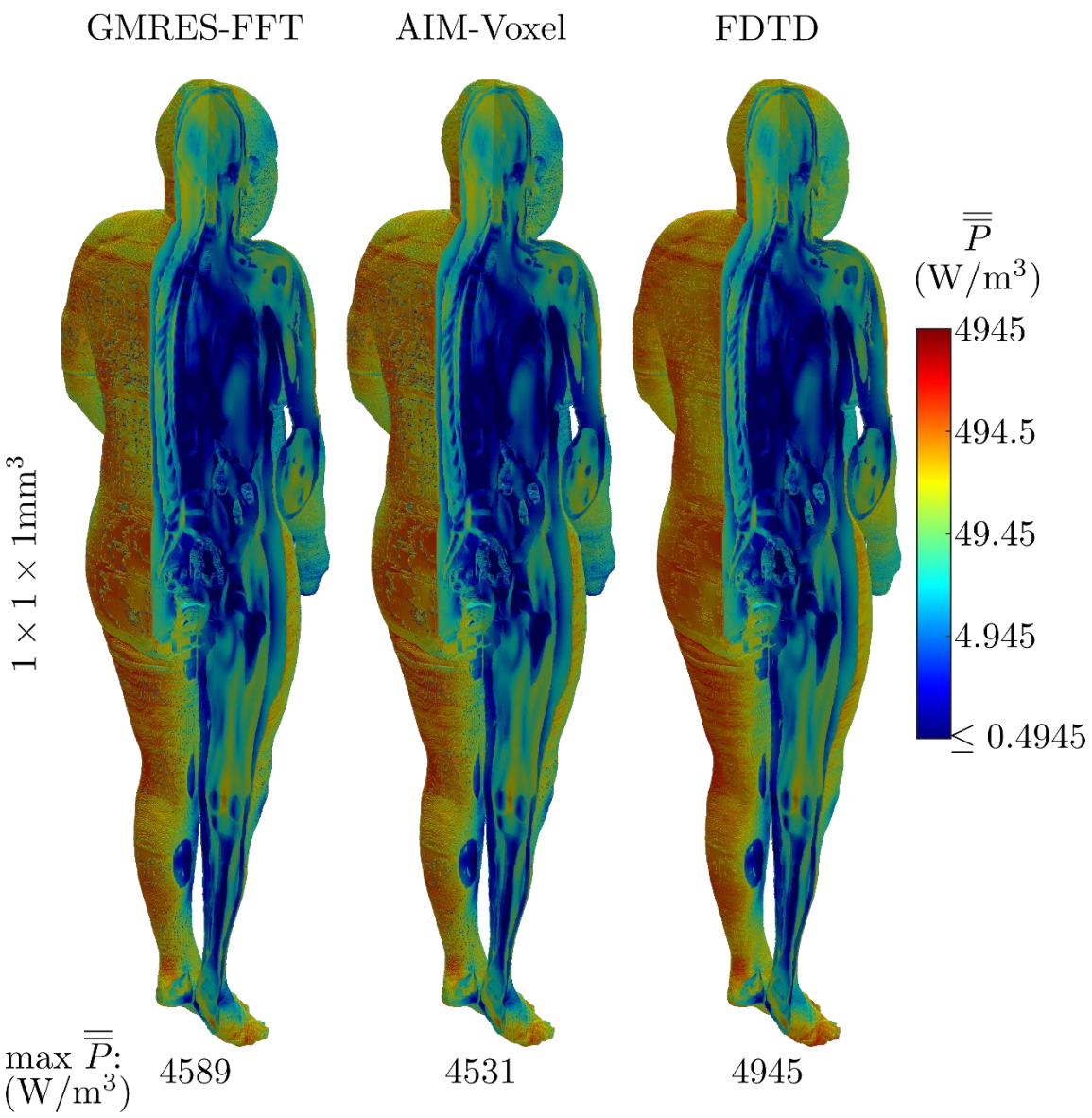

Figure 25: Cell-averaged time-averaged absorbed power density for the finest mesh of the AustinMan v2.2 model excited by a plane wave from behind. The results from three different methods are shown: GMRES-FFT, AIM-Voxel, and FDTD, all of which use a pixel-based model and voxel cells. One quadrant of the model is removed in the images to show the internal power density.

Table 4 Tissue absorbed power for the 1×1×1 mm^3 AustinWoman v2.1

Tissue	**Plot ID**	**FDTD** $\overline{P}_{\text{tissue}}$ (W)	**GMRES-FFT** $\overline{P}_{\text{tissue}}$ (W)	**AIM** $\overline{P}_{\text{tissue}}$ (W)	**Volume** (m^3)
Total	1	2.483E+00	2.483E+00	2.492E+00	8.195E+07
Muscle	2	9.803E-01	9.903E-01	9.975E-01	2.115E+07
Skin	3	8.545E-01	8.290E-01	8.210E-01	4.247E+06
Grey Matter	4	2.800E-02	2.854E-02	2.887E-02	8.208E+05
White Matter	5	7.749E-03	7.993E-03	8.196E-03	3.382E+05
Blood Vessel	6	1.419E-02	1.262E-02	1.283E-02	1.046E+06
Cerebro Spinal Fluid	7	1.349E-02	1.251E-02	1.269E-02	2.058E+05
Liver	8	1.227E-02	1.201E-02	1.248E-02	2.262E+06
Eye	9	2.976E-04	2.892E-04	2.851E-04	1.286E+04
Uterus	10	1.464E-04	1.514E-04	1.553E-04	6.292E+04

Chapter 5: Conclusion

This thesis compared two fundamentally different FFT-accelerated integral equation methods, GMRES-FFT and AIM, to FDTD when they are used to solve an important class of BioEM problems; specifically the power absorbed by a human model illuminated with an impressed time-harmonic source. A systematic approach that utilized benchmark problems, error measures, cost measures, and error-vs.-cost plots was developed to quantify the tradeoff between accuracy and computational costs of the methods and to judge to performance of the different methods.

It was found that AIM using surface-based models meshed with tetrahedral elements obtains significantly higher accuracy results compared to the numerical methods that used pixel-based models meshed with similar sized voxel elements. More importantly, the method was found to generally outperform the other numerical methods with respect to the accuracy-cost tradeoff, especially when comparing the memory requirement and solve/marching time costs of the methods. When only pixel-based models are available, however, FDTD became the best alternative for solving the benchmark problems (especially for anatomical models, far sources, and higher frequencies) because (i) AIM (using voxel meshes) and GMRES-FFT could not achieve higher accuracy results—in fact, the errors in all methods appeared to be dictated by the low fidelity of the pixel-based models—and (ii) FDTD required lower computational resources. An important caveat should be noted when comparing the methods' costs: Preconditioners can reduce the iterative-solution cost of AIM and GMRES-FFT and improve the methods competitiveness with FDTD [79], [80]. Finally, it is noteworthy to observe that AIM performed essentially on par with GMRES-FFT in this case.

Results also demonstrated that each of the three numerical methods are able to simulate complex whole-body pixel-based models, such as the AustinMan and AustinWoman models. The time-averaged absorbed power in the tissues computed by the different methods agreed within ~10% (if $1\times1\times1$ mm^3 resolution models were used). Solving the same problem using the fundamentally different methods can identify the level of uncertainty and increase/decrease the confidence in the result from each method.

Lastly, when performing BioEM analysis using more realistic device models than impressed Hertzian dipole sources, the error levels for FDTD and GMRES-FFT simulations are expected to increase due to the inaccurate modeling that arises from regular meshes/grids while the AIM error levels should remain similar to the results shown here. Thus, when complex antenna models are included in the simulations, AIM is expected to outperform the other numerical methods.

Appendix A

The following table provides the electromagnetic material properties that were used for the multilayered spherical head phantom at the three frequencies of interest. The material properties were obtained from [62], [68]. Bone average is a linear average of bone cortical and bone marrow. Brain average is a linear average of brain grey matter and brain white matter.

Table 5 Electromagnetic material properties for the multilayered spherical head phantom

	402 MHz		900 MHz		2.45 GHz	
	ε_r	σ (S/m)	ε_r	σ (S/m)	ε_r	σ (S/m)
Skin Dry	46.741	0.68892	41.405	0.86674	38.007	1.464
Fat	5.5789	0.041151	5.462	0.051043	5.2801	0.10452
Bone Average	9.40725	0.0604105	8.97915	0.091759	8.33895	0.2446735
Brain Average	49.721	0.59178	45.8055	0.76653	42.539	1.51135

The material properties for the anatomical human models, AustinMan v2.2 and AustinWoman v2.1, were based on the data in [62], [70]. Additional details about the development of the model can be found on the website: http://bit.ly/AustinMan.

Appendix B

The following tables provide information about the parameters used for the simulations presented in this thesis. All of the simulations were run on Stampede at TACC [78].

METHOD OF MOMENTS (MOM)

The MOM parameters that are used by both AIM and GMRES-FFT are listed in Table 6-Table 9 below. The GMRES iterative solver from PETSc (v3.4) [82] was used with an iterative solver tolerance equal to 10^{-4}. The GMRES restart value was set to 100.

Notes: * Volume cubature order is given as a pair of numbers. The first number denotes the order of the rule for the source integral (the inner integral in (8)); the second number denotes the order of the rule for the testing integral (the outer integral in (8)).

† If any of the cells comprising the testing function is closer than the singularity extraction factor multiplied by the maximum edge length of the source cell, then the inner integral is calculated by using traditional single-term singularity extraction [83].

Table 6 MOM parameters for the tetrahedral mesh of the spherical head phantom

Cell Volume	N_{MOM}	Volume Cubature Order*	Singularity Extraction Factor†
60.7 mm^3	175 494	{5, 3}	0.75
8.32 mm^3	1 276 029	{5, 3}	0.75
0.91 mm^3	11 645 244	{5, 3}	0.75

Table 7 MOM parameters for the voxel mesh of the spherical head phantom

Cell Volume	N_{MOM}	Volume Cubature Order*	Singularity Extraction Factor†
4×4×4 mm^3	254 388	{3, 3}	1.01
2×2×2 mm^3	2 004 408	{3, 3}	1.01
1×1×1 mm^3	15 939 336	{3, 3}	1.01

Table 8 MOM parameters for AustinMan v2.2

Cell Volume	N_{MOM}	Volume Cubature Order*	Singularity Extraction Factor†
8×8×8 mm^3	613 869	{3, 3}	1.01
4×4×4 mm^3	4 879 647	{3, 3}	1.01
2×2×2 mm^3	38 709 164	{3, 3}	1.01
1×1×1 mm^3	308 0012 198	{3, 3}	1.01

Table 9 MOM parameters for AustinWoman v2.1

Cell Volume	N_{MOM}	Volume Cubature Order*	Singularity Extraction Factor†
8×8×8 mm^3	494 477	{3, 3}	1.01
4×4×4 mm^3	3 928 920	{3, 3}	1.01
2×2×2 mm^3	31 130 421	{3, 3}	1.01
1×1×1 mm^3	247 549 701	{3, 3}	1.01

GMRES-FFT

Additional GMRES-FFT parameters and the computational environment used in the simulations with the multilayered spherical head phantom, AustinMan v2.2, and AustinWoman v2.1 are specified in Table 10-Table 12.

Table 10 GMRES-FFT parameters for multilayered spherical head phantom

Cell Volume	$N_x \times N_y \times N_z$	$\mathbf{r}_0$ (mm)	MPI Processes	Compute Nodes
4×4×4 mm^3	54×54×54	(-108,-108,-108)	1	1
2×2×2 mm^3	108×108×108	(-108,-108,-108)	1	1
1×1×1 mm^3	216×216×216	(-108,-108,-108)	4	4

Table 11 GMRES-FFT parameters for AustinMan v2.2

Cell Volume	$N_x \times N_y \times N_z$	$\mathbf{r}_0$ (mm)	MPI Processes	Compute Nodes
8×8×8 mm^3	41×71×234	(32,48,5)	1	1
4×4×4 mm^3	81×142×469	(36,52,1)	1	1
2×2×2 mm^3	162×284×938	(36,50,1)	16	16
1×1×1 mm^3	325×569×1877	(35,50,0)	256	256

Table 12 GMRES-FFT parameters for AustinWoman v2.1

Cell Volume	$N_x \times N_y \times N_z$	$\mathbf{r}_0$ (mm)	MPI Processes	Compute Nodes
8×8×8 mm^3	$36\times67\times216$	(40,88,2)	1	1
4×4×4 mm^3	$73\times133\times432$	(36,92,2)	1	1
2×2×2 mm^3	$146\times267\times865$	(38,90,0)	16	16
1×1×1 mm^3	$292\times536\times1730$	(37,89,0)	256	256

AIM-TETRA

Additional AIM parameters and the computational environment used in the simulations with the tetrahedral mesh of the multilayered spherical head phantom are specified in Table 13. Here, Q denotes the number of auxiliary grid points used to anter/interpolate each basis/testing cubature point (defined in [84]).

Table 13 AIM-Tetra parameters for multilayered spherical head phantom

Cell Volume	Q	$\gamma_{x,y,z}$	$\Delta c_{x,y,z}$	$N_{cx} \times N_{cy} \times N_{cz}$	$\mathbf{r}_0$ (mm)	MPI Processes	Compute Nodes
60.7 mm^3	8	1	4 mm	$64\times64\times64$	(-108, -108, -108)	1	1
8.32 mm^3	8	1	2 mm	$112\times112\times112$	(-108, -108, -108)	1	1
0.91 mm^3	8	2	1 mm	$224\times224\times224$	(-108, -108, -108)	16	16

AIM-VOXEL

Additional AIM parameters and the computational environment used in the simulations involving the voxel mesh of the multilayered spherical head phantom, AustinMan v2.2, and AustinWoman v2.1 are specified in Table 14-Table 16. Here, Q denotes the number of auxiliary grid points used to anter/interpolate each basis/testing cubature point (defined in [84]).

Table 14 AIM-Voxel parameters for multilayered spherical head phantom

Cell Volume	Q	$\gamma_{x,y,z}$	$\Delta c_{x,y,z}$	$N_{cx} \times N_{cy} \times N_{cz}$	$\mathbf{r}_0$ (mm)	MPI Processes	Compute Nodes
4×4×4 mm^3	8	0	4 mm	$64 \times 64 \times 64$	(-108, -108, -108)	1	1
2×2×2 mm^3	8	0	2 mm	$112 \times 112 \times 112$	(-108, -108, -108)	1	1
1×1×1 mm^3	8	1	1 mm	$224 \times 224 \times 224$	(-108, -108, -108)	16	16

Table 15 AIM-Voxel parameters for AustinMan v2.2

Cell Volume	Q	$\gamma_{x,y,z}$	$\Delta c_{x,y,z}$	$N_{cx} \times N_{cy} \times N_{cz}$	$\mathbf{r}_0$ (mm)	MPI Processes	Compute Nodes
8×8×8 mm^3	8	0	8 mm	$48 \times 80 \times 240$	(24,40,0)	1	1
4×4×4 mm^3	8	0	4 mm	$96 \times 144 \times 480$	(32,48,0)	4	2
2×2×2 mm^3	8	0	2 mm	$192 \times 288 \times 960$	(34,48,0)	32	16
1×1×1 mm^3	8	1	1 mm	$384 \times 576 \times 1920$	(34,49,0)	512	256

Table 16 AIM-Voxel parameters for AustinWoman v2.1

Cell Volume	Q	$\gamma_{x,y,z}$	$\Delta c_{x,y,z}$	$N_{cx} \times N_{cy} \times N_{cz}$	$\mathbf{r}_0$ (mm)	MPI Processes	Compute Nodes
8×8×8 mm^3	8	0	8 mm	$48 \times 80 \times 224$	(32,80,0)	1	1
4×4×4 mm^3	8	0	4 mm	$80 \times 144 \times 448$	(32,88,0)	4	2
2×2×2 mm^3	8	0	2 mm	$160 \times 288 \times 896$	(36,88,0)	32	16
1×1×1 mm^3	8	1	1 mm	$320 \times 576 \times 1792$	(36,88,0)	512	256

FDTD

For the FDTD simulations, the optimized parameters from [38] are used. A 5-cell thick split-field PML is used to truncate the computational domain for every simulation (regardless of mesh resolution). The PML conductivity profile is tapered using a third-order polynomial grading with a reflection error of $\Gamma(0) \approx e^{-8}$. The minimum distance between the scattering volume and the PML boundary is 64 mm in every simulation. The

ramped-up sinusoid defined in (56) (and based on the multiple cycle *m-n-m* pulse from [72]) is used for the excitation with $\zeta = 2$ ramp-up periods. The simulations are performed for 6 periods after the ramp up to achieve steady state; the resulting number of time steps N_T for each simulation are shown in Appendix C. Once in steady-state, the fields are converted to the frequency domain using an on-the-fly Fourier transform. Additional FDTD parameters and the computational environment is described in Table 17 for the multilayered spherical head phantom simulations, in Table 18 for the AustinMan v2.2 simulations, and Table 19 for the AustinWoman v2.1 simulations.

Table 17 FDTD parameters for multilayered spherical head phantom

Cell Volume	N_{FDTD}	$\mathbf{r}_0$ (mm)	MPI Processes	Compute Nodes
4×4×4 mm^3	96×96×96	(-192,-192,-192)	1	1
2×2×2 mm^3	182×182×182	(-182,-182,-182)	1	1
1×1×1 mm^3	354×354×354	(-177,-177,-177)	1	1

Table 18 FDTD parameters for AustinMan v2.2

Cell Volume	N_{FDTD}	$\mathbf{r}_0$ (mm)	MPI Processes	Compute Nodes
8×8×8 mm^3	67×97×260	(-72,-56,-99)	1	1
4×4×4 mm^3	123×184×511	(-48,-32,-83)	1	1
2×2×2 mm^3	236×358×1012	(-38,-24,-73)	1	1
1×1×1 mm^3	463×707×2015	(-34,-19,-69)	16	8

Table 19 FDTD parameters for AustinWoman v2.1

Cell Volume	N_{FDTD}	$\mathbf{r}_0$ (mm)	MPI Processes	Compute Nodes
8×8×8 mm^3	62×93×242	(-64,-16,-102)	1	1
4×4×4 mm^3	115×175×474	(-48,8,-82)	1	1
2×2×2 mm^3	220×341×939	(-36,16,-74)	1	1
1×1×1 mm^3	430×674×1868	(-32,20,-69)	16	8

Table 20 FDTD timestep parameters for simulations at 402 MHz, 900 MHz and 2.45 GHz

Cell Volume	Δt (s)
8×8×8 mm^3	$0.99\Delta x / c_0 \approx 1.525259895624805\times10^{-11}$
4×4×4 mm^3	$0.99\Delta x / c_0 \approx 7.626299478124023\times10^{-12}$
2×2×2 mm^3	$0.99\Delta x / c_0 \approx 3.813149739062012\times10^{-12}$
1×1×1 mm^3	$0.99\Delta x / c_0 \approx 1.906574869531006\times10^{-12}$

Table 21 FDTD excitation time delay values

Model	Excitation	t_d (s)
All head sphere resolutions	Plane wave	$-0.108 / c_0 \approx -3.602492228140042\times10^{-10}$
All head sphere resolutions	Hertzian dipole	$0.050 / c_0 \approx 1.667820475990760\times10^{-10}$
AustinMan 8×8×8 mm^3	Plane wave	$0.032 / c_0 \approx 1.067405104634087\times10^{-10}$
AustinMan 4×4×4 mm^3	Plane wave	$0.036 / c_0 \approx 1.200830742713347\times10^{-10}$
AustinMan 2×2×2 mm^3	Plane wave	$0.036 / c_0 \approx 1.200830742713347\times10^{-10}$
AustinMan 1×1×1 mm^3	Plane wave	$0.035 / c_0 \approx 1.167474333193532\times10^{-10}$
AustinWoman 8×8×8 mm^3	Plane wave	$0.040 / c_0 \approx 1.334256380792608\times10^{-10}$
AustinWoman 4×4×4 mm^3	Plane wave	$0.036 / c_0 \approx 1.200830742713347\times10^{-10}$
AustinWoman 2×2×2 mm^3	Plane wave	$0.038 / c_0 \approx 1.267543561752978\times10^{-10}$
AustinWoman 1×1×1 mm^3	Plane wave	$0.037 / c_0 \approx 1.234187152233163\times10^{-10}$

Appendix C

Additional data is included in this Appendix for completeness.

Table 22 The number of iterations required for the iterative solver to converge for AIM and GMRES-FFT and the number of timesteps for FDTD

Simulation	Avg. Cell Volume (mm^3)†	AIM-Tetra N_{iter}	GMRES-FFT N_{iter}	AIM-Voxel N_{iter}	FDTD N_T
Head PW 402 MHz	60.7/64	149	95	99	2616
	8.32/8	173	94	98	5224
	0.91/1	165	90	98	10440
Head PW 900 MHz	60.7/64	423	363	374	1168
	8.32/8	505	353	361	2336
	0.91/1	488	334	339	4664
Head PW 2.45 GHz	60.7/64	1191	1205	1168	432
	8.32/8	1343	1156	1140	864
	0.91/1	1362	1084	1063	1720
Head HD 900 MHz	60.7/64	434	367	380	1168
	8.32/8	532	355	371	2336
	0.91/1	509	341	347	4664
AustinMan PW 900 MHz	512	-	1260	1210	584
	64	-	1217	1187	1168
	8	-	1187	1168	2336
	1	-	1163	1148	4664
AustinWoman PW 900 MHz	512	-	1036	992	584
	64	-	1016	980	1168
	8	-	997	972	2336
	1	-	984	955	4664

Legend: PW = Plane Wave; HD = Hertzian Dipole; Head = multilayered spherical head phantom; AustinMan = AustinMan v2.2; AustinWoman = AustinWoman v2.1

† the average cell volume is given as average tetrahedron/voxel volume where applicable

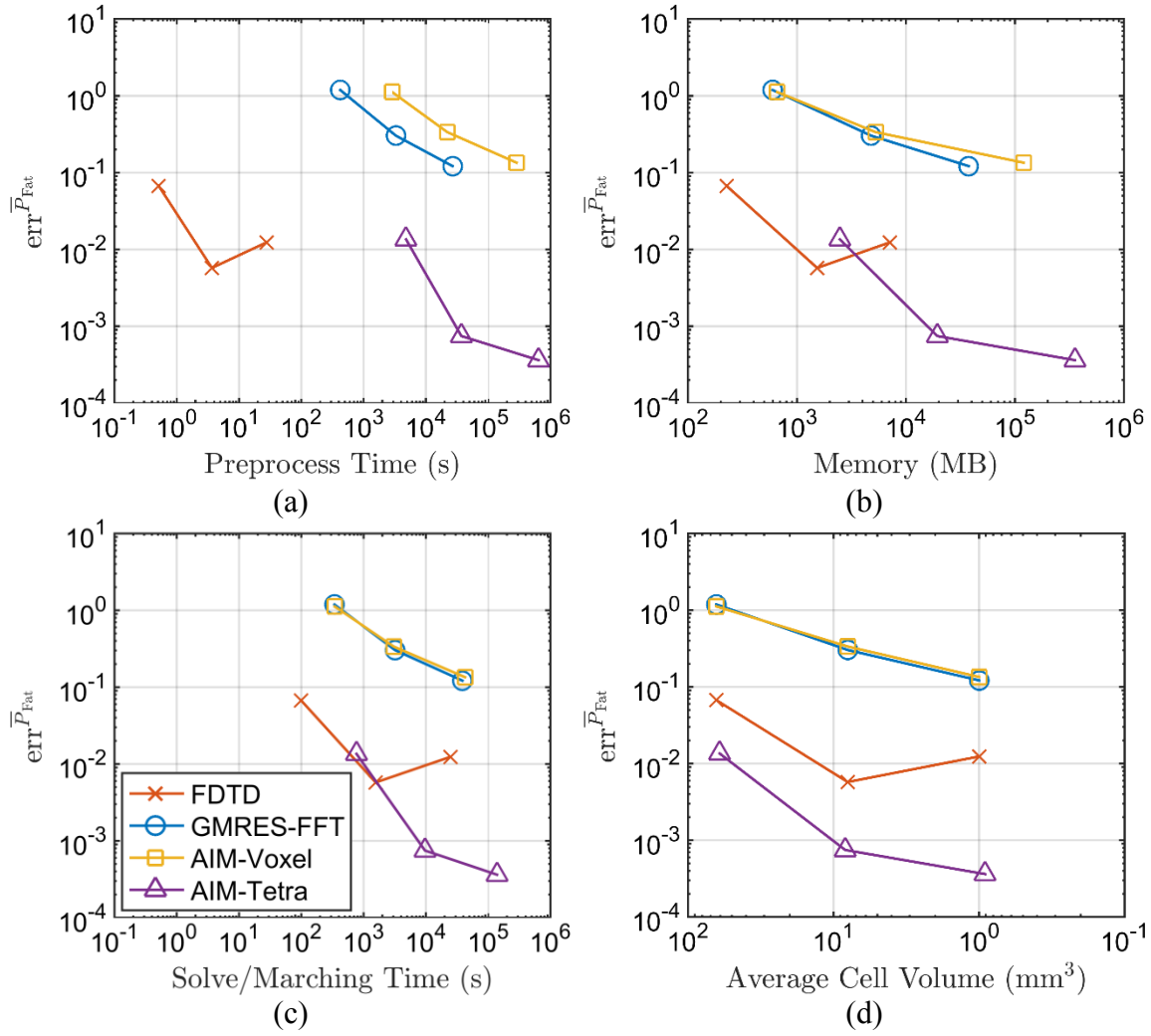

Figure 26: Accuracy-efficiency tradeoffs for the baseline case using the relative error of the power absorbed in the fat layer. The relative error of $\overline{P}_{\mathrm{Fat}}$ is plotted vs. the (a) preprocess time, (b) memory, (c) solve/ marching time, and (d) average cell volume as the model resolution is increased.

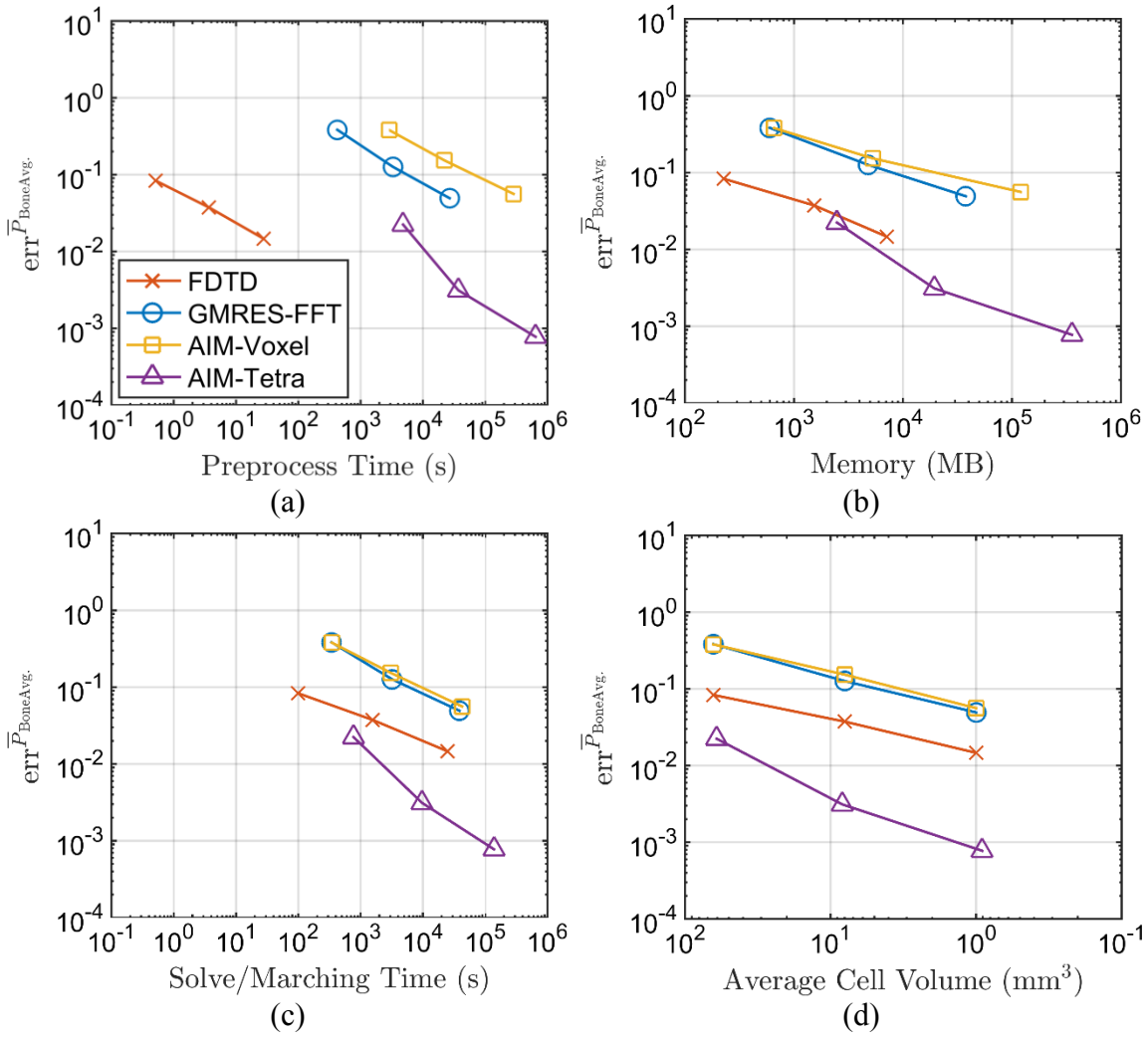

Figure 27: Accuracy-efficiency tradeoffs for the baseline case using the relative error of the power absorbed in the bone layer. The relative error of $\overline{P}_{\text{Bone Avg.}}$ is plotted vs. the (a) preprocess time, (b) memory, (c) solve/ marching time, and (d) average cell volume as the model resolution is increased.

References

[1] L. Roelens, S. Van den Bulcke, W. Joseph, G. Vermeeren, and L. Martens, "Path loss model for wireless narrowband communication above flat phantom," *Electron. Lett.*, vol. 42, no. 1, pp. 10–11, 2006.

[2] T. Bjorninen, E. Moradi, L. Sydanheimo, J. M. Carmena, J. M. Rabaey, and L. Ukkonen, "Electromagnetic modelling and measurement of antennas for wireless brain-machine interface systems," in *2013 IEEE MTT-S International Microwave Workshop Series on RF and Wireless Technologies for Biomedical and Healthcare Applications (IMWS-BIO)*, 2013, pp. 1–3.

[3] S. Amendola, E. Moradi, K. Koski, T. Bjorninen, L. Sydanheimo, L. Ukkonen, J. M. Rabaey, and Y. Rahmat-Samii, "Design and optimization of mm-size implantable and wearable on-body antennas for biomedical systems," in *The 8th European Conference on Antennas and Propagation (EuCAP 2014)*, 2014, pp. 520–524.

[4] S. Almari, R. J. Langley, and A. O. AlAmoudi, "Improved performance of 2.45 GHz implanted patch antenna for wireless communication," in *2013 Loughborough Antennas & Propagation Conference (LAPC)*, 2013, pp. 27–30.

[5] D. Wu, S. Shamsi, J. Chen, and W. Kainz, "Evaluations of specific absorption rate and temperature increase within pregnant female models in magnetic resonance imaging birdcage coils," *IEEE Trans. Microw. Theory Tech.*, vol. 54, no. 12, pp. 4472–4478, Dec. 2006.

[6] S. Wolf, D. Diehl, M. Gebhardt, J. Mallow, and O. Speck, "SAR simulations for high-field MRI: How much detail, effort, and accuracy is needed?," *Magn. Reson. Med.*, vol. 69, no. 4, pp. 1157–68, Apr. 2013.

[7] J. Chen, Z. Feng, and J. M. Jin, "Numerical simulation of SAR and B1-field inhomogeneity of shielded RF coils loaded with the human head," *IEEE Trans. Biomed. Eng.*, vol. 45, no. 5, pp. 650–9, May 1998.

[8] "IEEE Standard for Local and metropolitan area networks - Part 15.6: Wireless Body Area Networks," *IEEE Std 802.15.6-2012*, 2012.

[9] "IEEE Recommended Practice for Determining the Peak Spatial-Average Specific Absorption Rate (SAR) in the Human Head from Wireless Communications Devices: Measurement Techniques," *IEEE Std 1528-2013 (Revision IEEE Std 1528-2003)*, 2013.

[10] "IEEE Standard for Safety Levels with Respect to Human Exposure to Radio Frequency Electromagnetic Fields, 3 kHz to 300 GHz," *IEEE Std C95.1-2005 (Revision IEEE Std C95.1-1991)*, 2005.

[11] W. Kainz, A. Christ, T. Kellom, S. Seidman, N. Nikoloski, B. Beard, and N. Kuster, "Dosimetric comparison of the specific anthropomorphic mannequin (SAM) to 14 anatomical head models using a novel definition for the mobile phone positioning," *Phys. Med. Biol.*, vol. 50, no. 14, pp. 3423–45, Jul. 2005.

[12] V. Monebhurrun, Y. Braux, H. Devos, M. Kozlov, W. Simon, and T. Wittig, "A benchmark CAD mobile phone model for specific absorption rate calculations," *IEEE Trans. Magn.*, vol. 50, no. 2, pp. 1057–1060, Feb. 2014.

[13] T. Nagaoka, S. Watanabe, K. Sakurai, E. Kunieda, S. Watanabe, M. Taki, and Y. Yamanaka, "Development of realistic high-resolution whole-body voxel models of Japanese adult males and females of average height and weight, and application of models to radio-frequency electromagnetic-field dosimetry," *Phys. Med. Biol.*, vol. 49, no. 1, pp. 1–15, Jan. 2004.

[14] A. Christ, W. Kainz, E. G. Hahn, K. Honegger, M. Zefferer, E. Neufeld, W. Rascher, R. Janka, W. Bautz, J. Chen, B. Kiefer, P. Schmitt, H.-P. Hollenbach, J. Shen, M. Oberle, D. Szczerba, A. Kam, J. W. Guag, and N. Kuster, "The Virtual Family--development of surface-based anatomical models of two adults and two children for dosimetric simulations," *Phys. Med. Biol.*, vol. 55, no. 2, pp. N23–38, Jan. 2010.

[15] T. Wu, L. Tan, Q. Shao, C. Zhang, C. Zhao, Y. Li, E. Conil, A. Hadjem, J. Wiart, B. Lu, L. Xiao, N. Wang, Y. Xie, and S. Zhang, "Chinese adult anatomical models and the application in evaluation of RF exposures," *Phys. Med. Biol.*, vol. 56, no. 7, pp. 2075–89, Apr. 2011.

[16] J. W. Massey, C. S. Geyik, N. Techachainiran, C. Hsu, R. Q. Nguyen, T. Latson, M. Ball, E. Celik, and A. E. Yilmaz, "AustinMan and AustinWoman: High fidelity, reproducible, and open-source electromagnetic voxel models," in *The 34th Annual Meeting of the Bioelectromagnetics Society*, 2012.

[17] A. Taflove and S. C. Hagness, *Computational Electrodynamics: The Finite-Difference Time-Domain Method*, 3rd ed. Artech House, 2005.

[18] D. Xue, L. Demkowicz, and L. Hao, "A 3-D hp finite/infinite element method to calculate power deposition in the human head," *IEEE Trans. Biomed. Eng.*, vol. 54, no. 4, pp. 734–41, Apr. 2007.

[19] J. Chen, J. Jin, H. Gan, and W. Chew, "Analysis of electromagnetic wave interaction with biological tissue using CG-FFT method," in *IEEE Antennas and Propagation Society International Symposium. 1996 Digest*, 1996, vol. 3, pp. 1814–1817.

[20] J. M. Jin, J. Chen, W. C. Chew, H. Gan, R. L. Magin, and P. J. Dimbylow, "Computation of electromagnetic fields for high-frequency magnetic resonance imaging applications," *Phys. Med. Biol.*, vol. 41, no. 12, pp. 2719–2738, Dec. 1996.

[21] J. M. Song and W. C. Chew, "Multilevel fast-multipole algorithm for solving combined field integral equations of electromagnetic scattering," *Microw. Opt. Technol. Lett.*, vol. 10, no. 1, pp. 14–19, 1995.

[22] Ö. Ergül and L. Gürel, "Efficient parallelization of the multilevel fast multipole algorithm for the solution of large-scale scattering problems," *IEEE Trans. Antennas Propag.*, vol. 56, no. 8, pp. 2335–2345, 2008.

[23] F. Wei and A. E. Yilmaz, "A more scalable and efficient parallelization of the adaptive integral method—Part II: BIOEM application," *IEEE Trans. Antennas Propag.*, vol. 62, no. 2, pp. 727–738, Feb. 2014.

[24] D. T. Borup, D. M. Sullivan, and O. P. Gandhi, "Comparison of the FFT conjugate gradient method and the finite-difference time-domain method for the 2-D absorption problem," *IEEE Trans. Microw. Theory Tech.*, vol. 35, no. 4, pp. 383–395, Apr. 1987.

[25] M. F. Iskander, "Computational techniques in bioelectromagnetics," *Comput. Phys. Commun.*, vol. 68, no. 1–3, pp. 224–254, Nov. 1991.

[26] P. Wust, J. Nadobny, M. Seebass, J. M. Dohlus, W. John, and R. Felix, "3-D computation of E fields by the volume-surface integral equation (VSIE) method in comparison with the finite-integration theory (FIT) method," *IEEE Trans. Biomed. Eng.*, vol. 40, no. 8, pp. 745–59, Aug. 1993.

[27] E. A. Forgy, J. Chen, W. C. Chew, and J. M. Jin, "A comparison of the BCG-FFT and FD-TD methods for the 3-D human head absorption problem," in *IEEE Antennas and Propagation Society International Symposium 1997. Digest*, 1997, vol. 2, pp. 1202–1205.

[28] P. Wust, J. Nadobny, M. Seebass, D. Stalling, J. Gellermann, H. C. Hege, P. Deuflhard, and R. Felix, "Influence of patient models and numerical methods on

predicted power deposition patterns," *Int. J. Hyperthermia*, vol. 15, no. 6, pp. 519–40, 1999.

[29] "Virtual Population." [Online]. Available: http://www.itis.ethz.ch/itis-for-health/virtual-population/human-models/.

[30] M.-C. Gosselin, E. Neufeld, H. Moser, E. Huber, S. Farcito, L. Gerber, M. Jedensjö, I. Hilber, F. Di Gennaro, B. Lloyd, E. Cherubini, D. Szczerba, W. Kainz, and N. Kuster, "Development of a new generation of high-resolution anatomical models for medical device evaluation: the Virtual Population 3.0.," *Phys. Med. Biol.*, vol. 59, no. 18, pp. 5287–5303, 2014.

[31] J.-P. Berenger, "A perfectly matched layer for the absorption of electromagnetic waves," *J. Comput. Phys.*, vol. 114, no. 2, pp. 185–200, Oct. 1994.

[32] D. Schaubert, D. Wilton, and A. Glisson, "A tetrahedral modeling method for electromagnetic scattering by arbitrarily shaped inhomogeneous dielectric bodies," *IEEE Trans. Antennas Propag.*, vol. 32, no. 1, pp. 77–85, Jan. 1984.

[33] M. F. Cátedra, E. Gago, and L. Nuno, "A numerical scheme to obtain the RCS of three-dimensional bodies of resonant size using the conjugate gradient method and the fast Fourier transform," *IEEE Trans. Antennas Propag.*, vol. 37, no. 5, pp. 528–537, May 1989.

[34] E. Bleszynski, M. Bleszynski, and T. Jaroszewicz, "AIM: Adaptive integral method for solving large-scale electromagnetic scattering and radiation problems," *Radio Sci.*, vol. 31, no. 5, pp. 1225–1251, 1996.

[35] F. Wei and A. E. Yilmaz, "A hybrid message passing/shared memory parallelization of the adaptive integral method for multi-core clusters," *Parallel Comput.*, vol. 37, no. 6–7, pp. 279–301, Jun. 2011.

[36] Top500.org, "Performance Development," 2014. [Online]. Available: http://top500.org/statistics/perfdevel/.

[37] C. S. Geyik, F. Wei, J. Massey, and A. E. Yilmaz, "FDTD vs. AIM for bioelectromagnetic analysis," in *Proceedings of the 2012 IEEE International Symposium on Antennas and Propagation*, 2012, pp. 1–2.

[38] C. S. Geyik, "Accuracy-efficiency comparison of finite-difference time-domain and adaptive integral method based simulators for bioelectromagnetics," The University of Texas at Austin, 2013.

[39] J. Massey, F. Wei, C. Geyik, and A. Yilmaz, “A comparison of accuracy-efficiency tradeoffs of FDTD and FFT-accelerated integral equation methods for numerical dosimetry,” in *Proc. BIOEM 2013*, 2013, no. i.

[40] F. Wei, J. W. Massey, C. S. Geyik, and A. E. Yilmaz, “Error measures for comparing bioelectromagnetic simulators,” in *Proceedings of the 2012 IEEE International Symposium on Antennas and Propagation*, 2012, no. 3, pp. 1–2.

[41] H. Gan and W. C. Chew, “A discrete BCG-FFT algorithm for solving 3D inhomogeneous scatterer problems,” *J. Electromagn. waves Appl.*, vol. 9, no. 10, pp. 1339–1357, 1995.

[42] F. Wei and A. E. Yilmaz, “A 2-D decomposition based parallelization of AIM for 3-D BIOEM problems,” in *2011 IEEE International Symposium on Antennas and Propagation (APSURSI)*, 2011, no. 3, pp. 3158–3161.

[43] P. Zwamborn and P. M. van den Berg, “The three dimensional weak form of the conjugate gradient FFT method for solving scattering problems,” *IEEE Trans. Microw. Theory Tech.*, vol. 40, no. 9, pp. 1757–1766, 1992.

[44] M. L. Hastriter and W. C. Chew, “Role of numerical noise in ultra large-scale computing,” in *IEEE Antennas Propag. Soc. Symp., 2004.*, 2004, pp. 3373–3376 Vol. 3.

[45] R. Holland, “Pitfalls of staircase meshing,” *IEEE Trans. Electromagn. Compat.*, vol. 35, no. 4, pp. 434–439, 1993.

[46] T. Xiao and Q. H. Liu, “A staggered upwind embedded boundary (SUEB) method to eliminate the FDTD staircasing error,” *IEEE Trans. Antennas Propag.*, vol. 52, no. 3, pp. 730–741, Mar. 2004.

[47] Q. Du and D. Wang, “Tetrahedral mesh generation and optimization based on centroidal Voronoi tessellations,” *Int. J. Numer. Methods Eng.*, vol. 56, no. 9, pp. 1355–1373, Mar. 2003.

[48] J. R. Shewchuk, “Tetrahedral mesh generation by Delaunay refinement,” in *Proceedings of the fourteenth annual symposium on Computational geometry - SCG ’98*, 1998, pp. 86–95.

[49] Y. Zhang, C. Bajaj, and B.-S. Sohn, “3D finite element meshing from imaging data,” *Comput. Methods Appl. Mech. Eng.*, vol. 194, no. 48–49, pp. 5083–5106, Nov. 2005.

[50] S. J. Owen and D. R. White, “Mesh-based geometry,” *Int. J. Numer. Methods Eng.*, vol. 58, no. 2, pp. 375–395, 2003.

[51] L. Demkowicz, P. Gatto, W. Qiu, and a. Joplin, “G1-Interpolation and geometry reconstruction for higher order finite elements,” *Comput. Methods Appl. Mech. Eng.*, vol. 198, no. 13–14, pp. 1198–1212, Mar. 2009.

[52] J. W. Massey, F. Wei, and A. E. Yilmaz, “A hybrid surface-volume integral-equation method for analyzing scattering from voxel-based anatomical human models with smooth skin,” in *2014 USNC-URSI Radio Science Meeting (Joint with AP-S Symposium)*, 2014, vol. I, pp. 193–193.

[53] D. Szczerba, E. Neufeld, M. Zefferer, G. Szekely, and N. Kuster, “Unstructured mesh generation from the Virtual Family models for whole body biomedical simulations,” *Procedia Comput. Sci.*, vol. 1, no. 1, pp. 837–844, May 2010.

[54] C. F. Wang and J. M. Jin, “Simple and efficient computation of electromagnetic fields in arbitrarily shaped inhomogeneous dielectric bodies using transpose-free QMR and FFT,” *IEEE Trans. Microw. Theory Tech.*, vol. 46, no. 5, pp. 553–558, May 1998.

[55] M. M. Botha, “Solving the volume integral equations of electromagnetic scattering,” *J. Comput. Phys.*, vol. 218, no. 1, pp. 141–158, 2006.

[56] K. Yang and A. E. Yilmaz, “Integral equation solution of 3-D anisotropic lossy dielectrics in uniaxial layered media,” in *Antennas and Propagation Society International Symposium (APSURSI), 2012 IEEE*, 2012, no. i, pp. 5–6.

[57] F. Wei and A. E. Yilmaz, “A more scalable and efficient parallelization of the adaptive integral method—Part I: Algorithm,” *IEEE Trans. Antennas Propag.*, vol. 62, no. 2, pp. 714–726, Feb. 2014.

[58] A. E. Yilmaz, J.-M. Jin, and E. Michielssen, “Time domain adaptive integral method for surface integral equations,” *IEEE Trans. Antennas Propag.*, vol. 52, no. 10, pp. 2692–2708, Oct. 2004.

[59] K. Yang, F. Wei, and A. E. Yilmaz, “Truncated multigrid versus pre-corrected FFT/AIM for bioelectromagnetics: When is O(N) better than O(NlogN)?,” *2011 Comput. Electromagn. Int. Work. CEM’11*, vol. 0, pp. 153–158, 2011.

[60] K. S. Yee, “Numerical solution of initial boundary value problems involving Maxwell’s equations in isotropic media,” *IEEE Trans. Antennas Propag.*, vol. 14, no. 3, pp. 302–307, May 1966.

[61] R. Courant, K. Friedrichs, and H. Lewy, “On the partial difference equations of mathematical physics,” *IBM J. Res. Dev.*, vol. 11, no. 2, pp. 215–234, Mar. 1967.

[62] S. Gabriel, R. W. Lau, and C. Gabriel, “The dielectric properties of biological tissues: III. Parametric models for the dielectric spectrum of tissues,” *Phys. Med. Biol.*, vol. 41, no. 11, pp. 2271–93, Nov. 1996.

[63] C. A. Balanis, *Advanced Engineering Electromagnetics*. New York, New York, USA: Wiley, 1989.

[64] J. L. Young, “Propagation in linear dispersive media: Finite difference time-domain methodologies,” *IEEE Trans. Antennas Propag.*, vol. 43, no. 4, pp. 422–426, Apr. 1995.

[65] S. S. Zivanovic, K. S. Yee, and K. K. Mei, “A subgridding method for the time-domain finite-difference method to solve Maxwell’s equations,” *IEEE Trans. Microw. Theory Tech.*, vol. 39, no. 3, pp. 471–479, Mar. 1991.

[66] S. Benkler, N. Chavannes, and N. Kuster, “A new 3-D conformal PEC FDTD scheme with user-defined geometric precision and derived stability criterion,” *IEEE Trans. Antennas Propag.*, vol. 54, no. 6, pp. 1843–1849, Jun. 2006.

[67] V. M. Spitzer, M. J. Ackerman, A. L. Scherzinger, and D. G. Whitlock, “The visible human male: A technical report,” *J. Am. Med. Inform. Assoc.*, vol. 3, no. 2, pp. 118–30, 1996.

[68] D. Andreuccetti, R. Fossi, and C. Petrucci, “An Internet resource for the calculation of the dielectric properties of body tissues in the frequency range 10 Hz - 100 GHz,” *IFAC-CNR, Florence (Italy)*, 1997. [Online]. Available: http://niremf.ifac.cnr.it/tissprop/.

[69] csimsoft, “Trelis FEA.” 2014.

[70] J. W. Massey, C. S. Geyik, N. Techachainiran, C. Hsu, R. Q. Nguyen, T. Latson, M. Ball, and A. E. Yilmaz, “AustinMan Electromagnetic Voxels,” 2013. [Online]. Available: http://bit.ly/AustinMan.

[71] J. W. Massey, F. Wei, G. Kaur, K. Yang, C. S. Geyik, and A. E. Yilmaz, “Bioelectromagnetic Benchmarks.” [Online]. Available: http://web.corral.tacc.utexas.edu/BioEM-Benchmarks/index.html. [Accessed: 08-May-2015].

[72] R. Ziolkowski and E. Heyman, “Wave propagation in media having negative permittivity and permeability,” *Phys. Rev. E*, vol. 64, no. 5, p. 056625, Oct. 2001.

[73] G. Kaur, “COMPASS-EM: Comprehensive program for analytical scattering solutions for electromagnetics.” [Online]. Available: http://web.corral.tacc.utexas.edu/BioEM-Benchmarks/COMPASS-EM/index.html.

[74] International Commission on Non-Ionizing Radiation Protection (ICNIRP), “Guidelines for limiting exposure to time-varying electric, magnetic, and electromagnetic fields (up to 300 GHz),” *Health Phys.*, vol. 74, no. 4, 1998.

[75] G. Kaur and A. E. Yılmaz, “Empirical comparison of envelope-tracking and time-domain adaptive integral methods for surface integral equations,” 2014.

[76] G. Kaur and A. E. Yılmaz, “Envelope-tracking adaptive integral method for band-pass transient scattering analysis,” *IEEE Trans. Antennas Propag.*, 2015.

[77] M. E. G. Ong, “Uniform refinement of a tetrahedron,” *SIAM J. Sci. Comput.*, vol. 15, no. 5, pp. 1134–1144, 1994.

[78] TACC, “Stampede User Guide.” [Online]. Available: https://portal.tacc.utexas.edu/user-guides/stampede. [Accessed: 08-May-2015].

[79] T. Malas and A. E. Yilmaz, “Near-field preconditioners for large-scale AIM-accelerated bioelectromagnetics simulations,” in *Proc. USNC/URSI Radio Science Meeting*, 2011.

[80] F. Wei and A. E. Yilmaz, “Parallel truncated multigrid preconditioning of AIM for bioelectromagnetics,” in *Proc. USNC/URSI Radio Science Meeting*, 2012.

[81] F. Wei and A. E. Yilmaz, “Surface-preconditioned AIM-accelerated surface-volume integral equation solution for bioelectromagnetics,” in *Proceedings of the 2012 International Conference on Electromagnetics in Advanced Applications, ICEAA’12*, 2012, vol. I, no. 1, pp. 869–872.

[82] “Portable, Extensible Toolkit for Scientific Computation (PETSc).” [Online]. Available: http://www.mcs.anl.gov/petsc/.

[83] G. Kaur and A. E. Yilmaz, “A practical implementation and comparative assessment of the radial-angular-transform singularity cancellation method,” *IEEE Trans. Antennas Propag.*, vol. 59, no. 12, pp. 4634–4642, Dec. 2011.

[84] K. Yang and A. E. Yilmaz, “Comparison of precorrected FFT/adaptive integral method matching schemes,” *Microw. Opt. Technol. Lett.*, vol. 53, no. 6, pp. 1368–1372, 2011.